Processing and properties of graphene reinforced glass/ceramic composites

Harshit Porwal

Submitted in partial fulfilment of the requirements of the Degree of Doctor of Philosophy

School of Engineering and Materials Science,
Queen Mary, University of London
London, United Kingdom
February 2015

Declaration

I hereby declare that the present work is prepared solely by me during the course of my doctoral studies at the Queen Mary, University of London. It has not been submitted anywhere for any award. Work of other people is fully acknowledged according to standard referencing.

This thesis fully complies with the regulations set by the University of London and the Queen Mary, University of London.

Harshit Porwal

Feb’2015

Abstract

This research provides a comprehensive investigation in understanding the effect of the addition of graphene nano-platelets (GNP) on the mechanical, tribological and biological properties of glass/ceramic composites. We investigated two kinds of materials namely amorphous matrices like glasses (silica, bioglass) and polycrystalline matrices like ceramics (alumina). The idea was to understand the effect of GNP on these matrices as GNP was expected to behave differently in these composites. Bioglass (BG) was also chosen as a matrix material to prepare BG-GNP composites. GNP can improve the electrical conductivity of BG which can be used further for bone tissue engineering applications. The effect of GNP on both electrical conductivity and bio-activity of BG-GNP composites was investigated in detail. There were three main problems for fabricating these novel nano-composites:

1) Production of good quality graphene;

2) Homogeneous dispersion of graphene in a glass/ceramic matrix and;

3) Retention of the graphitic structure during high temperature processing.

The first problem was solved by synthesising GNP using liquid phase exfoliation method instead of using a commercially available GNP. The prepared GNP were ~1 μm in length with a thickness of 3-4 layers confirmed using transmission electron microscopy. In order to solve the second problem various processing techniques were used including powder and colloidal processing routes along with different solvents. Processing parameters were optimised to fabricate glass/ceramic-GNP composite powders. Finally in order to avoid thermal degradation of the GNP during high temperature processing composites were

sintered using spark plasma sintering (SPS) technique. Fully dense composites were obtained without damaging GNP during the sintering process also confirmed via Raman spectroscopy. Finally the prepared composites were characterised for mechanical, tribological and biological applications.

Interestingly fracture toughness and wear resistance of the silica nano-composites increased with increasing concentration of GNP in the glass matrix. There was an improvement of ~45% in the fracture toughness and ~550% in the wear resistance of silica-GNP composites with the addition of 5 vol% GNP. GNP was found to be aligned in a direction perpendicular to the applied force in SPS. In contrast to amorphous materials fracture toughness and scratch resistance of alumina-GNP composites increased only for small loading of GNP and properties of the composites decreased after a critical concentration. There was an improvement of ~40% in the fracture toughness with the addition of only 0.5 vol% GNP in the alumina matrix while the scratch resistance of the composite increased by ~10% in the micro-ductile region. Electrical conductivity of the BG-GNP composite was increased by ~9 orders of magnitude compared to pure BG. In vitro bioactivity tests performed on BG-GNP composites confirmed that the addition of GNP to BG matrix also improved the bioactivity of the nano-composites confirmed using XRD analysis. Future work should focus on understanding electrical and thermal properties of these novel nano-composites.

Acknowledgement

I would like to express my sincere gratitude to my Supervisor, Prof. Michael John Reece. Under his continuous guidance and support it was possible to complete my PhD. He encouraged me throughout my PhD and provided many opportunities to work on collaborative projects and develop deep understanding of the subject. His knowledge of the ceramic science has been and will be an infinite source of inspiration throughout my career. I would also like to thank my secondary supervisor Dr. Haixue Yan, whose critical analysis helped me during my research.

I would specially like to thank Dr. Salvatore Grasso and Dr. Peter Tatarko for stimulating discussions, ideas and help with the experiments. This research would not have been possible without their help.

I would like to acknowledge the help provided by my colleagues and friends particularly Dr. Ben Milsom, Dr. Jibran Khaliq, Chunchun Li, Dr. Mahesh Kumar Mani, Richa Saggar and Dr. Umar Khan.

A special thanks to my family and friends for encouraging me throughout my PhD. I am grateful to my father Arvind and mother Radha Porwal for all the sacrifices they made so that I can have good education. Words cannot express how lucky I feel to be your son.

Finally I would like to thanks European Union's Seventh Framework Programme managed by REA-Research Executive Agency http://ec.europa.eu/research/rea (Marie Curie Action, GlaCERCo GA 264526) for their support and funding for this research.

Table of Content

List of Figures

.

Figure 9.7 High magnification SEM images of BG and BG-GNP composites showing the formation of HA after 3 day immersion time in SBF; **a)** Pure BG; **b)** BG-GNP (1 vol%); **c)** BG-GNP (3 vol%); and **d)** BG-GNP (5 vol%) composites.

List of Tables

Chapter 1 Introduction

Monolithic ceramics have attractive properties like high elastic stiffness, mechanical strength, stability at high temperatures, making them useful for biomedical, electronic, automotive, industrial, defence and space applications. However, monolithic ceramics tend to be brittle, mechanically unreliable and poor electrical conductors, which limit their use. In order to improve these properties, ceramic matrix composites have been developed. There has been a considerable amount of research reported in the literature on fibre-ceramic composites [1]. In the last decade it has focussed mainly on CNT reinforced glass and ceramic composites [2]. Authors have reported remarkable improvements in properties like hardness [3], toughness [4, 5], strength [6], thermal [7] and electrical [8, 9] conductivity over monolithic ceramics. In the case of alumina composites, Fan et al. [10] reported an improvement of ~100% in fracture toughness and ~20% in flexural strength with the addition of only 1 wt% SWNTs. Zhan et al.[11] reported an improvement of 13 orders of magnitude in electrical conductivity with 15 vol% SWNTs.

Graphene has similar electrical [12], mechanical [13] and thermal [14] properties compared to CNTs. The main advantages of using graphene over CNTs are a higher specific surface area [15] and less tendency to tangle, which makes it easier to disperse graphene into a matrix [16], whereas CNTs usually require surface modification [2] in order to process them. It is also relatively easy to produce, inexpensive and potentially is less of a health hazard compared to CNTs [17]. In view of these advantages and its excellent properties, incorporating graphene into ceramics to produce reinforced ceramic composites has great potential.

Graphene may find use in various applications including sensors [18], ultra capacitors [19], liquid crystal displays [20], organic light emitting diodes [21], solar cells [22], and polymer [23-26] and ceramic [27] composites. In polymers there has been a considerable amount of research on graphene composites [28], which have low electrical percolation thresholds (0.1 vol%) [23] and good mechanical properties and thermal conductivity [29]. Research on Graphene Ceramic Matrix Composites (GCMC), although quite promising, is still quite limited and unexploited.

Present work focuses on understanding the effects of GNP on mechanical, tribological and biological properties of glass/ceramic composites. The thesis is divided into three parts: 1) Silica composites (amorphous matrix); 2) Alumina composites (polycrystalline matrix); and 3) Bioglass composites (bio-materials). Each part focusses on processing, fabrication and characterisation of the nano-composites. The thesis is organised as follows; Chapter 2 is the literature review and provides details about production, processing and properties of graphene-glass/ceramic composites. Chapter 3 contains details about the synthesis of GNP, materials used and characterisation techniques. Chapter 4-6 provides details about the silica composites. Chapter 3 is focussed on the optimisation of the processing conditions for preparing silica-GNP composites while Chapter 5 and 6 provide details about mechanical and tribological properties of the composites. Chapter 7 provides details about fabrication and mechanical properties while Chapter 8 focusses on the scratch resistance behaviour of alumina nano-composites. Chapter 9 describes processing, electrical properties and bioactivity of bioglass nano-composites. Finally a summary of the thesis and prospects of future work are provided in Chapter 10.

Chapter 2 Review of graphene-ceramic matrix composites

2.1 Introduction

The main purpose of this literature survey is to give a comprehensive picture of the current state of the art on graphene ceramic composites. The review includes: synthesis of graphene (section 2.2); fabrication and consolidation methods for preparation of GCMC (sections 2.3 and 2.4); structural, functional and biological properties (sections 2.5, 2.6 and 2.7); and future research trends (section 2.8). The content of the review is outlined in **Figure 2.1**.

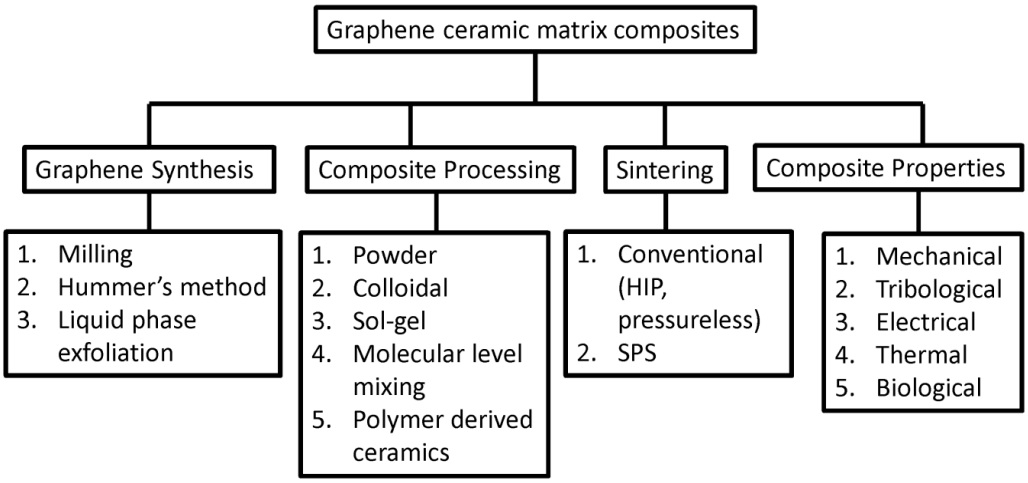

Figure 2.1 Illustrates the topics covered in the review.

2.2 Production of Graphene-Ceramic Composite

2.2.1 Graphene Synthesis

In the papers published on graphene ceramic composites, the main challenge has been to produce good quality graphene. So far three methods have mainly been used to produce graphene using commercially available graphite. One relies on preparing graphene from graphite by breaking it using high energy milling while mixed with the ceramic matrix powder. In the second method graphite is oxidised using Hummer's method and then dispersed in a solvent using mild sonication to produce graphene oxide (GO). Third method uses ultrasonic energy to remove layers of graphite and produce graphene in a polar solvent. All methods use top down approaches and require overcoming the cohesive forces between the graphitic planes in order to produce graphene from graphite. The details of the methods used for graphene synthesis is described in sections 2.2.1.1, 2.2.1.2 and 2.2.1.3.

2.2.1.1 In situ synthesis using high energy milling

In the work of Fan et al. [15] they synthesized graphene with a ceramic powder by planetary milling for long durations. They used commercially available expandable graphite (160–50 N, Grafguard, USA) and heated it to 1000 ^{o}C for 60 seconds under a nitrogen atmosphere. This sudden heating allowed the graphite to expand in the direction perpendicular to the plane direction (i.e., c-axis direction) making it easier to be exfoliated during planetary milling. After this the expanded graphite powder was mixed with Al_2O_3 powder using planetary ball milling for 30 hours using N-methyl-pyrrolidone (NMP) as the dispersing media.

Tapasztó et al. [30] used a similar method with a Si_3N_4 matrix. Using a high efficiency union process type attritor mill for 3 hours they produced graphene from

expanded graphite in a Si_3N_4 matrix. They reported producing graphene with lateral dimensions of a few microns and thickness of a few nanometres (1-30 layers). Kun et al. [31] have compared the mechanical properties (bending strength, elastic modulus) of graphene composites produced by mechanical milling with commercially available exfoliated graphite nano-platelets (5-8 nm). They found that in situ produced graphene produced composites with better mechanical properties as compared to the commercial material. They used high efficiency attritor milling at 600 rpm for 30 min for mixing Si_3N_4 powder with the graphene using ethanol as the dispersing media. **Figure 2.2 a)** illustrates the production of graphene using planetary ball milling, which involves mechanical exfoliation produced by the shear stresses generated during ball-ball contacts [15].

In work done by Ting et al. [16], they showed the effect of ball milling time on the synthesis of graphene using a planetary ball mill with Al_2O_3 powder. They used a rotation speed of 250 rpm with a powder to ball ratio of 1:30 and rotation times ranging from 10-30 hours. They reported that after 10 hours of ball milling the majority of the graphite sheets were not broken and some exfoliation of graphene occurred. With further increment of the milling time, the sizes of the graphite sheets were reduced and thinning was observed. However, long ball milling times lead to crumpling and rolling of the graphene sheets which results in damaging of the graphene flakes. They reported producing 3-4 nm thick graphene sheets after 30 hours of milling. **Figure 2.2 b)** shows a TEM image of the alumina-graphene powder mixture milled for 30 hours; the graphene flakes are 3-4 nm in thickness.

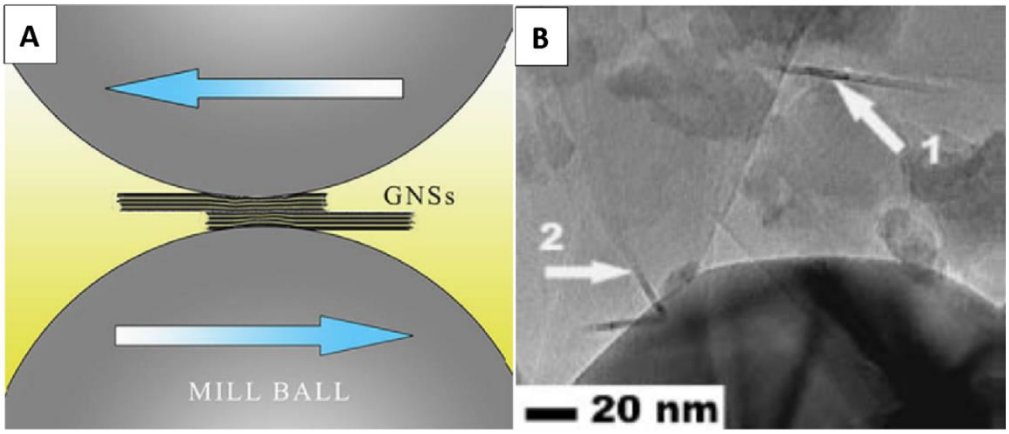

Figure 2.2 a) Production of Graphene Nano-sheets from graphite flakes during ball milling with arrows indicating direction of shear stress; and **b)** HRTEM image of Al_2O_3-5vol% C powder mixture milled for 30hour. Adapted from references [15, 16] respectively.

2.2.1.2 Graphene from Graphitic Oxide (Modified Hummer's Method)

To produce graphitic oxide using modified Hummer's method, commercially available graphite powder is treated with Sodium Nitrate ($NaNO_3$), Sulphuric acid (H_2SO_4) and Potassium Permanganate ($KMNO_4$) at 0^oC for 2 hours. After stirring the mixture for 30 min at room temperature, distilled water is slowly added while maintaining the temperature below 98 ^oC for 3 hours. The mixture is subsequently treated with hydrogen peroxide (H_2O_2) followed by filtering and washing with distilled water. After dispersing the mixture in distilled water and ultasonicating for 15 minutes, the dispersion is centrifuged and stable supernatant containing GO is collected[32-34]. **Figure 2.3 a)** illustrates the typical chemical structure of GO produced by hummer's method [32, 34]. The obtained GO can be used with hydrophilic solvents to prepare ceramic graphene composites. Generally, GO prepared using this method forms colloids stable in water, contains negative surface

charge, is ~1 nm thick and electrically insulating. **Figure 2.3 b)** is an AFM image of exfoliated GO with 1nm thickness [34, 35]. The electrical conductivity of GO can be partially restored by chemical reduction [36]. Reduction of GO to graphene can be characterized using Raman spectroscopy as shown in **Figure 2.3 c)** pristine graphite, displays only a G band mainly due to stretching of sp2 bonds [37], while the Raman spectrum of GO has the G band and an additional D band corresponding to reduction in size of the in plane sp2 domains due to oxidation. Raman spectra of reduced GO also contain D and G band, the increased I_D/I_G ratio is due to decrease in the average size of the sp2 domain upon reduction [35].

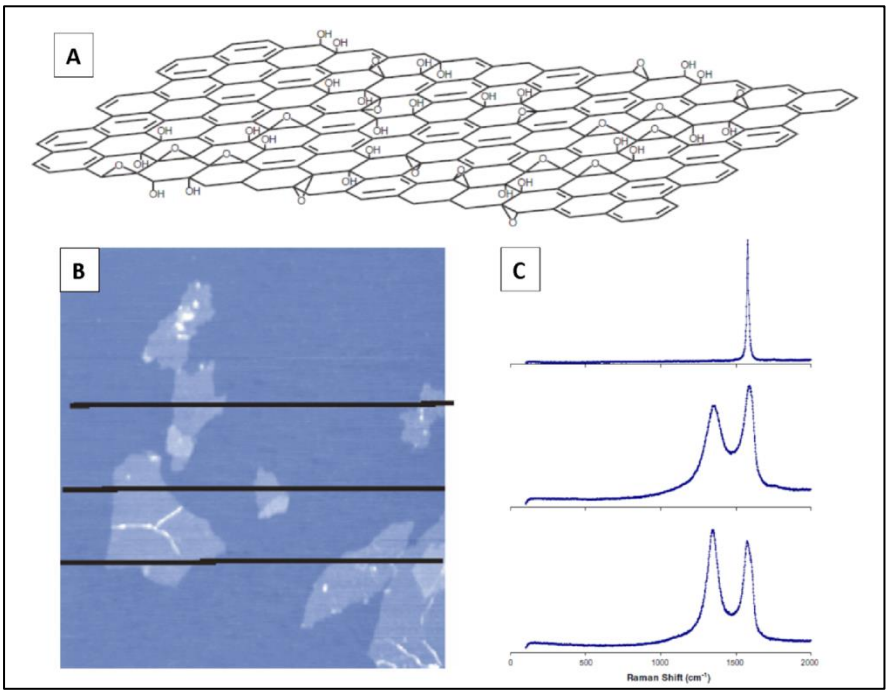

Figure 2.3 a) Typical chemical structure of GO produced by Hummer's Method; **b)** AFM image of exfoliated GO sheets in non-contact mode; **c)** Raman spectra of Graphite (top), GO (middle) and Reduced GO (bottom). Adapted from references [32, 34, 35].

Similarly, Wang et al. [38] produced graphitic oxide suspensions using modified Hummer's method followed by ultrasonication. The suspension was mixed with alumina powder using a colloidal processing route. GO was reduced to graphene using hydrazine monohydrate at 60 ^{o}C for 24 hours.

Walker et al. [27] used rapid thermal expansion (>2000 ^{o}C/min) of graphite oxide to produce graphene. They were able to produce 3-4 layer graphene with average thickness of less than 2 nm. Because of the thermal shock the majority of the oxygen moieties were expelled, converting GO to graphene, as verified by elemental analysis.

In general, producing graphene from graphitic oxide is a two-step process, in step one graphitic oxide is exfoliated to obtain GO using different mechanical or thermal methods and in step two GO is converted to graphene using different chemicals including hydrazine, sodium boro-hydride, hydroquinone or by thermal treatment in a reducing atmosphere [33].

The major problems associated with both mechanical milling and hummer's method to synthesise graphene are: 1) In-situ production of graphene using high energy milling method has lack of control over the quality. This method produces unexfoliated graphite crystallites in the ceramic matrix and graphene flakes with various size and thicknesses, which in turn can negatively affect the properties of graphene ceramic composites. 2) Hummer's method damages the graphene flakes by oxidation, which produces a lot of structural defects, degrading the physical properties compared to those of pure graphene. Also, it has been reported that the electrical conductivity of reduced GO is much lower than that of pristine graphene because significant amounts of oxygen is still present in the reduced GO, which was

confirmed by elemental analysis [34]. It should be noted that although authors have reported using graphene/GO of various thicknesses, most of the present work reports using graphene/GO with lateral dimensions of 200 nm to few micrometres. In order to prepare high quality GCMC we need to solve these problems using methods that have better control over the structural and chemical quality of graphene.

2.2.1.3 Liquid phase exfoliation (Graphene from graphite flakes using ultrasonic energy)

The main problem associated with producing graphene using high energy ball milling is we do not have proper control over the quality of graphene flakes. When using high energy ball milling method we end up with thick non exfoliated graphite flakes which can influence the properties of the composites. While in the case of Hummer's method we use strong acids to oxidise graphite which in turn damages the graphene sheets and thus influences its properties. In order to solve these problems authors have used liquid phase exfoliation method. Liquid phase exfoliation can produce good quality graphene flakes without the use of strong acids and we can remove the unexfoliated graphite by centrifugation thus solving both problems associated with previous described methods.

Liquid phase exfoliation uses the idea of ultrasonic energy to separate the graphite flakes layer by layer. In a typical setup for producing graphene using liquid phase exfoliation method graphite flakes are added to a polar solvent (NMP, DMF) and the suspension is sonicated using sonic tip or sonic bath for long times (24 hours). With the use of sonic energy the layers of graphene are separated from the bulk graphite while solvent stops the restacking of graphene layers by covering the graphene flakes. The choice of solvent plays a critical role in achieving good

exfoliation. According to Coleman [39], if the surface energy of solvent matches the surface energy of graphite we get better exfoliation of graphite in the solvent to produce graphene. After exfoliation the prepared suspension is centrifuged to separate the unexfoliated graphite flakes and the top supernatant which contains the good quality graphene is collected. Typically the length of graphene flakes produced using liquid phase exfoliation ranges from 0.2 to 4 μm while the thickness varies from 1-10 layers. **Figure 2.4 a)** shows the change in concentration of graphene with sonication time. As the sonication time increases more graphene flakes are exfoliated from graphite and thus the concentration of the suspension increases. For longer sonication times the concentration of the suspensions starts decreasing probably due to oxidative degradation of solvent [40]. **Figure 2.4 b)** shows the TEM image of graphene produced using liquid phase exfoliation method. It is also possible to separate the graphene flakes produced using liquid phase exfoliation according to their size distribution. Khan et al. [41] separated the graphene according to various sizes by centrifuging graphene suspension at various centrifugation speeds ranging from 4000-500 rpm with higher centrifugation rates resulting in smaller flakes and vice versa.

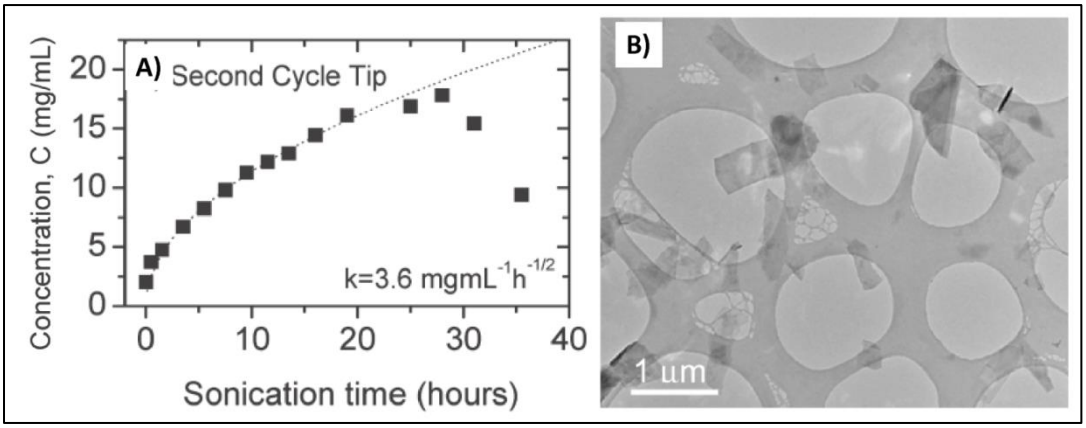

Figure 2.4 a) Change in concentration of graphene with sonication time; and **b)** TEM images showing graphene flakes produced using liquid phase exfoliation method [40].

2.3 Graphene Dispersions in the Ceramic Matrix

Another challenge associated with preparing GCMC is to develop processing routes that produce good dispersion of graphene in the ceramic matrix. The quality of the graphene dispersion in a ceramic matrix significantly affects the final properties of the composite. There has been a considerable amount of work done with CNTs in the past decade to produce well dispersed ceramic composites [5, 8, 9, 42, 43]. As graphene shares a similar chemical structure with CNTs, it is possible to use CNTs as a reference in terms of processing conditions to produce well dispersed graphene ceramic composites. The advantage of graphene over CNTs is related to their better processesability because of the high specific surface area and the 2D geometry of graphene flakes [16].

According to the papers published in the field of GCMC, researchers have mainly used either “powder processing” or “colloidal processing” to produce well dispersed

composites. Both of these techniques will be discussed in detail in sections 2.3.1.1 and 2.3.1.2. The physical principle behind these techniques consist of breaking the graphene agglomerates by applying shear forces, either by using high energy milling or ultrasonic probes. Graphene surface engineering either by direct functionalization or by using surfactants allows the preparation of stable dispersions as demonstrated in the case of CNTs. This is a new field, and there is a lot of scope for further research to investigate scalable and environmentally friendly processing routes for preparing well dispersed GCMCs.

2.3.1 Graphene-Ceramic Composite Processing Methods

2.3.1.1 Powder Processing

Powder processing has been very commonly used for the processing of ceramic-CNTs composites [44] with different matrices, including alumina [45], zirconia [46], silicon nitride [47], silica [8] and boro-silicate glass [48]. This technique has produced mixed results for ceramic-CNTs composites depending on the matrix used. In this technique the filler material is first de-agglomerated using various methods including ultrasonication and then mixed with the ceramic powder in a solvent, using conventional ball milling or high energy ball milling to produce slurries of well dispersed ceramic composites. In the research reported so far, researchers were able to produce GCMC with alumina [15] and silicon nitride [30] matrices. In their work they had used NMP/ethanol as the dispersing media with either planetary or attritor ball milling, with the milling time ranging from 3-30 hours, and reported producing well dispersed graphene-ceramic composites. As graphene, is easier to process compared to CNTs, powder processing is a promising method to produce well dispersed composites. In a work by Tapasztó et al. [49] they

produced silicon nitride-SWCNTs, MWCNTs and few layer graphene composites using attritor milling and compared the quality of the dispersion of the carbon nano-materials using the same processing method. They used small angle neutron scattering experiments and SEM to confirm the quality of the dispersions and found that graphene can be more efficiently dispersed in the ceramic matrix compared to CNTs. **Figures 2.5 a) and 2.5 b)** are SEM images of fractured surfaces of graphene-Si_3N_4 (1 wt % and 3 wt %) samples, produced by powder processing. Arrows in the figure show the location of embedded graphene[31]. Michálková et al. [50] compared the homogenisation of graphene nanoplatelet in silicon nitride matrix using various methods including attritor milling, ball milling or planetary ball milling and found that best results were obtained for composites prepared using planetary ball milling although all the composites prepared showed a decrease in mechanical properties compared to pure silicon nitride.

2.3.1.2 Colloidal Processing

Colloidal processing is a technique for producing ceramic suspensions on the basis of colloidal chemistry. This technique is used to prepare graphene-ceramic mixtures by combining colloidal suspensions of graphene and ceramic powders. Typically, the same solvent is preferred for both the materials in order to provide a uniform dispersing medium while mixing. The suspensions prepared are mixed slowly by magnetic stirring/ultrasonication in order to favour uniform distribution of the graphene into the matrix.

Colloidal processing also requires surface modification of both the graphene and the matrix powder; this can be achieved either by direct functionalization (i.e. oxidation) or by using surfactants which generate same/opposite electric charges.

Modification generally involves generating opposite electric charges between the ceramic particles and the graphene, and the process is commonly known as hetero-coagulation. According to the literature hetero-coagulation has been demonstrated to be a very effective route for producing well dispersed ceramic-CNTs composites [5, 51].

Wang et al. [38] employed hetero-coagulation to produce well dispersed graphene-alumina composites. In their work a suspension of GO was prepared by ultrasonication in water. Separately, they also produced an alumina suspension in water by sonication for 30 minutes. Finally, well dispersed graphene-alumina composites were achieved by adding GO drop wise to the alumina suspension under magnetic stirring conditions.

Walker et al. [27] successfully produced well dispersed graphene-Si_3N_4 composites with different concentrations using a colloidal processing route. In their work they used cetyl trimethyl ammonium bromide (CTAB) as a cationic surfactant to produce positive charges on both the ceramic and graphene surfaces. It is worth noting that in order to produce good dispersion using a surfactant system the concentration of surfactant should be above a critical micelle concentration. They used 1 wt% of CTAB to disperse both graphene and Si_3N_4 and developed an electrostatic repulsive forces on the surfaces of the materials to obtain good dispersion of graphene in the Si_3N_4 matrix. **Figure 2.5** illustrates **c)** low and **2.5 d)** high resolution SEM images of exfoliated graphene platelets mixed with Si_3N_4 particles after colloidal processing [27]. The images clearly indicate that Si_3N_4 particles are well dispersed over the surface area of the graphene platelets.

In interesting work by Rincón et al. [52, 53], they used tape casting to produce alumina (A), alumina-3YTZP (AZ), alumina-3YTZP-GO (2 vol%) (AZGO)

multilayer laminate composites. Firstly they optimised the processing conditions for preparing stable colloidal suspensions of A, AZ and AZGO in DI water using poly acrylic acid as the deflocculant. After preparing stable suspensions the rheological properties of A, AZ and AZGO were optimised. In order to get uniform dispersions without large agglomerates they sonicated the prepared suspensions and also optimised the sonication time. Finally the suspensions with the best rheological properties were tape caste after adding acrylic latex emulsion for tape casting. They conducted the tape casting on Mylar film for A, AZ and AZGO suspensions and the produced tapes were left to dry at room temperature for 24 hours. In the second step three kinds of alternating layers of laminates were produced: 1) layers of A-AZ, 2) AZ-AZGO and 3) A-AZ-AZGO. They punched the tapes of A, AZ and AZGO in 20 mm discs and the discs were laminated applying small pressure and using a few drops of water as the gluing agent. Symmetric laminates with 9 layers were obtained. Finally the prepared laminates were sintered in SPS at 1400 ^{o}C. In this work they demonstrate the possibility of making multilayer laminates using the tape casting method.

2.3.1.3 Sol-Gel Processing

Sol gel processing is another route for producing graphene glass/ceramic composites. This method basically requires creating a precursor that can undergo condensation to produce a green body with well dispersed graphene. In this technique, first a stable suspension of well dispersed graphene is prepared to which TMOS (tetra methyl ortho silicate) is added and the suspension is sonicated to obtain a uniformly dispersed sol. To initiate gelation, a catalyst such as acidic water is added which promotes hydrolysis and composite gels are formed after condensation

at room temperature. This technique is mainly used for creating silica nano composites. There are a number of reports in the literature on preparing well dispersed CNT-silica composites using the sol gel method [54, 55].

In work reported by Watcharotone et al. [29], they used the sol-gel technique to prepare graphene-silica films that can be used as transparent conductors. In their work they prepared GO using modified Hummer's method that was then exfoliated in a mixture of water-ethanol to prepare a stable GO suspension. Subsequently TMOS, a silicate precursor, was added to the above suspension to create a very stable GO containing sol that can be stored for several days. Instead of preparing gels from these sols, thin transparent films were prepared by spin coating on borosilicate glass or silicon. The solvent was evaporated from the prepared films, which were further treated in a reducing environment of hydrazine mono hydrate, which reduced the GO to graphene sheets. **Figure 2.5 e) and 2.5 f)** are SEM images of 6.6 wt% graphene-silica composite films produced by sol-gel processing. Arrows in the images indicate the edges of the graphene sheet.

Other than preparing composite films, the sol-gel technique has been used to prepare graphene composites for various applications including sensors [56], electrode materials for solar cells [57], Li-ion batteries [58] and catalysts [59, 60]. For example Zeng et al. [56] used this technique to prepare SiO_2 coated GO composites for electro chemical sensing of dopamine. Similarly, Cheng et al. [57] used an organic sol-gel process to produce graphene aerogels to produce highly efficient counter electrode material for dye sensitized solar cells. Yang et al. [58] used a template free sol-gel route to produce 3D porous graphene-$LiFePO_4$ hybrid cathodes with enhanced efficiency for Li-ion batteries.

The advantages of using sol-gel processing are that it can be used to obtain transparent and mechanically stable films and bulk materials. Because the technique requires liquid precursors it is easy to prepare doped materials or well dispersed composites by dissolving or suspending materials in a liquid phase [54].

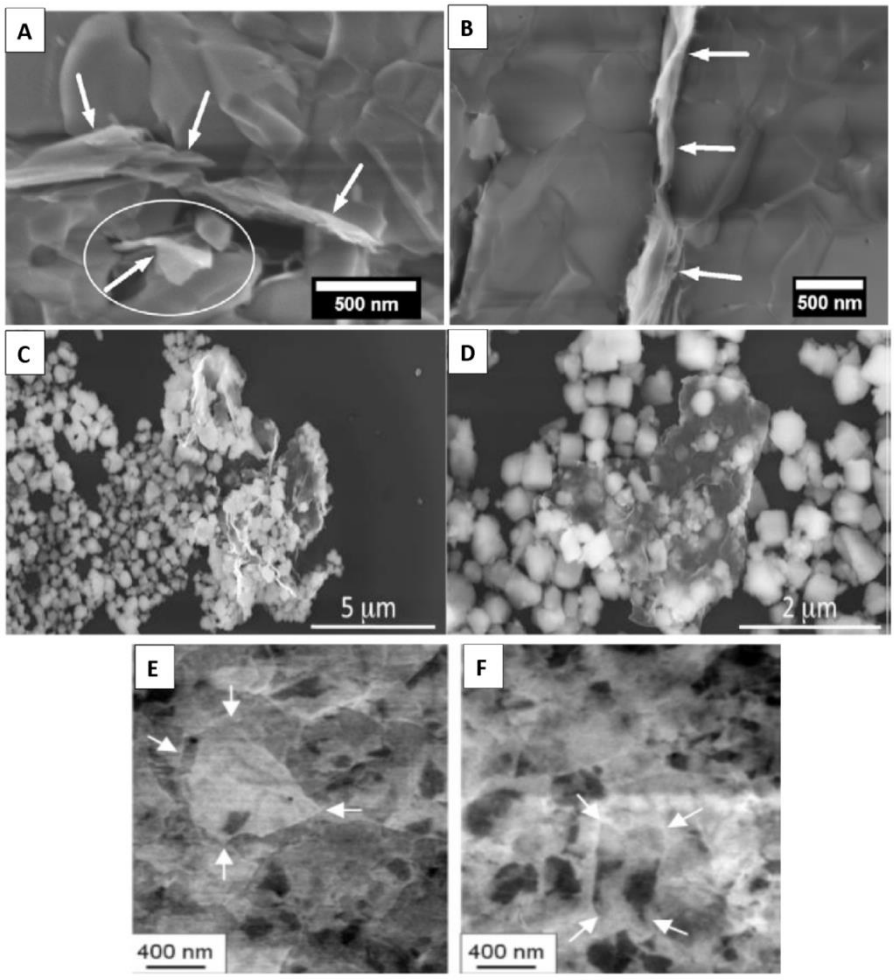

Figure 2.5 SEM images of: **(a)** fractured surfaces of Graphene-Si_3N_4 (1 wt %) sample; and **(b)** Graphene-Si_3N_4 (3 wt %) sample produced by powder processing; **(c)** and **(d)** Images after colloidal processing of Graphene-Si_3N_4 showing decorated graphene flakes with well dispersed Si_3N_4 particles; **(e)** and **(f)** GO-Silica (6.6 wt%) composite films produced using sol-gel processing. Adapted from references [27, 29, 31] respectively.

2.3.1.4 Molecular Level Mixing

In order to have better control over the microstructure and properties of ceramic-graphene composites authors have tried to control the processing of graphene and ceramic particles at the molecular level. In molecular level processing authors use functionalised graphene in a solvent and mixed it with a ceramic salt that can be converted to ceramic particles by heat treatment or other processing methods. By doing this they can coat the graphene with ceramic particles at the molecular level. This type of processing has two advantages: 1) it ensures good dispersion of graphene in the ceramic matrix; and 2) it provides better interfacial bonding between graphene and ceramic particles at the molecular level. This type of method has been used in the past for fabricating Copper-CNTs composites [61].

In interesting work by Lee et al. [62], they used a molecular mixing process to produce alumina-reduced (r) GO composites with different GO loading. In their work, a GO suspension was produced using distilled water as the solvent and the alumina precursor salt ($Al(NO_3)_3.9H_2O$) was added to this suspension followed by 12 h magnetic stirring. After mixing, the solution was vaporised at 100 ^oC and the dried powders were oxidised at 350 ^oC in air to produce alumina particles from precursor salt. The powders were further planetary ball milled for 12 h and well dispersed alumina-rGO powders were collected. **Figure 2.6** shows a schematic for producing alumina-rGO composite powders using molecular mixing. Aluminium (Al) nitrate is thermally decomposed in to Al ions while hydroxyl and carboxylic groups present on the surface of GO react with Al ions at the molecular level resulting in heterogeneous nucleation of Al ions on to GO surface. The coating of Al ions on to the surface of GO avoids the agglomeration of GO flakes. In the final step water is removed resulting in the formation of alumina coated GO powders.

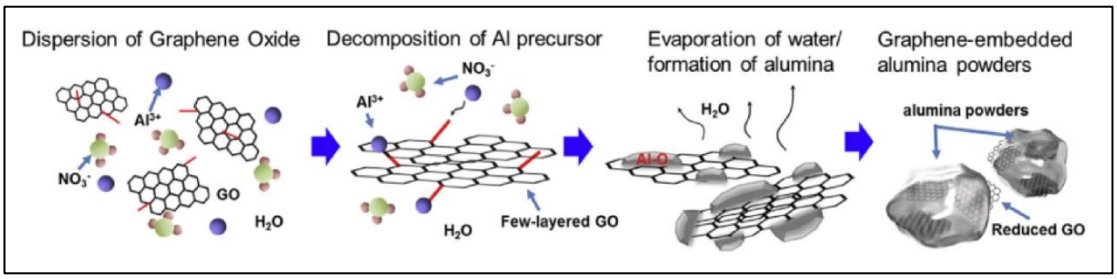

Figure 2.6 Schematic showing the fabrication of alumina-rGO powders using molecular mixing method [62].

2.3.1.5 Polymer Derived Ceramics

Polymer derived ceramics (PDC) is a processing route for producing ceramic fibres, layers or composite materials that are difficult to produce using conventional powder technology. Typically preceramic polymers (polysilazanes, polysiloxanes, and polycarbosilanes) are processed and shaped using conventional polymer-forming techniques such as polymer infiltration pyrolysis (PIP), injection molding, coating from solvent, extrusion, or resin transfer molding (RTM). After processing, PDCs are synthesized by direct thermal decomposition of preceramic polymer precursors, which can be either in liquid form, melt form or as an organic precursor. Other than producing unconventionally shaped ceramic components and devices, PDCs in general exhibit enhanced thermo-mechanical properties, high chemical durability, high creep resistance and low sintering temperatures [63].

They also have advantages over other techniques like sol gel as they do not have any drying problems that hamper the possibility of fabricating bulk components, do not need long processing times for gelation and drying, do not require flammable solvents, can be processed in the molten state and their solutions are stable with time [63, 64].

The PDC technique is particularly suitable for fabrication of ceramic nano-composites because the desired dispersion of nano-filler (CNTs, graphene) is relatively easy to produce in liquid phase precursors just prior to pyrolysis. It is also possible to control the interface of ceramic and nano-filler by either functionalizing the surface of the nano-filler or modifying the chemistry of the precursors, or both. In the last decade the PDC technique has been used to produce CNTs-ceramic composites with enhanced mechanical and functional properties[65, 66] for various applications including laser thermal detectors [67], and anode material for Li-ion batteries [68].

Ji et al. [69] used the PDC technique to produce graphene nano sheet (GNS) and silicon oxycarbide (SiOC) composites to be used as anode material for Li-Ion batteries. GNS and SiOC composites were fabricated by dispersing the GO powder into a polysiloxane (PSO) precursor liquid followed by crosslinking and pyrolysis at 1000 ^{o}C in argon for 1 hour, reducing GO to GNS and PSO to SiOC. Composites with up to 30 wt% loading were fabricated using this technique. They found that the discharging capacity of GNS-SiOC composite was higher than the graphite reference and SiOC monolithic. Both initial discharge capacity and reversible capacity increased linearly with increasing concentration of GNS in the SiOC matrix.

2.4 Sintering Techniques

Conventional sintering technique, such as, pressureless sintering require relatively long processing times and high temperature to prepare dense materials, both factors results in grain growth and simultaneous degradation of the nano-fillers (i.e. graphene, CNTs) in ceramic composites [70]. In order to avoid these problems

for ceramic graphene composites, novel sintering techniques are being exploited with the aim of both lowering the sintering temperature and shortening the dwell times. Apart from conventional sintering, Hot Pressing (HP) and Hot Isostatic Pressing (HIP) allow sintering of ceramics at lower temperatures by the application of pressure, while other sintering techniques, such as, Spark Plasma Sintering (SPS) and microwave sintering, involve the use of electromagnetic fields to obtain high heating rates in order to decrease the sintering temperature and dwell times.

2.4.1 Spark Plasma Sintering (SPS)

In terms of sintering carbon containing composites like graphene or CNTs ceramic composites, reducing the sintering temperature and time is critical in order to avoid degradation. Degradation of carbon nanotubes during conventional sintering has been reported in the literature [3, 70-75] due to the relatively long sintering time (2-10 hours) and high temperatures involved (> 800 ^{o}C) in the sintering process. In order to avoid these problems, rapid sintering techniques such as Spark Plasma Sintering (SPS) have been used to sinter GCMC. SPS is a pressure and electric field assisted sintering technique. The technique uses joule heating of the sample powder, punch and die, to generate very high heating rates (few hundred ^{o}C/min) [76]. Pressure as high as 1 GPa [77] can also be applied to the samples in order to sinter them quickly (3-10 minutes) and at relatively low temperatures. This minimizes any degradation of the nano-filler and grain growth. SPS is useful for investigating the sintering behaviour of ceramic composites with nano-fillers because it can rapidly achieve isothermal conditions, enabling densification to be studied over a wide range of densities [78, 79]. Milsom et al. reported a significant decrease in the sintering activation energy for the Y_2O_3 partially stabilised zirconia with the addition of CNTs

above the percolation threshold. The lower activation energy is attributed to the intrinsic effect of the carbon nano-filler. Other advantage of using SPS for sintering of ceramic-graphene composites is in-situ reduction of GO and alignment of graphene in the ceramic matrix. The high temperature and reducing environment of SPS results in the in-situ reduction of GO to graphene in a single step without the need of additional methods to reduce GO [80]. Alignment of graphene has been observed in a direction perpendicular to the applied pressure during SPS. The main reason for the alignment in the case of graphene compared to CNTs is the morphology of the graphene flakes. Since graphene is a two dimensional material during sintering when pressure is applied it tends to align naturally in a direction perpendicular to the applied pressure. Centeno et al. [80] used Raman spectroscopy to confirm the alignment of graphene in an alumina matrix. They did Raman scans on the surface of graphene-alumina composites in both the parallel and perpendicular directions to the applied pressure during SPS and found that the I_D/I_G ratio for graphene was different in both cases. I_D/I_G ratio on the sample surface perpendicular to the pressing direction was higher (I_D/I_G = 1.13) than the I_D/I_G ratio on the sample surface parallel to the pressing direction (I_D/I_G = 0.83). **Figure 2.7** shows the Raman spectra of graphene-alumina composites taken in two different directions. The I_D/I_G ratio in the Raman spectra is a measure of defects in graphene. In the case of graphene, the edges of the graphene flakes contribute to the high I_D peak intensity. Since graphene is aligned in a direction perpendicular to the applied pressure in SPS we see fewer edges when we do the Raman spectra on graphene alumina composite surface parallel to the pressing direction and more edges in the case of composite surface perpendicular to the pressing direction.

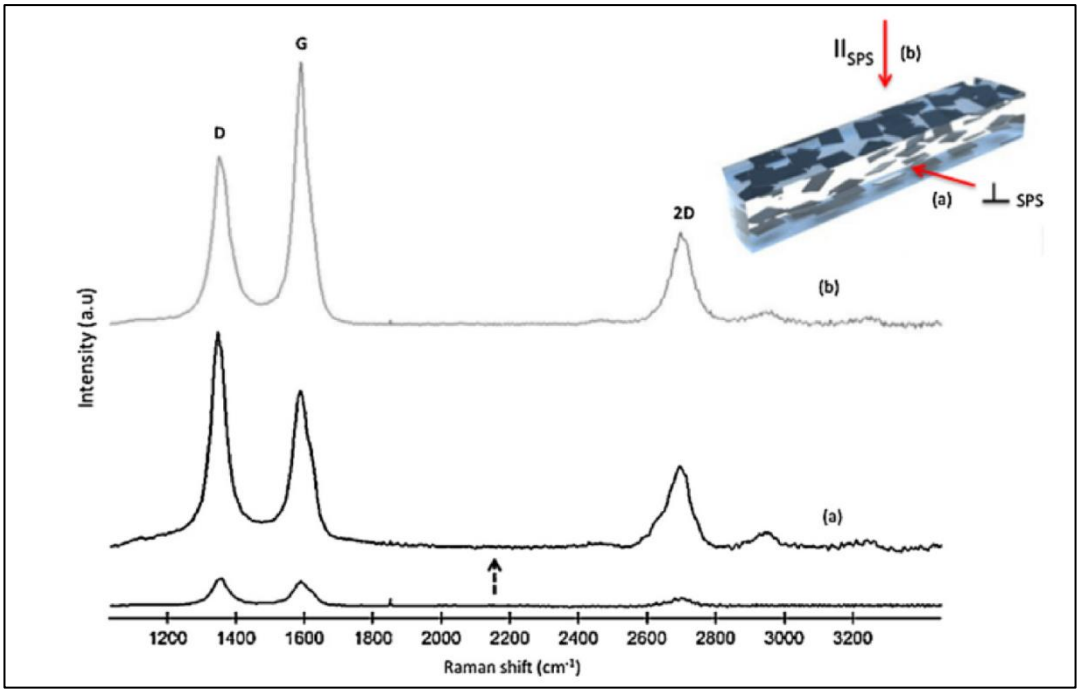

Figure 2.7 Raman spectra of graphene-alumina composites taken in two different orientations: a) perpendicular; and b) parallel to the pressing direction in SPS [80].

2.5 Mechanical Properties and Possible Toughening Mechanisms

Table 2.1 summarizes the mechanical properties of graphene ceramic composites reported in the literature. Several authors have reported an improvement in mechanical properties (with special attention on the fracture toughness) with the addition of graphene to a ceramic matrix.

Table 2.1 Mechanical Properties of Graphene-Ceramic composites as reported in literature.

Matrix material	**Nano-filler Type**	**Nano-filler content**	**Processing Route/ Consolidation Method**	**Relative Density (%)**	**Investigated properties (%) shows improvement in properties compared to monolith**
Si_3N_4 [27]	Reduced GO (thermally)	1.5 vol%	Colloidal/SPS	99.6 %	Fracture Toughness (VI): 6.6 MPa $m^{1/2}$ (235%).
Si_3N_4 [30]	Milled graphene sheets	3 wt%	Powder/HIP	-	Fracture Toughness (Nihara-formula): 3.6 MPa $m^{½}$. Hardness (HV10): 14.3 GPa. Bending strength, 4 point: 654 MPa. Bending strength, 3 point: 900 MPa. Young's modulus: 245 GPa. 10-50% less decrease in properties compared to MWNTs composites.
Si_3N_4 [81]	Exfoliated graphite sheets	3 wt%	Powder/ HIP and SPS	-	Fracture Toughness (VI): 4.29 MPa $m^{1/2}$ (HIP), 3.24 MPa $m^{½}$ (SPS). Hardness (HV): 12.6 GPa (HIP) and 17.37 GPa (SPS). Young's Modulus: 214 GPa (HIP), 227 GPa (SPS).
Si_3N_4 [31]	Milled, commercially available graphene platelets and	1 and 3 wt%	Powder/HIP	~98 %	Bending Strength: 643 MPa-1 wt% and 452 MPa-3 wt %, 4 point. Elastic Modulus: 239

	*multilayer graphene				GPa-1 wt% and 188 GPa-3 wt %.
Si_3N_4 [82]	Exfoliated graphite, nano graphene and *multilayer graphene platelets	1 wt%	Powder/HIP	-	Fracture Toughness (VI): 9.92 MPa $m^{1/2}$ (45%) Hardness (HV): 16.38 GPa (7%)
Al_2O_3 [38]	Reduced GO (chemically)	2 wt%	Colloidal/SPS	96 %	Fracture Toughness (SENB): 5.21 MPa $m^{1/2}$ (53%).
Zirconia toughened alumina (ZTA) [83]	Graphene platelet	0.8 vol%	Powder/SPS	98 %	Fracture Toughness (SENB): 9.05 MPa $m^{1/2}$ (40%).
Al_2O_3 [84]	Graphene platelet	0.38 vol%	Powder/SPS	99.5 %	Flexural Strength: 523 MPa (30%) Fracture Toughness: 4.49 MPa $m^{1/2}$ (27%) Hardness (HV): 17.6 GPa (-2%)
Al_2O_3 [80]	Reduced GO (in-situ SPS)	0.22 wt%	Colloidal/SPS	99%	Fracture Toughness (SENB): 5.1 MPa $m^{1/2}$ (50%). Fracture Strength: 630 MPa (80%)
TaC [85]	Graphene nano platelets	5 vol%	Powder/SPS	98.8%	Fracture Toughness (VI): 11.1 MPa $m^{1/2}$ (99%). Nano Hardness: 20.6 GPa (-27%) Elastic Modulus: 490 GPa (-10%) Grain size: 1.4 µm (-70%)
Si_3N_4 [86]	Exfoliated graphite,	1 wt%	Powder/GPS	-	Fracture Toughness (VI): 8.5 MPa $m^{1/2}$

	nano graphene and *multilayer graphene platelets				(35%)
$CaSiO_3$ scaffolds [87]	Graphene	0.5 wt%	Powder/SLS	-	Fracture Toughness (VI): 1.73 MPa $m^{1/2}$ (46%) Compressive Strength: 42.4 MPa (142%) Compressive Modulus: 160.7 MPa (37%)
Al_2O_3 [88]	Graphene nano sheets	0.1, 0.2 wt%	Powder/HIP	99%	Fracture Toughness (SENB): 6.6 MPa $m^{1/2}$ (44%). Bending Strength: 542 MPa (30%)
Al_2O_3 [89]	Un-oxidised graphene, GO, reduced GO	0.25 vol%	Colloidal/Pressure less sintering	-	Fracture Toughness (SENB): 4.72 MPa $m^{1/2}$ (48%). Flexural Strength: 424 MPa (28%) Wear Rate: $2.12x10^{-4}$ mm^3/N.m (95%)
Al_2O_3 [62]	Reduced GO	3 vol%	Molecular Level Mixing/SPS	-	Fracture Toughness (VI): 10.5 MPa $m^{1/2}$ (130%) Hardness (HV): 22.5 GPa (13%) Flexural Strength: 424 MPa (22%)
SiO_2 [90]	Reduced GO	10 vol%	Solgel/SPS	98.9%	Fracture Toughness (VI): 3.56 MPa $m^{1/2}$ (50%) Hardness (HV): 6.30 GPa (-30%) Elastic Modulus: 44.5 GPa (-35%)
$CaSiO_3$ [91]	Reduced GO	1 wt%	Hydrothermal/HIP	94%	Fracture Toughness (VI): 2.76 MPa $m^{1/2}$

					(123%) Hardness (HV): 4.54 GPa (40%) Elastic Modulus: 115 GPa (52%)
Hydroxyapatite [92]	Reduced GO	1 wt%	Colloidal/SPS	-	Fracture Toughness (VI): 3.94 MPa $m^{1/2}$ (203%) Hardness (HV): 4.3 GPa (26%) Elastic Modulus: ~150 GPa (48%)
Hydroxyapatite Coating [93]	Reduced GO	1 wt%	Vacuum Cold Spray	-	Fracture Toughness (VI): 0.42 MPa $m^{1/2}$ (280%) Hardness (HV): 0.22 GPa (30%) Elastic Modulus: 4.25 GPa (40%)
Hydroxyapatite [94]	Graphene Nano Sheets	0.5 wt%	Colloidal/SPS	-	Bending Strength: 96 MPa (12%)

VI- Vickers Indentation

SENB- Single Edge Notch Beam

SPS- Spark Plasma Sintering

HIP- Hot Isostatic Pressing

GPS- Gas Pressure Sintering

SLS- Selective Laser Sintering

*Mechanical properties reported in table for multilayer graphene composites.

Researchers have mainly used two techniques to measure the fracture toughness: Vickers Indentation fracture toughness (VI); and Single Edge Notched Beam (SENB). Vickers indentation is the most commonly used technique. Although the VI technique has advantages in terms of ease of use [2, 95], it should be noted that it does not provide absolute values for fracture toughness because it measures the toughness of the material locally in the sample under a complex stress field [96,

97]. Whereas the SENB method gives the fracture toughness values for the bulk under mode I crack opening [98]. Therefore it is recommended to use the SENB method if absolute fracture toughness values are required. The VI method can be used for simply comparing the fracture toughness and behaviour of different materials. Most authors have used the VI method due to the limited availability of samples, and calculated fracture toughness using Anstis' equation [99].

$$K_{IC} = 0.16\,(E/H)^{1/2}\,(P/c_o^{3/2}) \qquad (2.1)$$

Where, E is the modulus of the composites, H is the measured hardness, P is the applied load and c_o is the radical crack length.

In recent work by Walker et al. [27], they reported an improvement of ~235% in fracture toughness with only a 1.5 vol% loading of graphene in a Si_3N_4 matrix measured using VI method. The graphene appeared to be wrapped or anchored around the Si_3N_4 grains and formed a continuous network along the grain boundaries. They reported some unexpected toughening mechanism for these composites. Cracks were not able to propagate through the graphene walls and were arrested. Graphene blocked the in plane propagation of cracks, therefore forcing cracks to deviate around the graphene sheets. This kind of toughening mechanism is new compared to what has previously been observed for particulate, CNT and fibre-reinforced ceramic materials.

In work by Tapaszto et al. [30], they compared the mechanical properties of CNT and graphene-Si_3N_4 composites for 3 wt% loading. According to them graphene was easy to process and disperse compared to CNTs, which resulted in

better mechanical properties. There was an enhancement of 10-50% in the mechanical properties (fracture toughness, hardness, bending strength, Youngs modulus) for graphene composites compared to CNT composites with the same loading, although the overall properties for both composites decreased compared to monolithic Si_3N_4. **Figure 2.8** shows different mechanical properties of few layer graphene and CNT reinforced silicon nitride composites prepared under the same experimental conditions [30]. In other work by the same authors [81] they compared the mechanical properties of reinforced Si_3N_4 composites processed by different sintering techniques such as Hot Isostatic Pressing (HIP) at 1700 ^oC/ 20 MPa/ 3 hours and Spark Plasma Sintering (SPS) at 1650 ^oC/ 50-100 MPa/ 3-5 minutes. They found composites prepared by the different sintering techniques possessed different structural and mechanical properties. For example composites prepared using SPS consisted of alpha Si_3N_4 and were therefore stiffer and harder, whereas composites prepared using HIP had elongated β Si_3N_4 grains and were tougher [81].

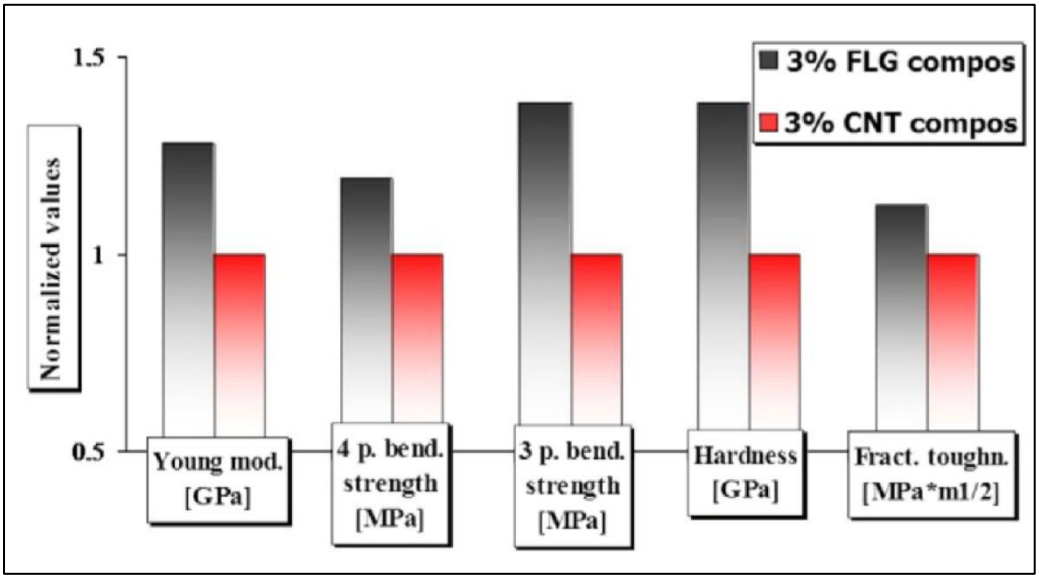

Figure 2.8 Mechanical properties of few layer graphene (FLG) and CNTs reinforced silicon nitride composites. Adapted from reference [30].

Kun et al. [31] prepared 1 and 3 wt% graphene-silicon nitride composites using HIP. They compared the bending strength and elastic modulus of composites reinforced with different types of graphene, namely multilayer graphene (MLG) with thickness of 14 nm, commercially available exfoliated graphite nano-platelets (xGnP) with thickness of 5-8 nm and graphene platelets with thickness of 10-20 nm. They found graphene platelets induced porosity in the samples. As a result of this the elastic modulus and bending strength both decreased with increasing amount of graphene. Better results were obtained for multi layer graphene compared to graphene nano platelets and graphene platelets **(Table 2.1)**. In a similar work, Kvetkova et al. [82] prepared 1 wt% graphene-silicon nitride composites with different graphene nano-fillers. They used multilayer graphene prepared by mechanical milling and commercially available graphene nano platelets. They fabricated silicon-nitride nano composites using HIP. Unlike Kun et al., they reported an improvement in fracture toughness for all the composites using the VI method. There was a reinforcement of ~45% in fracture toughness for multilayer graphene composite. They observed various toughening mechanisms, including crack bridging, crack branching and crack deflection. However, the hardness of all the composites was lower than the pure silicon-nitride material except for the multilayer graphene composite. The decreased hardness was attributed to increased residual porosity, whereas less porosity and smaller grain size explained the higher hardness of multi layer graphene composite. In another work by the same group they compared the effect of different sintering techniques on the mechanical properties of silicon nitirde nano-composites prepared with different kinds of graphene flakes. They compared HIP to Gas Pressure Sintering (GPS) technique and found that nano-composites prepared using GPS showed less improvement in fracture toughness and

hardness values compared to HIP method. Although similar to their previous work best results were obtained for composites prepared with multi layer graphene [86]. In another similar work on silicon nitride matrix Dusza et al. [100] prepared graphene (1wt%)-silicon nitride composites with different size graphene flakes including multi layer graphene (0.5–3 μm), exfoliated graphene platelets (1-25 μm) and nano-graphene platelets (0.5-5 μm). According to them the best results for fracture toughness were obtained for the composites with the smallest graphene size i.e. silicon nitirde-multi layer graphene composites. They reported an improvement of 45% in the fracture toughness.

Figure 2.9 illustrates the various mechanisms of crack toughening involved in GCMC: **Fig. 2.9 a)** shows a radical crack produced by indentation in graphene-Si_3N_4 composites, and crack bridging by graphene is apparent; **b)** shows the three main mechanisms of toughening including graphene sheet pullout, crack bridging and crack deflection in graphene-silicon nitride composites [27]; **c)** crack branching in 1 wt% graphene platelet-silicon nitride composites [82]; and **d)** graphene pull out from multi layer graphene reinforced ZTA nano-composites [83].

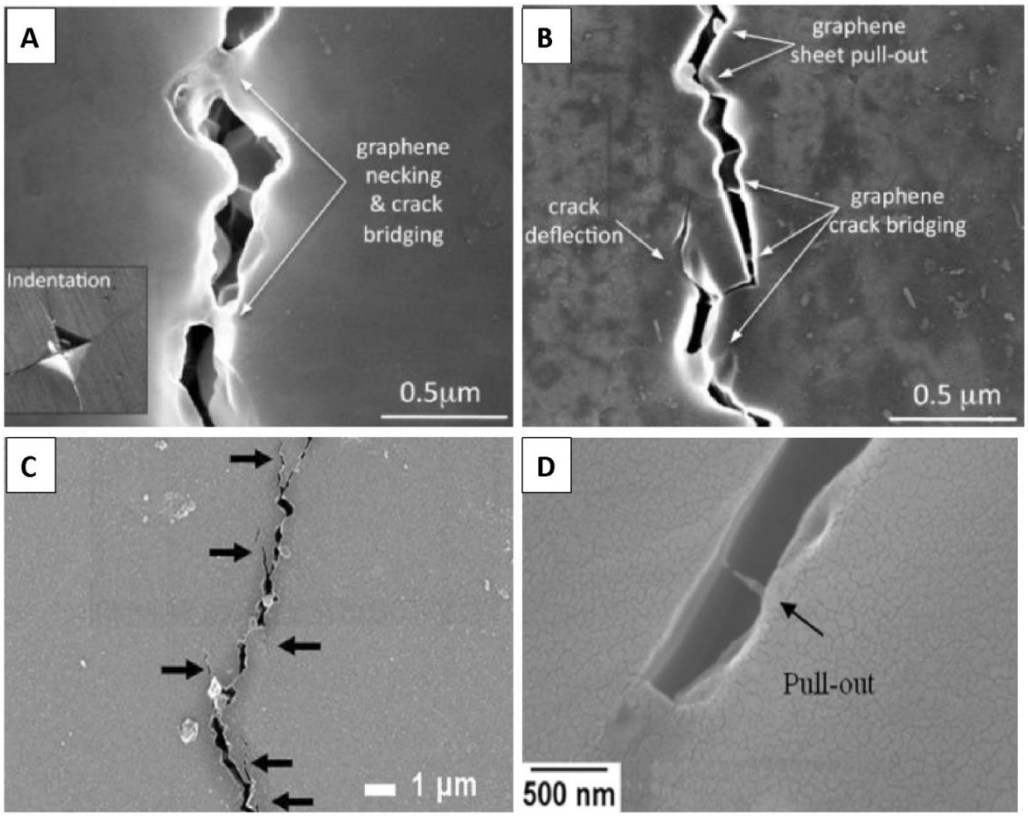

Figure 2.9 SEM images showing various mechanism of crack propagation **(a)** radical cracks (inset) crack bridging mechanism; **(b)** graphene pull out, crack deflection and crack bridging; **(c)** crack branching; and **(d)** graphene pull out mechanism of crack propagation. Adapted from references [27, 81, 82] respectively.

Wange et al. [38] used colloidal processing to produce well dispersed graphene-alumina composites. They reported a reinforcement of ~53% (SENB method) with a 2 wt% loading of graphene. They reported various toughening mechanism, including nano-sheet pull out and bridging. They observed that the addition of graphene in the alumina matrix resulted in grain size refinement. The grain size of pure alumina was 1000 nm, while the grain size of composites was 500

nm. This is similar to the effect of CNTs, Inam et al. [79, 101] reported inhibition of grain growth by CNTs in an alumina matrix.

Liu et al. [83] prepared graphene platelet reinforced zirconia toughened alumina (ZTA) nano composites using SPS. The fracture toughness of their material, measured by SENB method, resulted in an increment of ~40% for only 0.8 vol % loading of graphene. They also observed toughening mechanism such as pull-out, bridging and crack deflection on fractured surfaces with graphene trapped and anchored in between grain boundaries.

Kim et al. [89] reported improvements in fracture toughness, flexural strength and wear resistance of unoxidised graphene-alumina composites. In their work they compared the mechanical properties of unoxidised graphene composites with GO and reduced GO composites and found that best results were obtained for unoxidised graphene-alumina composites. The improvement in mechanical properties was related to less defect concentration in the case of unoxidised graphene flake. They reported an improvement of ~48% in fracture toughness, ~28% in flexural strength and ~95% in wear resistance of the composites. Crack bridging was considered as the main toughening mechanism. The amount of graphene loading (~0.5 vol%) required for achieving such reinforcement in mechanical properties (fracture toughness, flexural strength, wear resistance) of the alumina composites was much smaller when compared to CNTs (~1-10 vol%) and whiskers (>10 vol%) reinforcements. They also compared the effect of graphene size (~100, 20 and 10 μm) on the fracture toughness of graphene-alumina composites and found that best results were obtained for graphene flakes with lateral size of ~20 μm. Very big graphene flakes (~100 μm) produced structural defects in alumina nano-composites

while in the case of smaller flakes (~10 μm) the crack bridging toughening mechanism appeared to be less dominant.

In a fiber reinforced ceramic, the strength of the ceramic depends on the interface between the ceramic and fiber material. Once a crack is initiated and propagated, load is transferred from the ceramic matix to the fiber in the way of a crack. If the interface between the fiber and the ceramic is weak the fiber remains intact and the crack is deflected, and if the interface is too strong the crack penetrates through the fiber and the composite is brittle, just like a monolithic ceramic. Similar to fibre reinforced composites, a crack can propagate in three ways in graphene reinforced ceramic matrix composites i.e. singly deflected crack, doubly deflected crack and penetrating crack, **(Figure 2.10)**. However, the crack propagation behaviour can be different in graphene ceramic composites compared to fibre reinforced composites. In the case of strong bonding between graphene and the ceramic matrix, the high strength and increased contact area of graphene does not allow a crack to propagate through the graphene and in order for the crack to propagate it has to take more tortuous route, as shown in **Figure 2.10 f)**. Moreover, the force required to pull out a graphene sheet is expected to be higher than that required to pull out a nano-fiber because of its larger specific surface area and the wrapping/anchoring of graphene around ceramic grains. Also, the relatively large size of graphene flakes provides a lengthy deflection path. These properties contribute to the toughness of graphene ceramic composites and make graphene a good reinforcement [83]. It should be noted that the interface between graphene and ceramic plays an important role in deciding the mechanical properties of the GCMC. It may be more sensible to use graphene with carbides (eg. B_4C, SiC) and GO with

oxides (eg. Al_2O3 and ZrO_2) to obtain better interfacial bonding and to obtain better mechanical properties, although further research on this topic is needed.

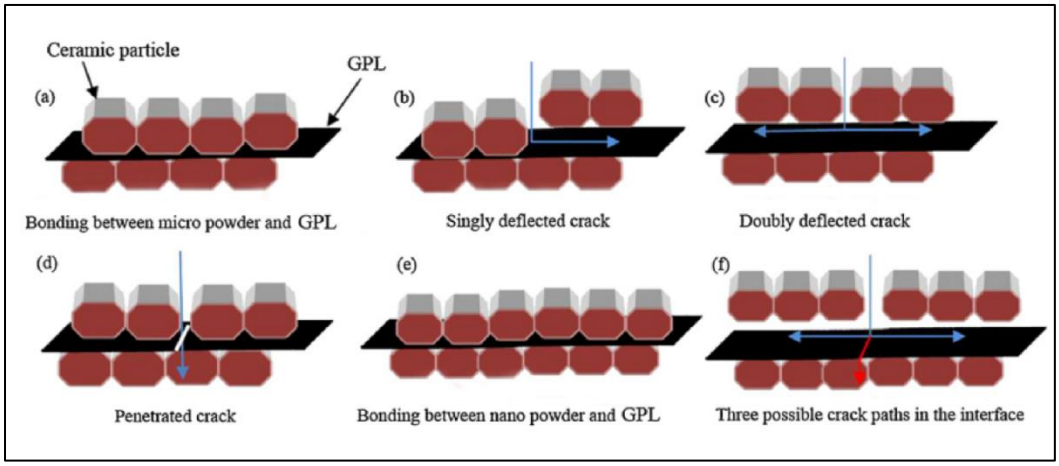

Figure 2.10 A schematic of toughening mechanism in composites with micro and nano scale ceramic matrix. Adapted from reference [82].

Ramirez et al. [102] explained the toughening in graphene nano platelet (GNP)/GO-silicon nitirde composites by using a well known model for reinforcement in ceramic composites by whiskers/fibers. In order to explain this they made a few assumptions: 1) GNP/GO platelets are aligned in a direction perpendicular to the pressing direction in SPS, this assumption is supported by many experimental observations [80]. 2) Graphene fillers in the ceramic matrix are in residual tension because of the mismatch in thermal expansion coefficient values of graphene fillers and silicon nitride. 3) Since nanofillers are in residual tension in the silicon nitride matrix contribution in fracture toughening due to GNP/GO pullout was not considered. Although they did not consider the contribution to toughening due to GNP/GO pullout in their model, their assumption is a bit contradictory to the

experimental evidence, as many authors have reported improvement in fracture toughness due to GNP/GO pullout [27].

The improvement in toughness due to the failure of the filler in the wake zone was calculated using **equation 2.2** [102] and compared to the experimental data for GNP/GO-silicon nitride composites.

$$\Delta G_c \equiv 2f \int_0^{t=S} tdu + \frac{4f\Gamma_i d}{(1-f)R} = \frac{fS^2 R[(\lambda_1+\lambda_2 (d/R))^2 - (E_F e_T/S)^2(\lambda_3+\lambda_4(d/R))^2]}{Ef(\lambda_1+\lambda_2(d/R))} + \frac{4f\Gamma_i d}{(1-f)R} \quad \textbf{(2.2)}$$

where, f is the filler volume fraction, S is the strength of the filler, R is the filler radius, E_F is the fiber elastic modulus, e_T is the misfit strain and Γ_i is the interface fracture energy. The λ_i coefficients depend on the filler volume fraction and the ratio between the fiber and matrix elastic modulus. The first term in **equation 2.2** is related to toughening due to crack bridging while the second term is associated with debond surface energy. The experimental toughness data was converted to critical strain energy release rate (G_c) using the expression $G_I = K_I^2/E'$ ($E' = E/1\text{-}v^2$) and compared to data plotted using **equation 2.2**. The best fittings for the experimental data were obtained by using strength (S) values for GNP and reduced GO of 20 and 40 GPa repectively which seems contradictory because strength of GNP should be higher than GO since GO were damaged during oxidation. Authors found a good corelation between experimental and theoretical data for GNP composites, where as some divergence in data was observed for reduced GO composites with filler loading >4 vol%. In the case of GNP composites, the

divergence in the data was observed at 7 vol% loading. For high graphene loading because of the overlapping of the interface crack propagation happens through the overlaping interfaces of graphene fillers and hence crack bridging becomes a less dominant toughening mechanism leading to a discrepency in the theoretical and expermental data for high GNP loading. They explained crack bridging to be the the main dominant toughening mechanism in the case of GNP/GO-silicon nitride composites. For high loading of graphene nano-fillers, the crack briding model becomes invalid because of the formation of a three dimensional inter connected network of GNP which controls the failure of the composites.

2.5.1 Tribological Properties

The tribological properties of ceramics are very important for a variety of engineering applications. Although the majority of the work on graphene-ceramic composites has reported improvement in mechanical properties (fracture toughness, strength, hardness, elastic modulus), some authors have also investigated the friction and wear properties of the graphene-ceramic composites. Since, carbon is considered a very good lubricant, the tribological properties of graphene-ceramic composites are expected to be better compared to pure ceramics. Authors have mainly used ball on disc appratus to study the tribological properties (friction and wear rate) of graphene-ceramic composites. The wear rate (W) is usually calculated using **equation 2.3** while coefficient of friction is recorded during the experiment

$$W = V/ L. F_p \ (mm^3/mN) \qquad \textbf{(2.3)}$$

where, W is the specific wear rate, V is the worn volume, L is the sliding distance and Fp is the loading force during the experiment.

Hvizdos et al. [103] measured the tribological properties of graphene nano platelet-silicon nitiride composites (1 and 3 wt%) composites using the ball on disk method with silicon nitride ball as the counter part for a sliding distance of 300 m. They studied the effect of four different kinds of GNP on the tribological properties of GNP-silicon nitride composites. No significant change in coefficient of friction was observed for all the composites suggesting graphene was nicely embedded in the silicon nitride matrix and did not take part in the lubrication process. In the case of the wear resistance, no significant change was observed for 1wt% GNP-silicon nitride composites while there was an improvement of 60% for composites with 3 wt% GNP loading. Also when comparing different kinds of GNP they found larger size GNP showed better wear properties. They also compared the GNP-silicon nitride composites to CNTs-silicon nitride composites and found GNP composites were more wear resistant compared to CNT composites for the same nano-filler loading. The improvement in wear properties was related to the improvement in mechanical properties of the nano-composites with GNP addition. The group also extended their work on GNP-silicon nitirde composites to understand the tribological properties at high temperatures (300, 500 and 700 ^{o}C) [104]. They found for 3 wt% GNP-silicon nitride composite both the coefficient of friction and wear rate increased with increasing temperature. In the case of pure silicon nitride and 1 wt% GNP composites, the coefficient of friction and wear rate first decreases at 300 and 500 ^{o}C and then increases again at 700 ^{o}C. The decrease in wear rate at 300 and 500 ^{o}C was associated with the formation of an oxide layer in silicon nitride composites. The final wear rate at 700 ^{o}C was high for all of the composites and improvement in

wear properties was observed at room temperature only for GNP-silicon nitride composites.

In another study on silicon nitride matrix composites, Belmonte et al. [105] used ball on disc method and different loads (50, 100 and 200 N) to understand the tribological properties of GNP (3 wt%)-silicon nitride composites. They found that coefficient of friction was higher for the nano-composites at lower loads and decreased with increasing loads. The coefficient of friction of GNP-silicon ntirde composite was 11% lower than pure silicon nitride for a 200 N load, while wear of the material was lower in the case of GNP composites. Similar to coefficient of friction, the difference between the wear properties was more marked for composites tested at higher loads. There was an overall decrease of 56% in the wear rate of GNP-silicon nitride composites tested at 200 N loads. They also found that wear of counter part material decreased when tested against nano-composites, suggesting increase in lifetime of counter part materials.

Li et al. [106] prepared GNP reinforced zirconia coatings and investigated the tribological properties of the composite coatings with ball on disc method for different loads (10, 50 and 100 N). They also prepared pure zirconia and zirconia-graphite coatings for comparison. Similar to Belomonte et al., they observed that both the coefficient of friction and wear rate of the GNP composite films decreased with increasing load. The best results for tribological properties were obtained for GNP-zirconia films compared to pure zirconia and graphite-zirconia films for all loadings. They reported a reduction of 29% in the coefficient of friction and 50% in the wear rate of GNP-zirconia compared to pure zirconia coatings.

2.6 Functional Properties and Percolation Threshold

Because of the remarkable in plane electrical (10^7 S m^{-1}) [36] and thermal (5300 W mK^{-1}) [14] conductivities of graphene, some researchers have investigated the functional properties of GCMCs. **Table 2.2** summarizes the electrical and thermal properties of GCMC reported in the literature so far.

Table 2.2 Overview of the functional properties of Graphene-ceramic composites as reported in literature.

Matrix material	**Nano-filler Type**	**Nano-filler content**	**Processing routes/ Consolidation Method**	**Temperature Measurement**	**Investigated properties (%) shows increase in properties compared to unloaded ceramics**
Al_2O_3 [15]	Milled graphene platelet	0-15 vol%	Powder/SPS	Room Temp. 2-300 K for 3.5 and 4 vol%	Percolation Threshold: 3 vol%. Electrical conductivity: 5709 S m^{-1} for 15 vol%.
Al_2O_3 [38]	Reduced GO	2 wt%	Colloidal/SPS	Room Temp.	Electrical conductivity: 172 S m^{-1}, 13 orders magnitude higher than Pure alumina.
Al_2O_3 [107]	Reduced GO	0- 2.35 vol%	Colloidal/SPS	Room Temp.	Percolation Threshold: 0.38 vol%. Electrical conductivity: 1000 S m^{-1} for 2.35 vol%.
Si_3N_4 [108]	GNP	12 and 15 wt%	Powder + Colloidal /SPS	Room Temp.	Percolation Threshold > 4.4 vol%.
Si_3N_4 [109]	GNP	4-25 vol%	Powder + Colloidal /SPS	Room Temp.	Percolation Threshold: 7-9 vol%. Electrical Conductivity: 40 S m^{-1}.
Al_2O_3 [80]	Reduced	0- 0.45	Colloidal/SPS	Room Temp	Percolation Threshold:

	GO	wt%			0.22 wt%. Electrical Resistivity: 9 and 81 Ω.cm (perpendicular and parallel to pressing direction in SPS respectively) 8 orders of magnitude lower than pure alumina
SiC [110]	In-situ Few Layer Graphene	4 vol%	Powder/SPS	Room Temp.	Electrical Conductivity: 102 S m^{-1}.
Si_3N_4 [111]	Reduced GO	7 vol%	Powder/SPS	Room Temp.	Electrical Conductivity: 7 S m^{-1}. 13 orders of magnitude higher than pure silicon nitride.
ZrO_2 [112]	Reduced GO	4.1 vol%	Colloidal/SPS	Room Temp.	Percolation Threshold: 2.5 vol%. Electrical Conductivity: 1.2 X 10^4 S m^{-1}. >14 orders of magnitude higher than pure zirconia. Thermal Diffusivity: 1.1 mm^2/s (12%).
Si_3N_4 [113]	GNP	4.3-24.4 vol%	Powder/SPS	Room Temp. 320-1073 K for through-thickness direction	Thermal Conductivity: 40 W mK^{-1} (100%).
Si_3N_4 [114]	GNP	10 wt%	Powder/HIP	Room Temp.	Thermal Conductivity: Perpendicular to pressing direction 60 W mK^{-1} (200%). Parallel to pressing direction 21 W mK^{-1} (-21%).

According to percolation theory, the macroscopic properties of a material (such as electrical conductivity) changes with nano-filler loading at a critical percolation threshold due to the formation of a continuous network structure. This change in property can be related to the change in concentration of nano-filler by the following scaling law:

$$\sigma_c = \sigma_o (\phi - \phi_c)^t \quad \text{for } \phi > \phi_c \qquad (2.4)$$

where, σ_c and σ_o are the conductivity of the composite material and conducting component (nano-filler), respectively. ϕ is the volume fraction of graphene and ϕ_c is the critical volume fraction or percolation threshold and t is the fitting constant which represents the dimensionality of the system.

The percolation threshold for GCMC was studied for the first time by Fan et al. [15], in which they prepared composites with 0-15 vol% graphene loading in an Al_2O_3 matrix. The percolation threshold for the composites was around 3 vol%. The electrical conductivity of the composites increased with increasing amount of graphene as shown in **Figure 2.11**, and reached a value of 5709 S m^{-1} for 15 vol%. This is 170% higher than the previously best reported result for alumina-CNTs composites [11]. They also studied the temperature dependence of electrical conductivity in the temperature range of 2-300 K and found that the composites behaved as semi-metals.

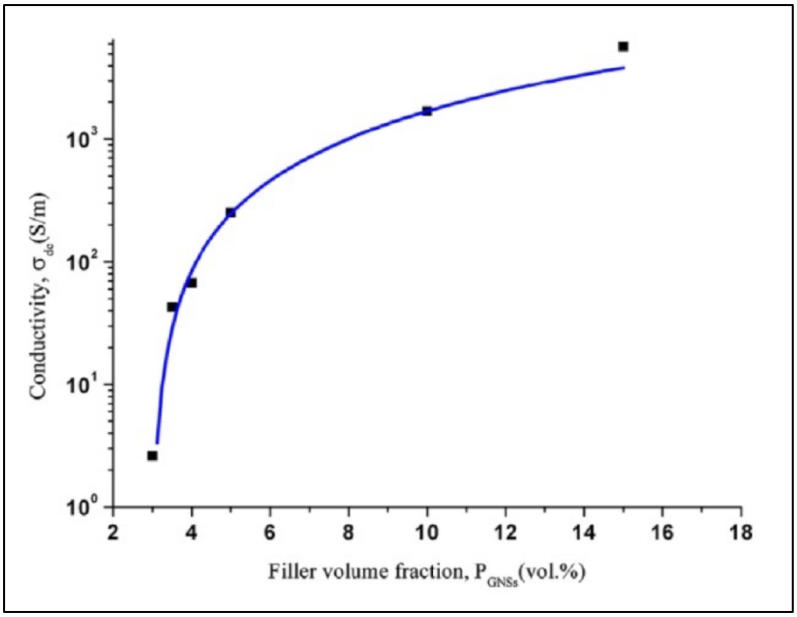

Figure 2.11 Change in electrical conductivity of graphene-alumina composites with increasing conc. of graphene with threshold value at 3 vol%. Adapted from reference [15].

In a more recent work by Fan et al. [107] they used colloidal processing to prepare well dispersed GO and alumina composite powders. GO was reduced to graphene thermally during SPS processing. They reported a threshold value of 0.38 vol%, which is much lower than their previously reported value of 3 vol%. It is also lower than the best reported value of 0.64 vol% for CNTs-$MgAl_2O_4$ [75] composites. This improvement was attributed to good dispersion and the high quality of the graphene used, but their method for measuring graphene volume content in the alumina matrix is not well established. In order to measure the net graphene volume after sintering of the composites, they loaded a certain amount of GO in a graphite die and processed it in SPS under the same conditions used for the graphene-alumina composites. They found that only 35% of the amount of GO was left after sintering

in SPS and therefore used this calculation to estimate the net graphene content in the graphene-alumina composites. They reported an electrical conductivity of 1000 S m^{-1} for only 2.35 vol% loading of graphene. More interestingly, they reported that the Hall coefficient reversed it sign from positive to negative with increasing concentration of graphene, revealing a change in the major charge carrier. They also confirmed this effect by thermo power measurements, where the value of Seebeck coefficient changed from positive to negative. The intrinsic charge carrier type for a graphene film should be electrons as chemically reduced and annealed GO films have semi-metallic characteristics. The reason for the positive Hall coefficient was considered to be due to doping of the graphene by the alumina matrix. It has been reported that the substrate can influence the properties of graphene. In the case of graphene-alumina composites, due to mismatch in coefficient of thermal expansion, graphene expands during cooling while alumina contracts. It was suggested that this generates high pressure and very firm contact between alumina and graphene. Also, in an environment of low oxygen partial pressure at high temperature, oxygen vacancies and aluminium interstitials are promoted as the main point defects. These positively charged defects act as electron acceptor and make graphene hole doped. They explain the positive value of hall coefficient due to this doping affect. This changed to negative value when the concentration and thickness of the graphene increased. This phenomenon is very unique and has not been reported for other composites. In some other work with an alumina matrix, Wang et al. [38] reported a conductivity of 172 S m^{-1} for a 2 wt% loading of graphene.

Ramirez et al. [108] used conductive scanning force microscopy to investigate the electrical conductivities of 12 and 15 wt% graphene nano platelets-silicon nitride composites above their percolation threshold. As confirmed by current

maps obtained for parallel and perpendicular orientation, they reported the preferential orientation of graphene platelets in the ceramic matrix of materials prepared by SPS. In other recent research by the same group, also with a silicon nitride matrix [109], they prepared composites with a loading of up to 20 vol%, and reported an electrical conductivity of 40 S m^{-1}. They confirmed the preferred orientation of the graphene platelets in silicon nitride matrix from electrical conductivity measurements. In the direction perpendicular to the SPS pressing axis the electrical conductivity was one order of magnitude higher than in the parallel direction. They reported a percolation threshold of 7-9 vol% depending on the conductivity measuring direction. Also, different mechanisms of charge transport were reported for the different directions. The variable range hopping mechanism for charge transport was dominant in the perpendicular direction; while in the parallel direction it was attributed to a complex behaviour with a metallic type transition.

Inam et al. [115] used the change in the electrical conductivity values of the alumina nano-composites prepared using various carbon nano-fillers (CNTs, GNP and Carbon black) to quantify the damage to alumina matrix with indentation. They found that the electrical conductivity of alumina-CNTs composites showed a decrease in 86% after indentation compared to 69% and 27% decrease in electrical conductivity values in the case of GNP and carbon black respectively. Although GNP showed reasonable sensitivity, CNTs were more sensitive to material damage because of their fibrous nature and high electrical conductivity. This novel approach can be used for damage sensing applications. In another work by the same group they analysed the thermal stability of GNP (3 vol%)-alumina nano-composites [116]. They prepared composites using SPS and HIP with different dwell times (10-60 minutes) and compared their electrical conductivities. They found that for longer

dwell times (60 minutes) the electrical conductivity values were higher compared to composites sintered using short dwell times (10-20 minutes) for both SPS and HIP. The increase in electrical conductivity was attributed to increased graphitisation at high temperatures for longer dwell times which was lacking in composites prepared using short dwell times.

Research on thermal conductivity of GCMC was carried by Miranzo et al. [113], in which they compared the thermal conductivities of CNTs and graphene platelets reinforced silicon nitride composites. They prepared composites ranging from 0.9 to 8.6 vol% for CNTs and 4.3 to 24.4 vol% for graphene platelets. They reported that the addition of both carbon nanostructures leads to anisotropic thermal response, decreasing the through thickness thermal conductivity of silicon nitride composites and increasing the in plane conductivity. In the case of graphene platelets composites, the thermal conductivity in the in plane direction increased twice as compared to the pure silicon nitride matrix. This effect was attributed to the preferential orientation of graphene platelets after SPS in the ceramic matrix leading to a more conductive network in the in plane direction of thermal conductivity. Similar anisotropy in thermal conductivity of GNP-silicon nitride composites was reported by Rutkowski et al. [114].

It should be noted the functional properties of the GCMC depend not only on the quality of graphene dispersion in the ceramic matrix but also on the surface functionalization. GO or reduced graphene is reported to have poor electrical and thermal properties as compared to pure graphene due to defects induced during functionalization [34, 117]. Similarly the oxidation and degradation of graphene during high temperature processing can also affect the properties of GCMC as

reported in case of CNTs [70]. A detailed study is needed to understand these topics and may be of interest to other researchers for future work.

2.7 Bioactivity

The main problem associated with bio-materials (Calcium silicate (CS), Hydroxyapatite (HA), Bioglass) is they have poor mechanical properties which limits their applications in bio-medical fields [118]. Authors have used second phase reinforcements (ceramics, polymers, metals) to improve the mechanical properties of bio-materials but these second phase fillers do not show enough bio-compatibility to be used for bio-medical applications [119-121]. Recently it has been shown by Conroy et al. [122] that graphene films produced by CVD and Liquid phase exfoliation method are bio compatible. They reported no detectable change in cell morphology or attachment of cells during the bio-compatibility testing of graphene films for a 72 hour incubation period. Since graphene has very good mechanical, electrical and thermal properties along with biocompatibility, authors have used graphene as a second phase nano-filler to improve simultaneously the mechanical and biological properties of graphene-bio material composites.

Mehrali et al. [91] produced reduced GO-CS composites with various loading of reduced GO (0.25, 0.5, 0.75, 1 and 1.5 wt%) and reported an improvement in mechanical properties of CS nano-composites **(Table 2.1)**. Other than improving the mechanical properties, the addition of reduced GO resulted in the improvement of bioactivity of CS composites compared to pure CS. They reported a thicker HA layer formation on the surface of nano-composites compared to pure CS after Simulated Body Fluid (SBF) test. Also the introduction of reduced GO into the CS matrix

stimulated the human osteoblast cells proliferation and significantly increased the alkaline phosphate activity of human osteoblast cells compared with pure CS ceramics. Similarly improvement in bioactivity of chitosan, silica and HA with incorporation of graphene or reduced GO has been reported by other authors [92, 123, 124].

Interestingly not all authors reported an improvement in bioactivity of graphene-bio-material composites. Zhu et al. compared the bioactivity of graphene nanosheet-HA and MWCNTs-HA composites. They reported a decrease in osteoblast cell adhesion and proliferation in the case of graphene nanosheet-HA composites compared to pure HA. On the other hand, the addition of MWCNTs to HA increased the bioactivity of HA composites. They suggested the dimensions and morphology of graphene to be the main reasons for reduced bioactivity in graphene nanosheet-HA composites, resulting in reduced osteoblast adhesion and proliferation on graphene surface of several micrometres.

2.8 Future work and Conclusion

This review presents the current state of knowledge of the synthesis of graphene and the processing and properties of GCMCs. It is clear that graphene has considerable potential as filler for ceramic matrices. This is confirmed by significant improvement in mechanical, tribological, electrical, thermal and biological properties reported in a number of publications.

Various mechanism of structural reinforcement has been identified in GCMCs. They can be differentiated from the ones occurring in CMCs containing CNTs. Uniaxial-pressure assisted sintering such as SPS results in a preferential alignment of

graphene in the ceramic matrix, leading to highly anisotropic properties. The orientation of nano-filler in composites prepared using SPS has not been reported for CNT-ceramic composites. The reported work shows that thinner graphene flakes improves various properties of GCMCs.

Work on graphene ceramic composites is in its early stages and there is still considerable work that needs to be done in order to optimise their processing, microstructure and interfacial properties. There is great potential to produce multifunctional materials with a completely new window of thermo physical properties for a wide range of applications.

Present research provides a comprehensive investigation in understanding the effect of the addition of graphene nano-platelets (GNP) on the mechanical, tribological and biological properties of glass/ceramic composites. We investigated two kinds of materials namely amorphous matrices like glasses (silica, bioglass) and polycrystalline matrices like ceramics (alumina). The idea was to understand the effect of GNP on these matrices as GNP was expected to behave differently in these composites. Bioglass (BG) was also chosen as a matrix material to prepare BG-GNP composites. GNP can improve the electrical conductivity of BG which can be used further for bone tissue engineering applications. The effect of GNP on both electrical conductivity and bio-activity of BG-GNP composites was investigated in detail.

Chapter 3 Experimental Details

3.1 Materials Used

This section provided the details about the materials used in this study.

3.1.1 Graphene

Graphene was synthesized using a liquid phase exfoliation method from graphite flakes, natural, 10 mesh (Alfa Aesar, Purity 99.9%, Size 1mm, MP > 2660 ^{o}C, **Figure 3.1 (a)**). The whole process was carried out in 2 cycles because of oxidative degradation of n-methyl pyrrolidone (NMP) after the 1st cycle of sonication [125]. Briefly, 10 g of graphite was mixed with 100 ml of NMP (Sigma-Aldrich). The sample was sonicated (CV33 flat probe sonic tip, 50 W, 25 KHz) for 10 hours in an ice bath and filtered using vacuum filtration. In the 2nd cycle filtered graphite was washed twice with fresh NMP and again re-dispersed in 100 ml of fresh NMP. The prepared suspension was sonicated for 10 hours using the sonic tip in an ice bath. After the 2nd cycle of sonication, the sample was filtered using vacuum filtration. The prepared graphene was washed twice with DMF (Sigma-Aldrich) to remove the traces of NMP.

The prepared graphene was then re-dispersed (Branson-5510 sonic bath) in fresh DMF. To remove the un-exfoliated graphite, the suspension was centrifuged (Centurion Scientific) at 500 rpm for 45 minutes. The top 80% of the supernatant was separated by pipet after centrifugation [40, 41]. The produced suspension was

very stable with a yield of 4 to 8 wt% and showed very small sedimentation after a period of 90 days.

Figure 3.2 shows the typical setup used for preparing graphene suspensions. **Figure 3.2 a)** image shows ultrasonic probe. Ultrasonication was done at amplitude of 25% with 5 second on and 1 sec off pulsing. **Figure 3.2 b)** Vacuum filtration setup used and **Figure 3.2 c)** centrifugation machine used. The centrifugation machine was used at 500 rpm speed for 45 minutes.

It should be noted that NMP was used as a solvent for the exfoliation process because of its higher boiling point ~200 ^{o}C which enabled the sonication process to be carried out at higher energies and resulting temperatures without deteriorating the solvent, while DMF [44] was used for processing of the powders because of its lower boiling point ~80 ^{o}C, thus enabling easy drying. The prepared graphene flakes were characterised using UV, Raman spectroscopy and Transmission electron microscopy as described in detail in the sections below. **Figure 3.1 b)** shows the TEM image of graphene produced from graphite flakes using liquid phase exfoliation. The average length of the flakes was ~1.5 µm and average thickness was 4-5 layers.

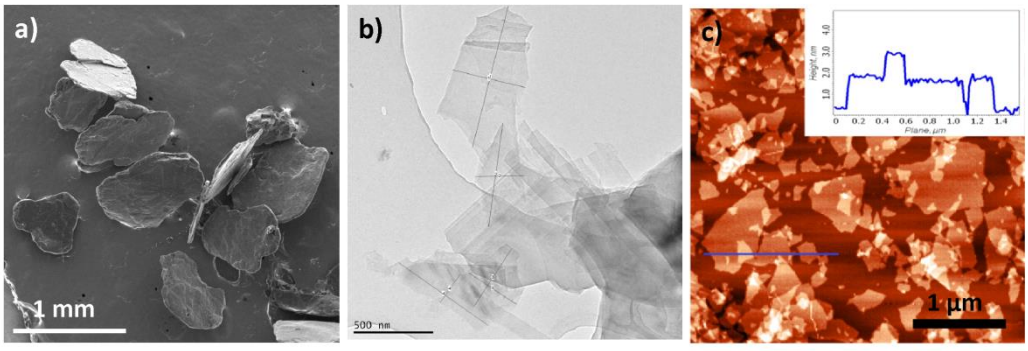

Figure 3.1 a) SEM image showing as received graphite flakes (Alfa Aesar); b) TEM image showing graphene produced using liquid phase exfoliation and; c) AFM image showing GO flakes with average length of 1-2 µm and thickness of 2-3 nm.

Figure 3.2 shows: a) the ultrasonic probe; b) vacuum filtration setup and; c) centrifugation machine.

3.1.2 Graphene oxide

The graphene oxide (GO) used in the present work was purchased commercially from Nano-innova. The data sheet provided by the company shows the characterisation of the GO flakes using FTIR, XRD, XPS, AFM and solid state NMR spectroscopy. The average length of GO flakes was 1-2 µm and thickness was 2-3 nm **(Figure 3.1 (c))**. SEM analysis after dispersion of the GO flakes in a glass matrix suggests that the GO flakes thickness was 20-50 nm. To prepare GO suspension, GO powder was dispersed in ethanol using an ultrasonic bath for 2 hours. The zeta potential (Malvern Instrument-Nano ZS) values of the prepared suspensions were measured to be -5.36 mV. GO was also characterised using XRD and Raman spectroscopy.

It should be noted that after processing both graphene and graphene oxide flakes were found to be thicker compared to graphene and graphene oxide flakes before processing so from here on they will be referred as graphene nano platelets (GNP) and graphene oxide nano platelets (GONP).

3.1.3 Silica

Silica was used as the glass matrix in the present study. Commercially available nano silica powder was purchased from Sigma Aldrich with particle size of 10-20 nm, density of 2.2 g/cm^3, boiling and melting points 2230 and 1600 ^{o}C respectively.

3.1.4 Alumina

Alumina used in the present work was purchased commercially from Sumitomo Chemicals sold with commercial name AKP-53. It has a particle size of 200 nm, specific surface area of 12.3 m^2/g and density of 3.98 g/cm^3. The main phase of the alumina used was α. **Figure 3.3** shows **a)** the properties and **b)** TEM image showing the particle size of commercial alumina powder used.

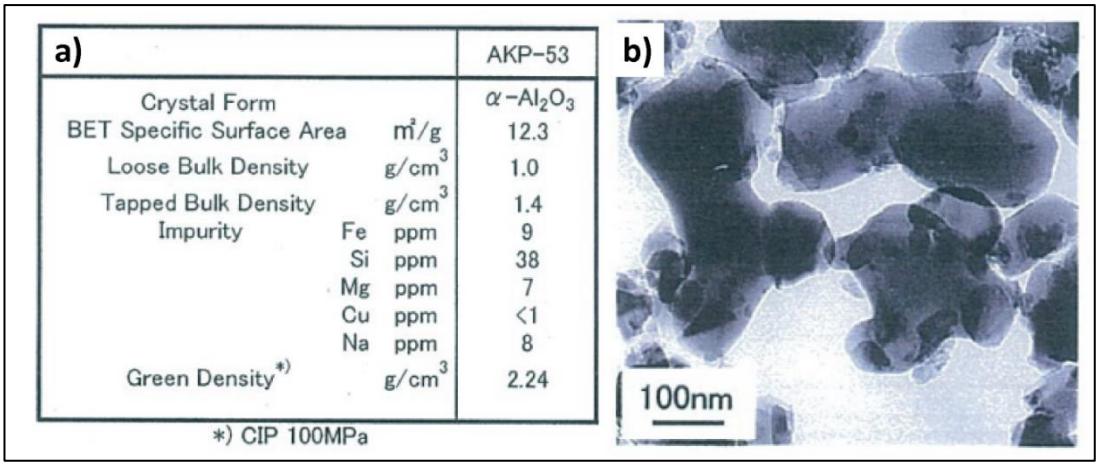

a)

			AKP-53
Crystal Form			α-Al_2O_3
BET Specific Surface Area		m^2/g	12.3
Loose Bulk Density		g/cm^3	1.0
Tapped Bulk Density		g/cm^3	1.4
Impurity	Fe	ppm	9
	Si	ppm	38
	Mg	ppm	7
	Cu	ppm	<1
	Na	ppm	8
Green Density*)		g/cm^3	2.24

*) CIP 100MPa

Figure 3.3 a) Properties and; **b)** TEM image showing particle size of the alumina powder as provided by Sumitomo Chemicals.

3.1.5 Bioglass

Bioglass (BG) powder used in the present work is a commercially available product, Bioglass 45S5®. The BG powders were provided to us by our collaborator Prof. Aldo R. Boccaccini from Institute of Biomaterials, Erlangen, Germany. The chemical composition of the BG powders was 45 wt.% SiO_2 , 24.5 wt.% Na_2O, 24.5 wt.%, CaO and 6 wt.% P_2O [126, 127]. The BG particles were very coarse with an average particle size ranging from 60-80 µm and density of 2.72 g/cm^3. **Figure 3.4** shows the SEM image of as received BG particles.

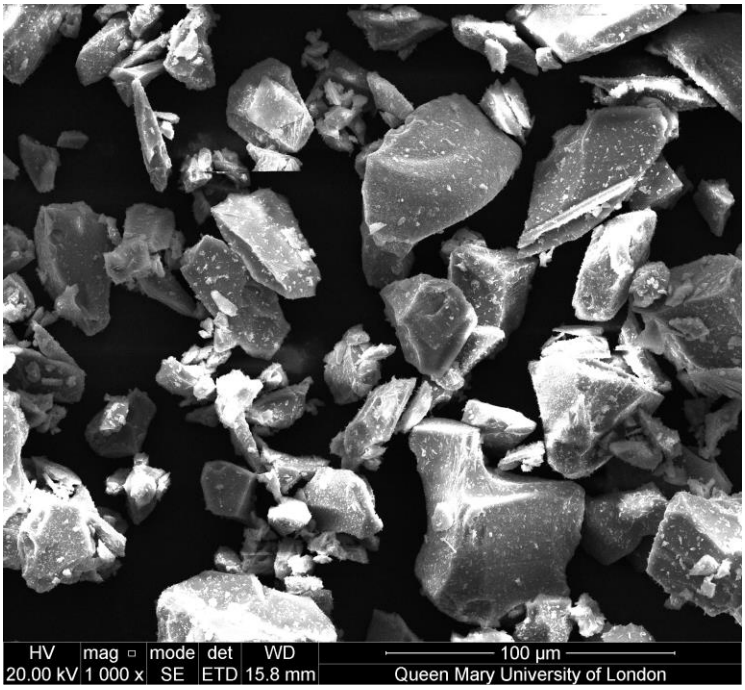

Figure 3.4 SEM image of bioglass powder.

3.2 Processing

We tried various processing methods to obtain good dispersion of the graphene and GO in the glass/ceramic composites. Since different glass/ceramic matrices were used, processing was optimised for each material. Mainly powder and colloidal processing methods were used to prepare GNP/GONP-glass/ceramic composites. The details about the processing are described in sections below.

3.2.1 Powder processing

Powder processing was used to prepare composites with all kinds of matrices used in this study namely alumina, silica and BG. In order to prepare uniform and well dispersed nano-composites using powder processing route. The already

prepared graphene suspension were diluted to the desired concentration of 1 mg/ml using DMF as the solvent, and then sonicated for 2 hours in an ultra-sonic bath. After sonication, commercially available α-Al_2O_3 powder, silica powder or BG powder was added to the prepared suspension, and the slurry was ball milled at 350 rpm using QM planetary ball mill (Nanjing University Instrument Plant) and zirconia balls (diameter 10 and 5 mm) for 4 hours with a powder-to-ball weight ratio of 1:20. After milling the prepared slurry was dried on a hot plate at 90 ^{o}C for 10 hours. The dried mixture was ground and sieved using 250 mesh followed by drying in a vacuum oven at 90 ^{o}C for another 2 days. **Figure 3.5** shows the images of the **a)** nylon ball milling jars and **b)** planetary ball milling machine used for powder processing of the nano-composite powders. It should be noted that the pure alumina, silica and BG sample were also fabricated using the same processing route for comparison of the properties of the nano-composites against pure samples. It should be noted that only powder processing was used to fabricate alumina-GNP composites while both powder and colloidal processing were used to fabricate silica-GONP/GNP and BG-GNP composites.

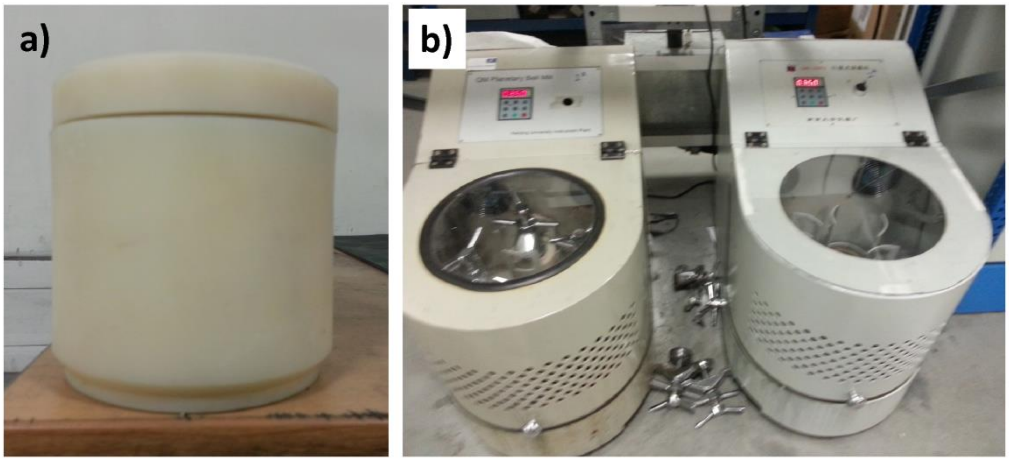

Figure 3.5 images showing: **a)** Nylon ball milling jar and; **b)** Planetary ball milling machine used for powder processing.

3.2.2 Colloidal processing

Colloidal processing was used to optimise the processing conditions for preparing both silica-GNP/GONP and BG-GNP composites using various solvents. Details about the processing method are described below separately for both silica and BG matrix composite powders.

3.2.2.1 Silica-GNP/GONP

In order to prepare silica-GNP and silica-GONP composite powders using colloidal processing, suspensions of GNP, GONP and silica were prepared separately. First, GNP/DMF [44] and GONP/ethanol suspensions were sonicated for 4 hours in order to obtain good dispersion and exfoliation of GNP and GONP powders in the solvents. The concentrations of the suspensions were 1 mg/ml. Similarly silica/DMF and silica/ethanol suspensions with concentrations 30 mg/ml were prepared by sonication for 2 hours. Already prepared GNP and GONP suspensions were added drop wise to the silica suspensions with magnetic stirring (200 rpm). After 2 hours of magnetic stirring, suspensions were dried on a hot plate at 80 ^{o}C for 12 hours. Similar to the powder processing method, the dried mixtures were ground and sieved using 250 mesh followed by drying in vacuum oven at 80 ^{o}C for another 2 days.

3.2.2.2 BG-GNP

Two different solvents were used to prepare BG-GNP powder mixtures using colloidal processing route. In the first case, separate BG and GNP suspensions were prepared by adding separately powders of BG and GNP into a mixture of acetone

and DI water (3:1) [128], followed by ultrasonication for 2 hours. In the second case, separate BG and GNP suspensions were prepared using DI water as the solvent followed by 2 hour sonication. As GNP is hydrophobic in nature, cationic surfactant Cetyl trimethylammonium bromide (Ctab, Sigma Aldrich) was added before the ultrasonication step to obtain good dispersion of GNP in DI water. The surfactant to GNP weight ratio was 1:5. In both cases after sonication the GNP suspensions were slowly added drop wise to the BG suspensions while magnetic stirring (200 rpm). The concentrations of BG and GNP suspensions were 30 and 1 mg/ml respectively. After 2 hours of magnetic stirring, the suspensions were dried on a hotplate at 80 ^{o}C for 12 hours followed by grinding and sieving using 250 mesh and drying in a vacuum oven at 80 ^{o}C for another 2 days.

3.3 Sintering

Spark plasma sintering uses pulsed DC electric currents to achieve very high heating rates (600 ^{o}C/min) while applying uniaxial pressures (upto 75 MPa this work) [77]. High heating rates combined with high pressure can be used to decrease both sintering times and temperatures for sintering nano-composites. As discussed in the **chapter 2,** decreasing the sintering times and temperatures is very important to maintain the structural integrity of carbon nano-materials during high temperature processing. Another advantage of using SPS is the alignment of graphene flakes in the glass/ceramic matrix in a direction perpendicular to applied pressure. This can be useful for preparing nano-composites with anisotropic properties. **Figure 3.6** shows a typical SPS setup with inset showing the cross section view of the carbon die set.

Bulk samples were prepared after sintering of nano-composite powders using an SPS furnace (HPD 25/1, FCT systems, Germany, Furnace). Different materials were sintered at different temperatures, details about the sintering procedure for each material are provided in the sections below. It should be noted that the powders were held at 450 (silica, alumina) and 300 ^{o}C (BG) for 5 to 10 minutes during heating in the SPS furnace in order to remove any traces of solvent left after the processing. The samples prepared were 20 mm in diameter and 4 mm in thickness for silica and alumina composites and 10 mm in diameter and 4 mm in thickness for BG composites.

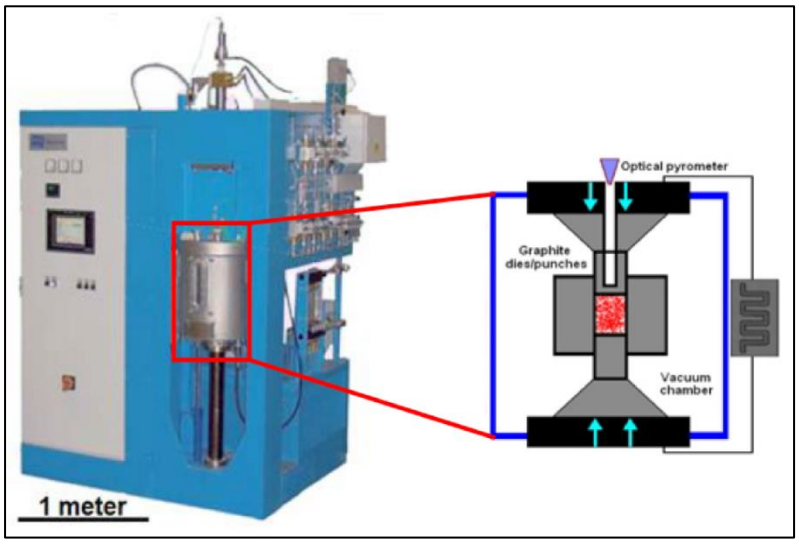

Figure 3.6 Spark Plasma Sintering Furnace, inset showing the cross sectional view of the carbon die set.

3.3.1 Silica-GNP/GONP composites

The silica-GNP and silica-GONP composites were densified using an SPS furnace at 1200 ^{o}C (heating, cooling rate 100 and 50 ^{o}C/min respectively) with

simultaneous application of 50 MPa pressure for a dwell time of 7 minutes. The pressure was raised during heating (1100-1200 ^{o}C) from 12 to 50 MPa, and then linearly decreased in 6 minutes at 1200 ^{o}C.

3.3.2 Alumina-GNP composites

Al_2O_3-graphene nano composites with different vol% loading were sintered using a SPS furnace at 1350 ^{o}C (heating and cooling rate 100 ^{o}C/min) with simultaneous application of 50 MPa pressure for a dwell time of 5 minutes. The pressure was removed at the end of the sintering.

3.3.3 BG-GNP composites

BG-GNP composite powders were densified using an SPS furnace at 600 ^{o}C with a 2 minutes dwell time and 70 MPa pressure [127]. The pressure was applied from the start and maintained constant throughout the sintering process while the temperature was increased at a rate of 50 ^{o}C/min up to 550 ^{o}C. Just before the holding temperature, the heating rate was reduced to 10 °C/min to avoid overheating and consequent crystallization of the glass. The samples were 10 mm diameter and 3 mm thick.

3.4 Characterisation

3.4.1 UV spectroscopy

The concentration of prepared GNP suspensions was measured using UV-Visible spectroscopy (Perkin Elmer-Lambda 950) by recording the absorbance at 660 nm

and calculating the concentration using Beer-Lambert's law **(equation 3.1)**, where *A* is the absorbance, *l* is the path length (10^{-2} m) and α is the extinction coefficient with a value of 3620 ml/mg/m [40] and *C* is the concentration of the suspension. The concentration of the prepared suspension ranged from 2.5 to 5 mg/ml. **Figure 3.7** shows UV spectrums of GNP suspensions produced using liquid phase exfoliation method. The red and black lines in the figure indicate GNP suspensions with different concentrations. Absorbance of GNP suspensions is directly related to the concentration. This can be used to calculate the concentration of GNP suspensions using Beer lamberts Law **(equation 3.1)**.

$$A/l = \alpha C \qquad \textbf{(3.1)}$$

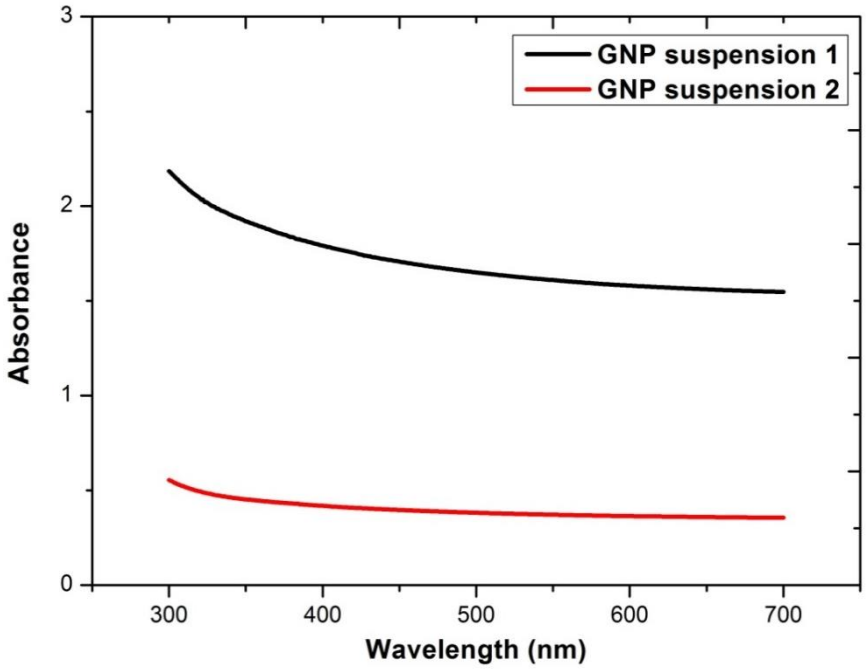

Figure 3.7 UV spectrums of GNP suspensions with black line showing GNP suspension with higher concentration.

3.4.2 Polishing and Density Measurements

The sintered samples were ground and polished using SiC paper down to 4000 grit and then diamond suspensions before characterisations. The surface roughness of polished samples was around ~1 μm. The bulk density of the prepared composites were measured using Archimedes' method **(equation 3.2)** and their theoretical density were estimated assuming a rule of mixtures and taking the densities of Silica, Al_2O_3, BG, and graphene/GO to be 2.2, 3.98, 2.72 and 2.1 g/cm^3 [129] respectively.

$$\rho = m_1 \rho_o / m_2 - m_3 \qquad \textbf{(3.2)}$$

Where, ρ is the density of the sample, ρ_o is the density of the water, m_1 is mass of the sample is air, m_2 is mass of the water soaked sample and m_3 is mass of the sample in water. For samples with closed porosities $m_1 = m_2$.

3.4.3 X-ray Diffraction (XRD)

XRD was used to determine the final crystalline phases in the sintered samples. XRD was done using Siemens Diffraktometer-D5000 instrument. XRD instrument was operated in reflection mode with Cu-Kα incident radiation from 5-70° (2 theta) with a step size of 0.033^o. XRD spectra were analysed using X'Pert HighScore Plus software. To determine the crystalline to amorphous ratio in a XRD spectrum JADE 5.0 software was used.

3.4.4 Raman Spectroscopy

Raman spectroscopy was performed using Renishaw inVia Raman microscope. The samples were excited with a 514 nm argon laser with the power and

spot size maintained at 12.5 mW and 5 μm, respectively. The Raman spectra spanning between 100 and 3200 cm-1 was obtained three times for each sample after 12 accumulations. Raman is a very sensitive instrument for investigating any change or damage in carbon nano-materials. A typical Raman scan of GNP/GONP consists of D (1350 cm^{-1}), G (1585 cm^{-1}) and 2D (2700 cm^{-1}) peaks **(Figure 3.8)** where D peak corresponds to local defect/disorders, G peak corresponds to sp^2 graphitised structure and shape and intensity of the 2D peaks gives some idea about the number of layers in a graphene flake [130]. The ratio of the D and G peak intensities can give information about the defect concentration in graphene flakes (I_D/I_G). Raman spectroscopy was used to analyse the effect of high temperature sintering and mechanical properties characterisations on GNP and GONP in glass/ceramic composites. It was also used to quantify the alignment of GNP and GONP in glass/ceramic matrices. **Figure 3.8** shows a Raman spectrum of GNP film produced using liquid phase exfoliation method. Typical D, G and 2D were observed corresponding to defects/disorder, sp^2 graphitised structure and no. of layers in a graphene flake.

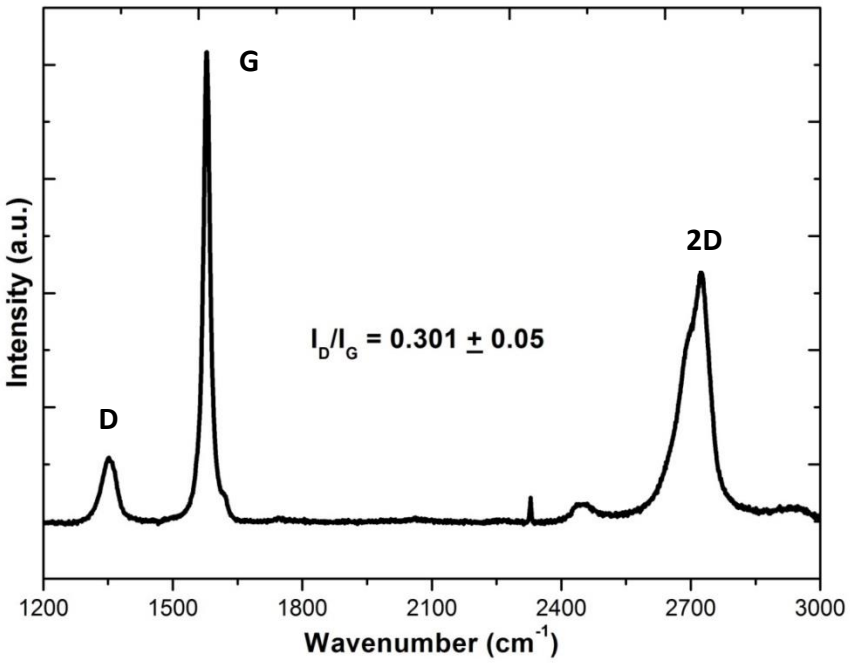

Figure 3.8 Raman spectrum of a GNP film showing D, G and 2D peaks with I_D/I_G ratio of 0.301 typical for liquid phase exfoliated graphene films.

3.4.5 Scanning and Transmission Electron Microscopy (SEM, TEM)

High resolution images of the fractured surfaces of nano-composites were taken using a FEI–Inspect F SEM at 10-20 KV accelerating voltage with 5-10 mm working distance. Samples for SEM were prepared after fracturing nano-composites and coating the fractured surfaces with Carbon. Carbon coating was needed to form a conductive layer on the sample surfaces before analysing in SEM. SEM was used to analyse both dispersion of GNP/GONP and understand the behaviour of crack in the glass/ceramic matrix.

TEM analysis was done to investigate the length, width and thickness of GNP produced using liquid phase exfoliation. TEM measurements were done using a JEOL JSM-2010 microscope. Samples for TEM were prepared after diluting the GNP suspensions and drop casting them onto carbon grids. TEM statistics were done

after counting length, width and thickness of >100 graphene flakes using Image J and origin image analysis softwares. **Figure 3.9 a)** shows a TEM image of graphene produced by liquid phase exfoliation. **Figure 3.9 b)** shows statistics of the graphene produced using liquid phase exfoliation. The average lateral dimension of the flakes was ~1.5 µm and thickness ~3 layers as measured by the edge counting method [131].

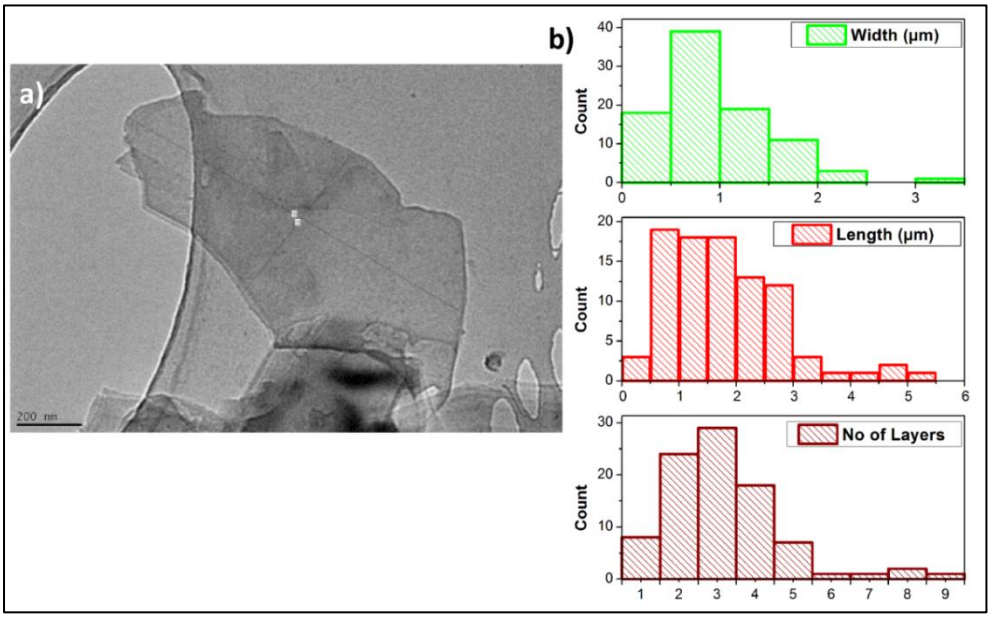

Figure 3.9 a) TEM image and; **b)** statistics showing average length, width and thickness of graphene produced using liquid phase exfoliation method.

3.4.6 Grain Size Analysis

The alumina-GNP samples for grain size analysis were prepared by thermal etching polished surfaces at 1200 ^{o}C for 30 minutes dwell time with a heating and cooling rate of 5 ^{o}C/min using a Carbolite furnace HTF- 1800. SEM images were

taken of the etched grains and analysed using Image J software. The grain size was determined by the line intercept method which involves counting the number of grain boundaries intercepted by a line of known length drawn on an SEM image of the sample. In all cases 10 lines were used per image and typically 4 images were chosen to calculate the grain size. In total 200 grains were counted for each sample.

3.4.7 Electrical Conductivity Measurements

The electrical conductivity measurements were performed for the BG-GNP composites using a two point probe method. The voltage was applied from 0 to 1 V using an Agilent voltmeter in steps of 0.1 V and I-V curves were recorded. Resistivities of the samples were determined using the formula $\rho = (R \times A) / L$, where R is the resistance, A is the cross sectional area and L is the length of the sample. Silver paste was used to prepare the electrodes on the cross sectional areas of the samples.

3.4.8 Mechanical testing

3.4.8.1 Chevron Notch Fracture Toughness Measurements

The Chevron notch technique was used for fracture toughness determination of the glass/ceramic nano-composites. Chevron notches with an angle of 90° were introduced into each bar (having rectangular cross-section of 2 mm x 3 mm) using an ultra-thin diamond blade on a precision saw Isomet 5000 (Buehler, USA). A universal testing system Instron 8862 (USA), equipped with a three point bend test fixture, with a span of 16 mm, was used to apply the loading. A span of 16 mm is widely accepted [132-135] for obtaining a valid value of the fracture toughness unless the specimen geometry has a span-to-thickness (height) ratio of less than 4

[134]. **Figure 3.10 a)** shows the three point bending test setup with an alumina-GNP beam with a chevron notch. The calculation of the geometric function Y^*_{min} for CVN bend bars with chevron notch depth (a_0) and specimen height (W) was based using the Bluhm's slice model [136] and a simplified solution of normalized stress intensity factors for chevron-notched specimens. The procedure used for the purposes of this investigation has been described elsewhere [137, 138]. The Bluhm's slice model helps to obtain an appropriate geometry of the chevron notch when the specimen dimensions are different from the standardized geometry (3 mm x 4 mm x 45 mm) [ASTM C1421, Standard Test Method for Determination of Fracture Toughness of Advanced Ceramics at Ambient Temperature, 2002]. The reliability of this approach is described elsewhere [132]. The chevron notch depth, a_0, was measured from SEM micrographs of the fractured specimens and the values varied between 0.60 and 0.65 mm for the individual samples, which corresponds to the recommended value in the ASTM standard (0.02 - 0.025 of height W). The chevron notch thickness was less than 0.20 mm in all cases. A cross–head speed of 1 μm/min was used in all tests to achieve slow crack propagation during loading. An inductive extensometer was used to measure deflection, and force–deflection curves were recorded. Stable crack propagation was achieved for all samples. The fracture toughness values were calculated using the maximum force evaluated from the force–deflection curve and the specimen dimensions using the following equation [5, 138].

$$K_{1c} = F_{max}/BW^{1/2}.Y^*_{min} \qquad \textbf{(3.3)}$$

Where Y^*_{min} is the minimum of geometrical compliance function, and *B* and *W* are the width and height of specimens, respectively. At least 3 beams were tested for each sample.

3.4.8.2 Vickers Indentation Toughness and Hardness

Indentation hardness values were measured for glass/ceramic nano-composites using a Vickers indentations machine **(Figure 3.10 (b))** with a load of 9.8 N for 10 seconds (Zwick/Roell ZHU/Z2.5, Ulm, Germany). The Martens hardness (HM) was calculated for silica nano-composites automatically by dividing the maximum test force P by the surface area of the indenter penetrating beyond the original surface of the test piece.

The indentation fracture toughness (IF) was estimated for the alumina-GNP composites from the crack lengths produced by Vickers indentations. Calculation of the fracture toughness was done using the equation proposed by Anstis [99].

$$K_{IC} = 0.016.\left(\frac{E}{H}\right)^{1/2} \cdot \frac{P}{c^{3/2}} \qquad \textbf{(3.4)}$$

Where *E* is the Young's modulus of materials, *H* is the hardness of materials, *P* is the indentation load and *c* is the indentation cracks length. At least 10 indents were measured for each sample in randomly chosen and well separated areas. Radial crack lengths were measured using a confocal microscope (Olympus Lext OLS 3100).

3.4.8.3 Elastic Modulus

The elastic modulus of silica composites was determined using the slope of the stress-strain curves produced during indentation while for alumina composites was determined on the polished test bars 2 x 3 x 20 mm^3 using the resonance method using a GrindoSonic Mk5i (J.W. Lemmens N.V., Belgium), and at least 10 readings were taken for each sample. It should be noted that because glass/ceramic nano-composites were anisotropic, all composites were tested on a surface with a normal parallel to the pressing direction of SPS. **Figure 3.10 c)** shows the setup for measuring elastic modulus using resonance method.

3.4.8.4 Tribological Properties

The wear behaviour of the silica composites were studied in unlubricated ball-on-disc experiments [ASTM G99-03, Standard test method for wear testing with a pin-on-disk apparatus, 2003] using a tribometer (DTHT 70010, CSM Instrument, Switzerland, **Figure 3.10 (d)**), against commercial borosilicate and alumina balls (with a diameter of 6 mm). The samples were in the form of polished disks with a diameter of 20 mm and thickness of 3 mm. The tested surface was ground and polished with a final diamond suspension of 3 μm (roughness Ra < 0.25 μm). The specimens were tested normal to the major surface of the sample with an applied load of 5 N for silica composites. The tests were performed in air with a relative humidity of 40 ± 5 %. The total sliding distance was 100 m (borosilicate balls) and 500 m (alumina balls), and the sliding velocity was 0.1 ms^{-1} for both cases. The coefficient of friction was continually recorded during the tests and the average value was calculated for each test within the distance of 100 and 500 m for the BS and alumina balls respectively. The wear volume of each specimen was calculated from

the surface profile traces (at least 6) across the wear track and perpendicular to the sliding direction using a profilometer (Mitutoyo SJ-201, USA), or by using a high precision confocal microscope (PLu neox 3D Optical Profilometer, Sensofar, Spain).

The specific wear rate (r) is defined as the worn volume (V) per loading force (F_p), per sliding distance (L), i.e.:

$$r = \frac{V}{F_p.L}\left[\frac{mm^3}{N.m}\right] \quad \textbf{(3.5)}$$

The worn volume was estimated from the following equation:

$$V = A.2\pi R[mm^3] \quad \textbf{(3.6)}$$

Where A is the average value of at least 6 different measurements of cross section area of the wear track estimated by profilometer or confocal microscopy, and R is sliding radius (7 and 3.5 mm). It should be noted two kinds of balls (borosilicate and alumina) were used to investigate the wear properties of silica nano-composites. Detailed analysis of the wear tracks as well as the wear debris, along with EDS analysis of the wear tracks, were performed using SEM in order to investigate the wear mechanisms.

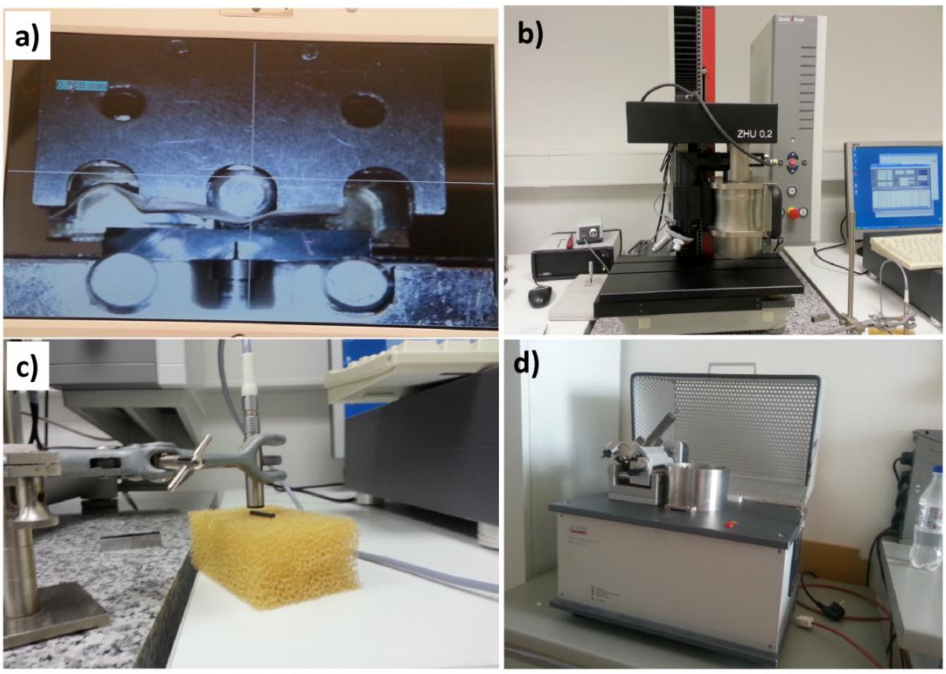

Figure 3.10 a) Three point bending test setup; **b)** Zwick/Roell ZHU/Z2.5 indentation machine; **c)** setup for measuring elastic modulus using ultrasonic method and; d) DTHT 70010, CSM Instrument tribometer.

3.4.8.5 Scratch Testing

The scratch test parameters reported in ISO 20502 for ceramic coating were adopted for alumina-GNP composites. To perform progressive load scratch testing, a Scratch tester UMT-2 (Bruker, USA) was used. The scratch tests were conducted with a standard Rockwell diamond indenter (200 µm tip radius). The normal load started at 1 N and increased linearly during the scratch test up to a pre-defined maximum load of 200 N (with an accuracy of 10 mN), over a displacement of 10 mm. A constant speed of the indenter displacement of 0.01 mm/s was used. The sample surfaces for the scratch testing were polished with a final diamond suspension of 1 µm. The normal (penetration) force, coefficient of friction, indenter

displacement and acoustic emission signal were continuously recorded during the testing. After the tests, the scratch grooves were examined using a confocal microscope (PLu neox, Sensofar-Tech, S.L., Spain) in order to assess both the profile and optical appearance of the scratch grooves. Detailed analysis of the scratch grooves were performed using Scanning Electron Microscopy (SEM, JEOL 7000F, Japan) in order to investigate the micro-damage mechanisms. The lengths at which radial cracks and chipping initiated were measured by analysing the SEM images using ImageJ software.

Chapter 4 In-situ reduction of graphene oxide nanoplatelet during spark plasma sintering of a silica matrix composite

4.1 Introduction

So far the improvement in the properties of graphene nano-composites has been limited because of the difficulty in producing single layer graphene flakes. The strong van der wall forces between graphene layers leads to GNP formation when using liquid phase exfoliation or milling methods. On the other hand these forces can be overcome by oxidising the graphene which avoids re-agglomeration of graphene flakes, but in turn compromises its excellent electrical properties. Oxidised graphene is easy to disperse in aqueous solvents and can be used to produce GONP reinforced glass/ceramic composites. Authors have reported reduction of GONP either by using chemical or thermal methods [35, 111]. Spark plasma sintering (SPS) uses pulsed direct current in an inert/vacuum environment to achieve very high heating rates, thus reaching the sintering temperature in just a few minutes. The inert and high temperature conditions in SPS are sufficient for reducing GONP to GNP during sintering [111]. Although authors have reported reduction of GONP during sintering in SPS, no systematic study has been performed to understand the reduction process in detail during SPS.

In the present work, the processing conditions for preparing well dispersed silica-GNP/GONP composites are discussed. Colloidal and powder processing routes were investigated with different solvents including ethanol, deionized (DI) water, n-methyl pyrrolidone (NMP) and di-methyl formamide (DMF). SPS was used to consolidate the powders. SPS avoided any damage/decomposition of GNP/GONP by minimizing the sintering times while reducing GONP to GNP during sintering. In-situ reduction of GONP in SPS was investigated for various sintering times and temperatures using Raman spectroscopy and XRD analysis. Finally, the conditions for preparing well dispersed and reduced silica-GONP composites were optimised avoiding crystallization of the nano-composites.

4.2 Experimental Section

GNP and GONP were used for optimising the fabrication conditions for preparing silica nano-composites using various processing routes and solvents. Details about the processing of GNP and GONP silica composites powder mixtures are provided in **chapter 3**. SPS was used for the sintering of silica-nanocomposites. Various sintering temperatures and times were investigated to understand the in-situ reduction of GONP to GNP during SPS processing without crystallising the silica matrix. The prepared composites were characterised using SEM, Raman and XRD.

4.3 Results and Discussion

Figure 4.1 shows the shrinkage rate (blue curve), temperature (red curve) and pressure profile (black curve) of the silica-GONP (2.5 vol%) composite. To optimise the processing conditions, the nano-composites were sintered at 1200 ^{o}C [5] with a 6 minutes dwell time. The short dwell time minimized any structural damage of the GNP/GONP during high temperature processing.

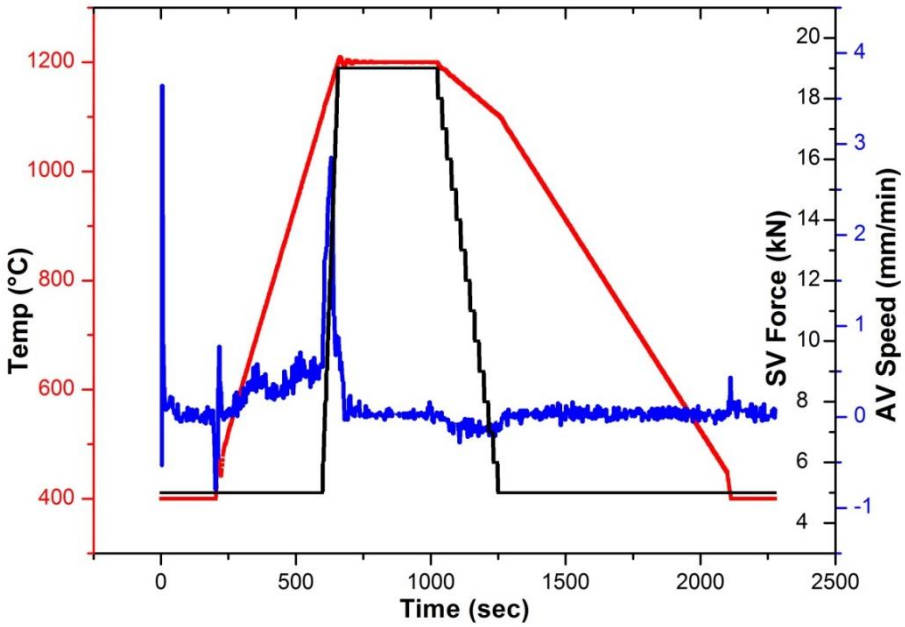

Figure 4.1 Shows shrinkage rate (blue curve), temperature (red curve) and pressure (black curve) profile for silica-GONP (2.5 vol%, ethanol and colloidal processing) composite during SPS processing (1200 ^{o}C/ 50 MPa/ 6 min). The shark shrinkage peak indicates viscous flow sintering mechanism for silica-GONP composite.

Table 4.1 lists the processing methods, solvents, sintering conditions, and bulk and relative densities of the pure silica, silica-GONP (2.5 vol%) and silica-GNP

(5 vol%) composites along with qualitative analysis of their dispersion. All of the samples were at least 98% dense except for the silica-GNP (5 vol%) sample processed using the powder processing route and NMP as the solvent. The low density of the NMP sample can be explained because of its high boiling point (205 ^{o}C), which was not sufficient for complete evaporation of the solvent at 200 ^{o}C. During sintering the trapped solvent formed bubbles thus inhibiting complete densification.

Table 4.1 Bulk and relative theoretical densities of prepared silica GNP/GONP (2.5 and 5 vol%) composites along with processing methods, solvents and sintering conditions. All the samples were sintered at 1200 ^{o}C under 50 MPa pressure for 6 minutes. The quality of the GNP/GONP dispersion is also qualitatively described.

Sample	**Bulk Density (g/cm^3)**	**% Relative Density**	**Dispersion**
SiO_2	2.18	99.2	-
SiO_2 + GONP (2.5 vol%) (Colloidal-Ethanol)	2.19	99.5	Very Good
SiO_2 + GONP (2.5 vol%) (Colloidal-DI water)	2.16	98	Poor
SiO_2 + GNP (5 vol%) (Colloidal-DMF)	2.16	98.1	Fair
SiO_2 + GNP (5 vol%) (Powder-NMP)	1.94	87.9	Good

In order to evaluate the quality of the dispersion of the GNP and GONP in the silica matrix, SEM images of fractured surfaces of the silica nano-composites were studied. **Figure 4.2 (a)** shows an SEM image of a fractured surface of the silica-GONP (2.5 vol%) composite prepared using the colloidal processing route and ethanol as the solvent. The GONP was found to be well dispersed and preferentially aligned perpendicular to the applied uniaxial pressing direction in the silica matrix (**figure 4.2 (a)**, arrow indicates the pressing direction). **Figure 4.2 (b)** shows an SEM image of a fractured surface of the silica-GONP composite prepared using the colloidal processing route and DI water as the solvent. The GONP was found to be agglomerated and poorly dispersed in the silica matrix (**figure 4.2 (b)**, arrows indicate silica and agglomerated GONP). The reason for the good dispersion of GONP in ethanol compared to its poor dispersion in DI water can be related to the good affinity of GONP to the alkyl and hydroxyl groups present in ethanol compared to only hydroxyl functional groups in DI water. As GONP also contains both alkyl and hydroxyl functional groups it is possible that it had a better affinity and interaction with the functional groups of ethanol compared to DI water. **Figure 4.2 (c)** shows an SEM image of a fractured surface of the silica-GNP (5 vol%) composite prepared using the colloidal processing route and DMF as the solvent. There was good dispersion of GNP in the silica matrix but some agglomerates of the GNP were present as highlighted in **figure 4.2 (c)**. Although DMF is a good solvent for producing good quality dispersions of GNP, the colloidal processing route using DMF was not the best method for fabrication of these composites. **Figure 4.2 (d)** shows an SEM image of a fractured surface of the silica- GNP (5 vol%) composite produced using the powder processing route and NMP as the solvent. It is clear from

the SEM images that the GNP was damaged during the processing (also confirmed by Raman spectroscopy) as highlighted in **figure 4.2 (d)**. Because of the high boiling point of NMP, the powders were dried at 200 ^{o}C in air, which resulted in damage of the GNP as a result of oxidation. Also, residual porosity was observed **(Table 4.1)** because it was not possible to completely remove the solvent from the powders. NMP has been reported in the literature [41, 131] to be a good solvent for producing GNP suspension but because of its high boiling point it is not suitable for drying in air. Although GNP was damaged during drying, the quality of GNP dispersion was still satisfactory; suggesting that powder processing might still be a promising method for fabricating these composites. Similar to silica-GONP (ethanol) composite, alignment of GNP was also observed in silica-GNP (NMP) composites. The best dispersion and densification was obtained for silica-GONP composites prepared using the colloidal processing route and ethanol as the solvent, and sintered at 1200 ^{o}C, 50 MPa pressure and 6 minutes of dwell time.

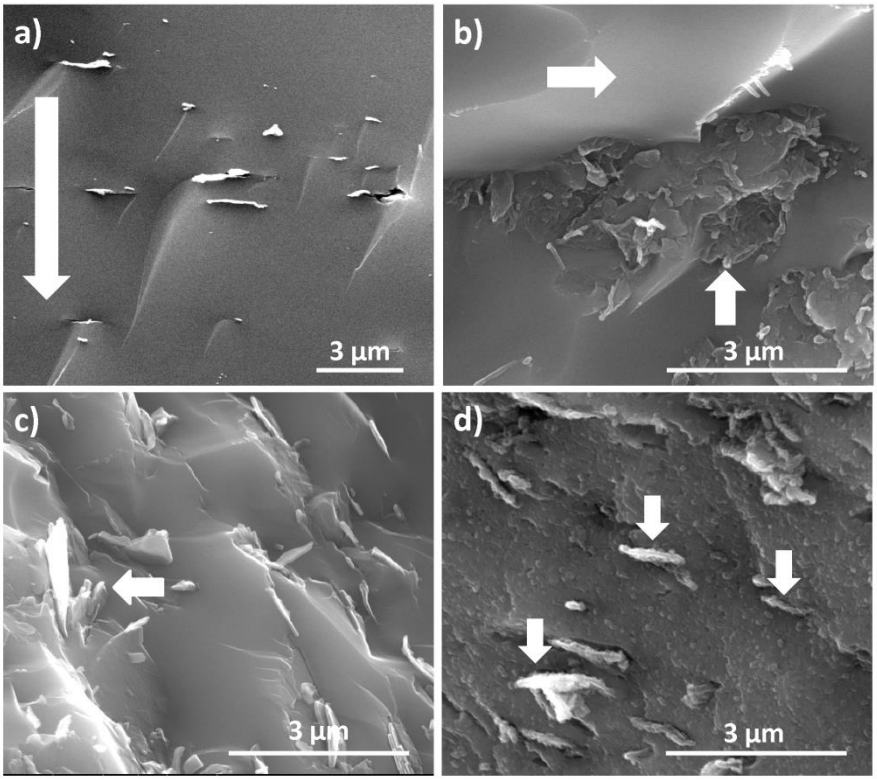

Figure 4.2 SEM of fractured surfaces of silica-GONP (2.5 vol%) and silica-GNP (5 vol%) nano composites: **a)** colloidal processing using GONP in ethanol (arrow showing direction of applied pressure during SPS); **b)** colloidal processing using GONP in DI water (arrows showing agglomerated GONP); **c)** colloidal processing using GNP in DMF (arrow showing dispersion of GNP) and; **d)** powder processing using GNP in NMP (arrows showing well dispersed but damaged GNP).

GONP contain large quantities of H_2O molecules and oxide groups of –OH (hydroxyl), -COOH (carboxyl) and >O (epoxy) [139]. This results in distorted sp^3 hybridised geometry of the carbon atoms in GONP and thus poor electrical properties. Therefore, after optimising the processing method and sintering conditions for silica-GONP composites, reduction of GONP to GNP is necessary in order to achieve good electrical conductivity. In order to investigate the reduction of

GONP to GNP during sintering more samples were prepared of silica-GONP (2.5 vol%) composites using SPS. The sintering conditions were chosen in order to systematically investigate the effect of both different sintering times (1200 ^{o}C -6, 15 and 25 minutes) and temperatures (1100, 1200 and 1300 ^{o}C for 15 minutes dwell time) on the reduction of GONP to GNP **(Table 4.2)**. The prepared composites were analysed using Raman spectroscopy and XRD to understand the kinetics and mechanism of the reduction of GONP to GNP during high temperature SPS.

Table 4.2 Sintering conditions for silica-GONP (2.5 vol%) composites prepared using different sintering times and temperatures for investigating the reduction of GONP to GNP.

Temperature (^{o}C)	**Dwell Time (minutes)**	**Pressure (MPa)**	**Crystallization**
1200	6	50	No
1200	15	50	No
1200	25	50	Yes
1100	15	50	No
1300	15	50	Yes

Figure 4.3 shows Raman spectra of GONP powder and silica-GONP (2.5 vol%) composites: **a)** sintered at 1200 ^{o}C, 50 MPa pressure for 6, 15 and 25 minutes of

dwell time and; **b)** sintered at 1100, 1200 and 1300 ^{o}C, 50 MPa pressure for 15 minutes of dwell time. The typical D (~1350 cm^{-1}), G (~1585 cm^{-1}), 2D (~2700 cm^{-1}) and D+G (~2940 cm^{-1}) peaks were observed for GONP and silica-GONP composites [130, 140]. The two main peaks, D and G bands, are related to defects and sp^2 hybridised carbon respectively for GONP. There are two weaker intensity peaks related to the Π bond in the graphitic electronic structure (2D band) and disorder (D+G band) [140]. **Figure 4.3 a)** shows the change in the I_D/I_G ratio for GONP and silica-GONP composites sintered at 1200 ^{o}C with increasing dwell times of 6, 15 and 25 minutes. The I_D/I_G ratio for pure GONP was 1.08 which increased to 1.10 and 1.14 for silica-GONP composites sintered at 1200 ^{o}C for 6 min and 15 minutes respectively. With further increase in the dwell time (25 minutes) the I_D/I_G ratio decreased to 0.91. The increase in the I_D/I_G ratios can be explained by the reduction of GONP to GNP during high temperature processing. Usually, the I_D/I_G ratio is a measure of the disorder of the carbon, as expressed by the sp^3/sp^2 carbon bonding ratio [141]. An increase in I_D/I_G ratio corresponds to an increase in the disorder of carbon. In recent work by Ramirez et al. [111] suggested that the reduction of GONP occurs in two stages. In the first stage at 800 ^{o}C the I_D/I_G ratio increased. This was possibly due to rupture of the bonds induced by partial removal of functional groups. In the second stage at 1500 ^{o}C, the I_D/I_G ratio decreased significantly suggesting the removal of carbonyl, carboxyl and epoxy groups and the recovery of highly crystalline graphitic structure. So the decrease in I_D/I_G ratio with increasing dwell time at 1200 ^{o}C suggests the recovery of the highly crystalline graphitic structure in the silica-GONP (1200 ^{o}C-25 min) composites. A similar phenomenon has been observed by other authors for reduced GONP [111]. In the case of processing the silica-GONP composites at different temperatures **(Figure 4.3 (b))** a continuous

decrease in I_D/I_G ratio was observed with increasing temperature. The I_D/I_G ratio in case of silica-GONP sintered at 1100 ^oC for 15 min was 1.31 which reduced to a value of 0.66 for the silica-GONP sintered at 1300 ^oC for 15 min. Comparing the I_D/I_G ratio of the composites sintered at 1100 (1.31) and 1200 ^oC (1.14), it was confirmed that reduction of GONP to GNP was in its second stage i.e. recovery of the crystalline graphitic phase. The small I_D/I_G ratio of 0.66 in the case of silica-GONP (1300 ^oC-15 min) composite confirms the full recovery of highly crystalline graphitic phase. It should be noted that I_D/I_G ratio in the case of liquid phase exfoliated GNP is in the range from ~0.2 to 0.6 depending on the sonication time. In addition to the I_D/I_G ratio, the change in intensity of 2D and D+G band can also be used to quantify the reduction of GONP. The intensity of the 2D band is lower than the D+G band in GONP because of the presence of defects and disorder. As the GONP is reduced thermally, defects and disorder in its electronic structure are decreased. Thus we see a decrease in the intensity of D+G band while the intensity of the 2D band increases **(Figure 4.3)**. Thus, Raman spectroscopy results confirmed the reduction of GONP to GNP at high temperatures in the reducing environment of SPS.

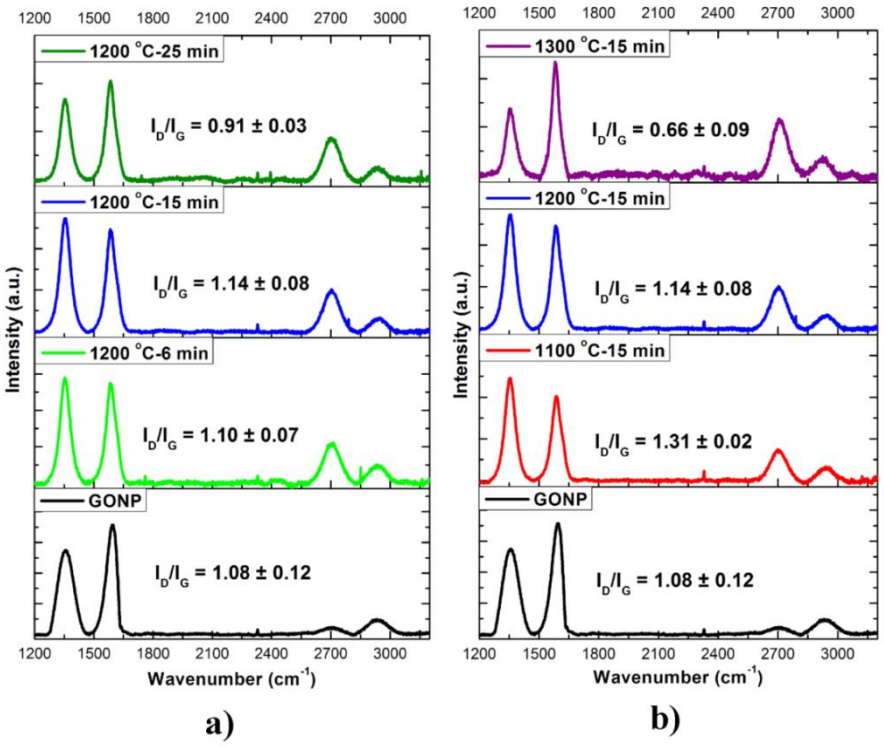

Figure 4.3 Raman spectra of: **(a)** GONP and silica-GONP composites sintered at 1200 ^{o}C for different dwell times; and **(b)** GONP and silica-GONP composites sintered at different sintering temperatures for 15 minutes of dwell time.

Both the reduction of GONP and crystallisation of silica with increasing sintering times and temperatures were investigated using XRD analysis. In order to optimise the processing conditions for preparing silica-GONP composites we would like to reduce GONP at high temperatures without crystallisation of the silica matrix. **Figure 4.4 a)** shows the XRD patterns for GNP, GONP powders and pure silica sintered at 1200 ^{o}C for 6 minutes of dwell time. The sharp crystalline peaks at 26.3^{o} and 11.4^{o} correspond to the crystalline phases of GNP and GONP respectively [139, 142] while a broad peak at ~21^{o} corresponds to amorphous silica. GONP has a peak at a lower angle (11.4^{o}) compared to GNP (26.3^{o}) because of its large interlayer distance. The intercalation of water molecules and other oxide groups in the case of

GONP increases the interlayer distance. The d spacing of GONP is ~0.9 nm compared to ~0.34 nm for GNP [35, 139]. The crystalline peak of GONP shifts to higher angles with reduction. The change in peak position is mainly because of the removal of trapped water molecules and oxide groups resulting in a decreased interlayer distance for reduced-GONP. **Figure 4.4 b)** shows the XRD patterns for silica-GONP composites sintered at 1200 ^{o}C for 6, 15 and 25 minutes dwell times. XRD confirmed that there was no reaction between silica and GONP during sintering. The sharp crystalline peak at ~26.3^{o} confirmed the reduction of GONP to GNP at 1200 ^{o}C during sintering. The intensity of the GONP increased with increasing dwell time suggesting the recovery of crystalline graphitic phase. The silica-GONP composite sintered at 1200 ^{o}C for 25 minutes dwell times started to crystallize (cristobalite-19 wt%) suggesting that long dwell times are not good for sintering silica nano-composites. **Figure 4.4 c)** shows the XRD patterns for silica-GONP composites sintered at 1100, 1200 and 1300 ^{o}C for 15 minutes dwell time. Similar to **figure 4.4 b)** the sharp crystalline peaks at ~26.3^{o} confirmed the reduction of GONP in all of the composites. Also, the peak intensity of reduced GONP increased with increasing sintering temperatures. This correlates with the Raman results where the I_D/I_G ratio decreases with increasing sintering temperatures. The composite sintered at 1300 ^{o}C formed a significant amount of cristobalite phase (62 wt%) (PDF 00-039-1425). In order to appreciate the effect of GONP on the crystallisation behaviour of silica matrix, pure silica samples were also sintered at 1200 ^{o}C and 1300 ^{o}C for 25 and 15 minutes dwell times respectively. The pure silica samples were found to be fully crystallized (cristobalite-100 wt%) compared to 19 wt% (1200 ^{o}C-25 min) and 62 wt% (1300 ^{o}C-15 min) crystallinity in the case of silica-GONP composites for the same sintering conditions, suggesting that GONP

inhibited the crystallisation of the silica matrix. Carbon nanostructures are known to increase the crystallization temperatures of glasses possibly because of increased viscosity, reduced mobility of silica particles bound to GNP or to the local stiffness of GNP opposing the volume reduction associated with the crystallisation of glasses [5]. The increase in viscosity can also be confirmed by comparing the sintering temperatures of pure silica and silica-GONP (2.5 vol%) composites which was shifted to higher temperatures by ~70 to 100 ^{o}C for the nano-composites (data not shown). The GONP delayed the crystallization of silica up to a limit but the sintering temperatures used were still high enough to crystallise silica. The best sintering conditions for reducing GONP to GNP without crystallizing the composites were found to be 1200 ^{o}C with 50 MPa pressure and 15 minutes of dwell time. Higher temperatures can further improve the crystallinity of the graphitic structure of GNP but they also cause the crystallization of the silica.

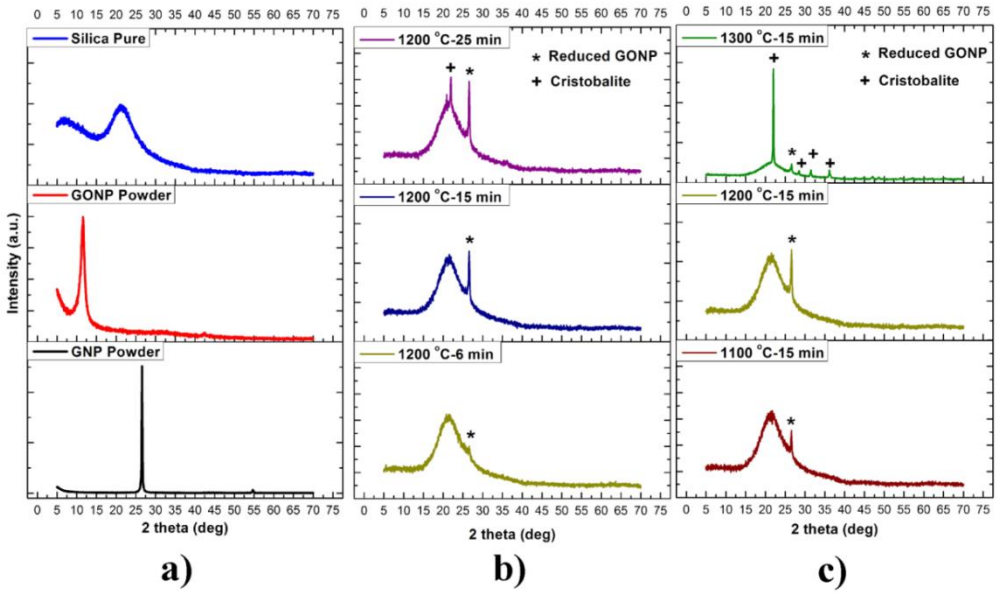

Figure 4.4 XRD patterns of **a)** pure GNP, GONP powders and silica sintered at 1200 ^{o}C for 6 minutes dwell time; **b)** silica-GONP composites sintered at 1200 ^{o}C for different dwell times; and **c)** silica-GONP composites sintered at different sintering temperatures for 15 minutes dwell time.

4.4 Conclusion

The conditions for preparing well dispersed silica-GNP and silica-GONP nano-composites were optimised using powder and colloidal processing routes in different solvents including ethanol, DI water, NMP and DMF. The best results were obtained for the silica-GONP (2.5 vol%) composite produced using a colloidal processing route and ethanol as the solvent. Raman spectroscopy and XRD results confirmed that the GONP was reduced to GNP during high temperature processing in SPS. Composites sintered at 1200 ^{o}C, 50 MPa pressure and 15 minutes dwell times showed the recovery of crystalline graphitic phase of GNP after reduction without crystallizing the silica matrix. The GONP was found to inhibit the crystallisation of the silica matrix, possibly due to increased viscosity and reduced mobility of silica particles bound to GNP resulting in decreased crystallinity of silica nano-composites compared to pure silica.

Chapter 5 Toughened and machinable glass matrix composites reinforced with graphene-oxide nano platelets

5.1 Introduction

The majority of the work on ceramic composites in the last decade has been focussed on carbon nanotube (CNT) reinforced inorganic (glass and ceramic) matrix composites [2, 3, 9, 48, 78, 79, 143] because of their attractive combination of mechanical and multifunctional properties [144-146]. However, graphene apart from having similar properties to CNTs also has additional advantages such as: high specific surface area [15]; and less tendency to tangle, which makes them easier to disperse in a matrix (where as CNTs usually require surface modification [2]). Graphene is also relatively easy to produce, inexpensive and potentially less toxic compared to CNTs [17]. Recently Tapaszto [30] et al. compared the mechanical properties of silicon nitride-CNTs and silicon nitride-graphene composites with 3 wt% loading. According to their results, graphene was easy to process and disperse compared to CNTs, it also produced better mechanical properties. Similarly, Walker et al. [27] reported an improvement of ~235% in fracture toughness of silicon nitride-graphene (1.5 vol%) composites, while Fan et al. [107] reported an electrical conductivity of 1000 S/m with the addition of only 2.35 vol% graphene to an

alumina matrix. In view of these encouraging results, the use of graphene to produce reinforced inorganic matrix composites has great unexplored potential.

In the present study, GONP reinforced silica composites were prepared. Dispersion of GONP in the silica matrix was optimised with reproducible results using colloidal processing route. The details about the processing are provided in **chapter 3 and 4**. Composites with different volume fraction of GONP were prepared and their mechanical properties characterized. SPS was used to rapidly consolidate the composites, thus minimising any structural damage to GNP and GONP during high temperature sintering [70]. The results and discussion make reference to the corresponding results reported in the literature for silica-CNTs composites [5]. Finally, the machinability of silica-GONP nanocomposites was investigated and compared with that of pure silica.

5.2 Experimental Section

Silica nano-composites with GONP loading of 0.5, 2 and 2.5 vol% were prepared using colloidal processing method and sintered using SPS. Details about the optimisation of processing conditions, sintering and characterization of silica nanocomposites are provided in **chapters 3 and 4**.

The mechanical properties of the composites were characterised. The details of the mechanical testing are provided in **chapter 3**. The nanocomposites were characterised for chevron notch fracture toughness (K_{IC}), Martin's hardness (HM), elastic modulus (E) and machinability.

Brittleness Index (BI) was measured using equation (**5.1**) where HM is the Martin's hardness and K_{IC} is the chevron notch fracture toughness of the material.

$$BI = HM/ K_{IC} \qquad \textbf{(5.1)}$$

The machinability of dense silica and silica-GONP composites was evaluated by drilling the polished samples using a high speed rotating WC-Co driller. The rotation speed of the drill was 560 rpm and the contact load was controlled by hand in order to inhibit the bending of drill. The drilled surfaces of the samples were examined by SEM.

5.3 Results and Discussion

Silica-GONP composites prepared by colloidal processing showed the best dispersion results compared to all of the composites (for details refer to **chapter 4**). For this reason, nanocomposites with increasing content of GONP of 0.5, 2 and 2.5 vol% were prepared. Interestingly, silica-GONP composites were Raman inactive when observed in the direction perpendicular to the SPS pressing (**figure 5.1**). Thus confirming the preferential alignment of GONP in the silica matrix. Since GONP was aligned in a direction perpendicular to the applied force in SPS all the samples were tested for mechanical properties accordingly.

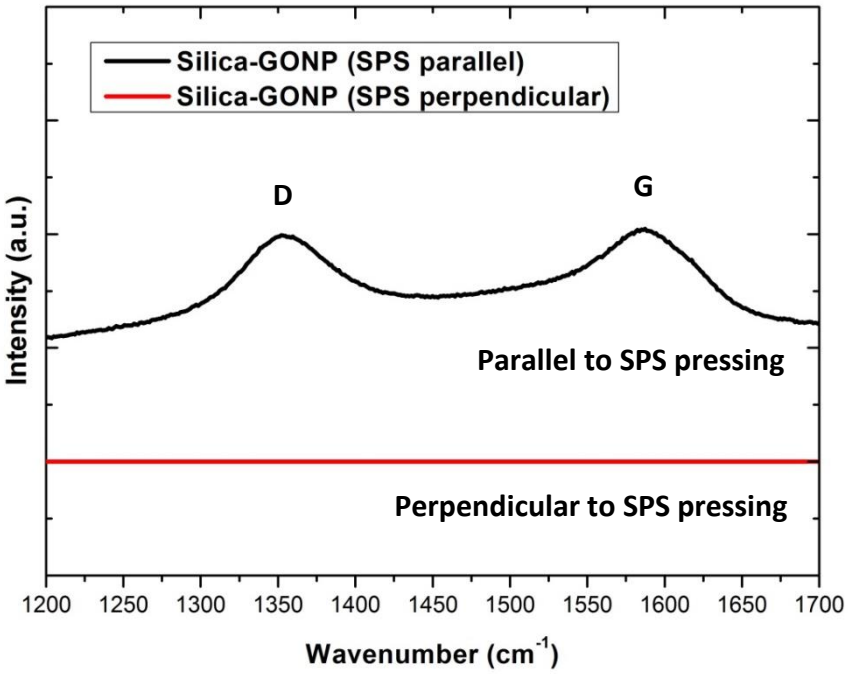

Figure 5.1 Shows Raman scans in the directions parallel and perpendicular to SPS pressing. Typical D and G peaks were observed for parallel SPS pressing direction while no peaks were observed for perpendicular SPS pressing direction confirming the alignment of GNP in silica matrix.

The effect of GONP content on the fracture toughness of silica was investigated. A fracture toughness of 0.67 MPa $m^{1/2}$ was measured for pure silica. The fracture toughness of the composites increased linearly with increasing content of GONP **(figure 5.2)** and reached a value of 0.89 MPa $m^{1/2}$ for 2.5 vol% loading, corresponding to an increase of ~35% compared to pure silica.

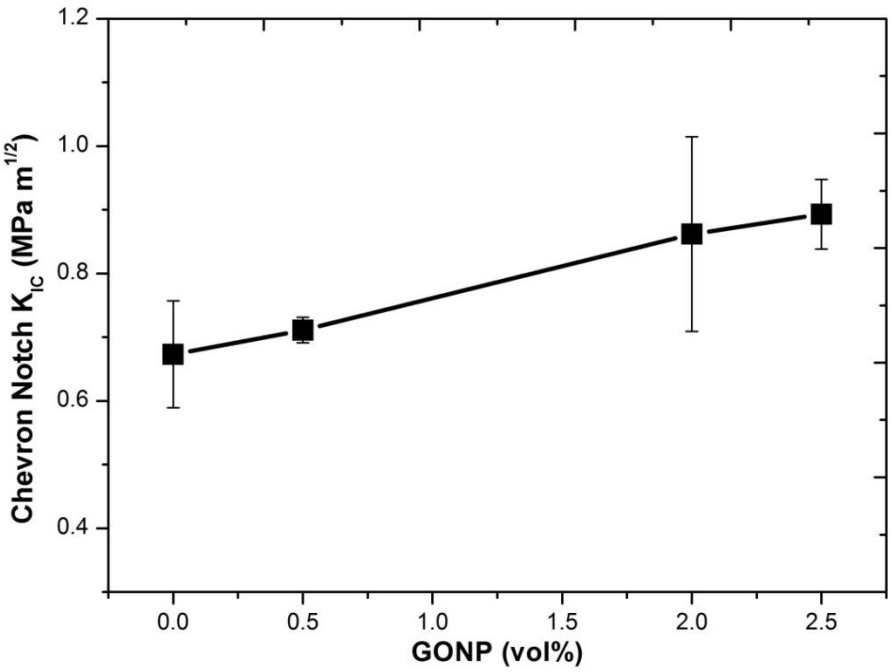

Figure 5.2 Fracture toughness of the silica-GONP nanocomposites measured with chevron notch fracture toughness method.

In order to understand the toughening mechanism of GONP compared to CNTs, the fracture toughness values of as prepared silica-GONP composites are compared to silica-CNTs composites from the literature, which were sintered, processed and characterized using similar conditions [5]. The silica-GONP composites had a toughness value of 0.89 MPa $m^{1/2}$ for 2.5 vol% loading while silica-CNTs composites had a similar value of 0.92 MPa $m^{1/2}$ for 7.5 wt% (9.67 vol%) loading, although the measured fracture toughness of pure silica was ~0.6 MPa $m^{1/2}$ [5] compared to 0.67 MPa $m^{1/2}$ in the present work. Thus, in order to achieve a fracture toughness of about 0.9 MPa $m^{1/2}$, the necessary GONP loading was three times lower compared to CNTs. This suggests that GONP may be more effective than CNTs in improving fracture toughness. The easier processability and the improved mechanical properties of GONP composites can be attributed to high

specific surface area; 2D geometry and better interfacial bonding of GONP compared to CNTs, which have a tendency to tangle and agglomerate.

5.3.1 Toughening mechanisms

To investigate the toughening mechanisms of GONP in silica, cracks generated from Vickers indentation were analysed. It was not possible to calculate fracture toughness and hardness values using the micro indentation (≥ 5 kg) technique because indentation of glass did not generate a well-defined radial/median crack system, but instead chipped and produced ill-defined indentation impressions **(figure 5.3)**. By varying the mass (1, 2, 3 and 5 kg) radial cracks were observed.

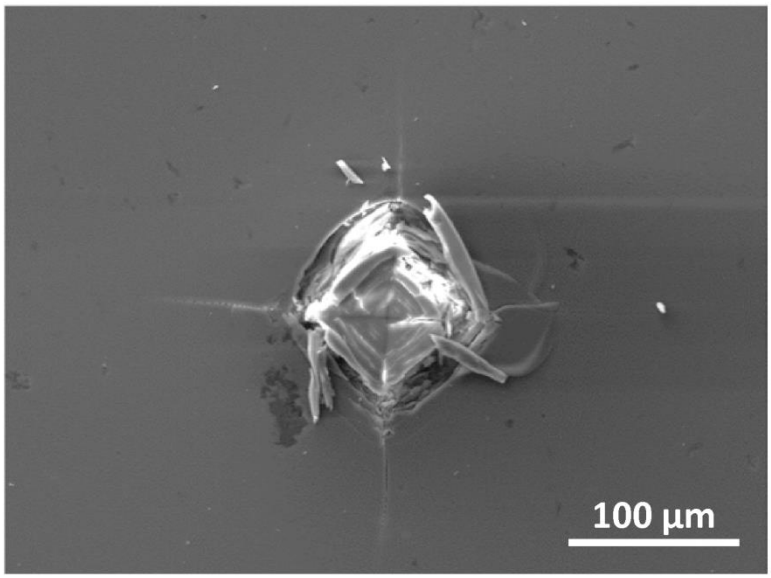

Figure 5.3 Vickers Indentation impression produced on silica-GONP composite.

Figure 5.4 shows SEM images of Vickers indentation cracks for silica and silica-GONP nanocomposites. **Figure 5.4 (a)** shows a typical straight crack path for pure silica. **Figure 5.4 (b)** is a low magnification image showing a wavy crack path and **Figure 5.4 (c)** shows a deflected crack path in the case of silica-GONP (2.5 vol%) composites. Necking and joining of the cracks can be seen in the case of the GONP composites.

The differential thermal expansion between GONP and silica might have induced local stresses in the silica matrix enabling crack deflection. In fact, during cooling due to negative coefficient of thermal expansion of GONP [107, 147] it expands while silica contracts, generating high residual stresses [148]. These residual stresses might reduce the susceptibility of the glass to fracture. **Figure 5.4 (d)** shows the anchoring of GONP in between the cracks showing GONP crack bridging toughening mechanism. **Figure 5.4 (e)** shows fractured surface of a chevron notch showing crack branching toughening mechanism. When a crack front interacts with GONP it deviates from its straight path. A crack is not able to propagate through the GONP so it is deflected. Crack deflection promotes energy dissipation through crack branching occurring along the edges of GONP. The inset of **Figure 5.4 (e)** depicts crack branching where GONP is sketched with grey colour and cracks with red colour. The crack branching toughening mechanism was observed in crystalline graphene composite materials as reported in Refs. [82, 100]. It should be noted that crack deflection and crack branching were found to be the dominant toughening mechanisms. **Figure 5.4 (f)** is a high magnification image showing GONP pull out from the silica matrix. The nature of the interfacial bonding between GONP and silica plays an important role in toughening response. Due to the good

interfacial bonding between the oxide layers of GONP and silica various toughening mechanism were observed for silica-GONP composites.

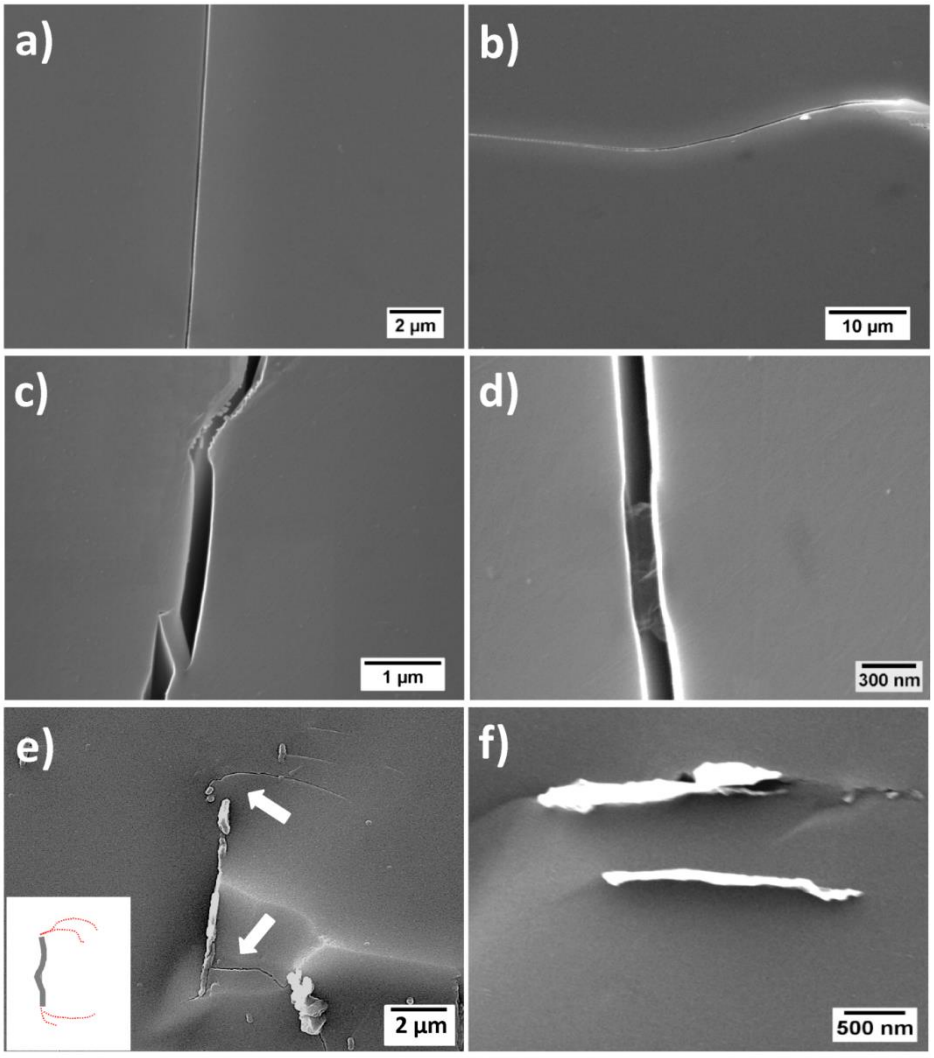

Figure 5.4 SEM fractured surface images of silica-GONP nanocomposites: **a)** Image showing straight crack path for pure silica; **b)** low magnification image showing wavy crack path for silica-GONP nanocomposites; **c)** crack deflection and GONP necking toughening mechanisms; **d)** high magnification image showing GONP crack brigding; **e)** chevron notch fractured surface image showing crack branching; and **f)** GONP pull out from silica matrix.

Table 5.1 summarizes the chevron notch fracture toughness, Martens hardness (HM), elastic modulus and brittleness index values for silica-GONP nanocomposites. Analogous to CNTs, GONP reduces the elastic modulus and hardness of the glass composites with increasing concentration. The elastic modulus and hardness of the composite decreases by ~19% and ~30% respectively for 2.5 vol% silica GONP composite. In the case of CNTs, the reduction in hardness and Young's modulus with increasing concentration of CNTs was attributed to CNT agglomeration in borosilicate glass composites [143]. In the case of GONP silica glass composites, the reduction in both elastic modulus and hardness was even more marked because of the presence of relatively large and weakly bonded graphene planes.

Table 5.1 Physical and mechanical properties of silica-GONP nanocomposites.

Sample	**Chevron Notch K_{IC} (MPa $m^{1/2}$)**	**Martens Hardness HM (GPa)**	**E-Modulus (GPa)**	**Brittleness Index ($\mu m^{-1/2}$)**
SiO_2	0.67 ± 0.08	3.51 ± 0.14	49.9 ± 2.6	5.24
SiO_2 + GONP (0.5 vol%)	0.71 ± 0.02	3.07 ± 0.06	49.1 ± 0.9	4.32
SiO_2 + GONP (2 vol%)	0.86 ± 0.15	3.04 ± 0.08	48.6 ± 1.2	3.53
SiO_2 + GONP (2.5 vol%)	0.89 ± 0.05	2.55 ± 0.05	40.18 ± 1.4	2.86

The brittleness index can be used to quantitatively determine the machinability of glass ceramics [149]. The lower the BI, the higher the machinability of the glass-ceramics. Interestingly, the increase in fracture toughness and decrease in hardness remarkably decrease the BI of silica-GONP composites. As reported by Boccaccini, the BI of machinable glasses should be lower than 4.3 $\mu m^{-1/2}$ [149]. In the case of silica-GONP (2.5 vol%) composites the BI value decreased from 5.24 to 2.86 $\mu m^{-1/2}$, corresponding to a ~50% decrease compared to pure silica. **Figures 5.5** shows SEM micrographs of drilling indentations on the polished surface of pure silica and silica-GONP (2.5 vol%) composite. The silica-GONP composite exhibited good machinability. In comparison with pure silica, the drilled surface of composite was smoother and there was less debris. Under the shear stresses generated by drilling, the pure silica showed material removal mechanisms by fragmentation and fracture so that the drilled surfaces were coarse **(figure 5.5 (a, b))**. During the drilling test, even under high loading of the drill, material removal was difficult. At longer drilling times, the drilling tip became red hot due to high friction. On the contrary, when drilling the GONP composites, it was found that the material removal was easier and the drilled surface was smoother and flat **(figure 5.5 (c, d))**. As expected, homogeneously distributed GONP flakes played an important role in dissipating the shear stresses and local heating in the silica matrix. Micro cracks were easy to nucleate and propagate along the relatively weak GONP and silica matrix interface **(figure 5.4)**. Also there was no significant local increase of temperature at the tip contact point (i.e. no red areas were observed). The addition of GONP produced a reduction in coefficient of friction [150, 151] and an increase in

thermal conductivity [113, 152] resulting in both reduced local heating and increased machinability.

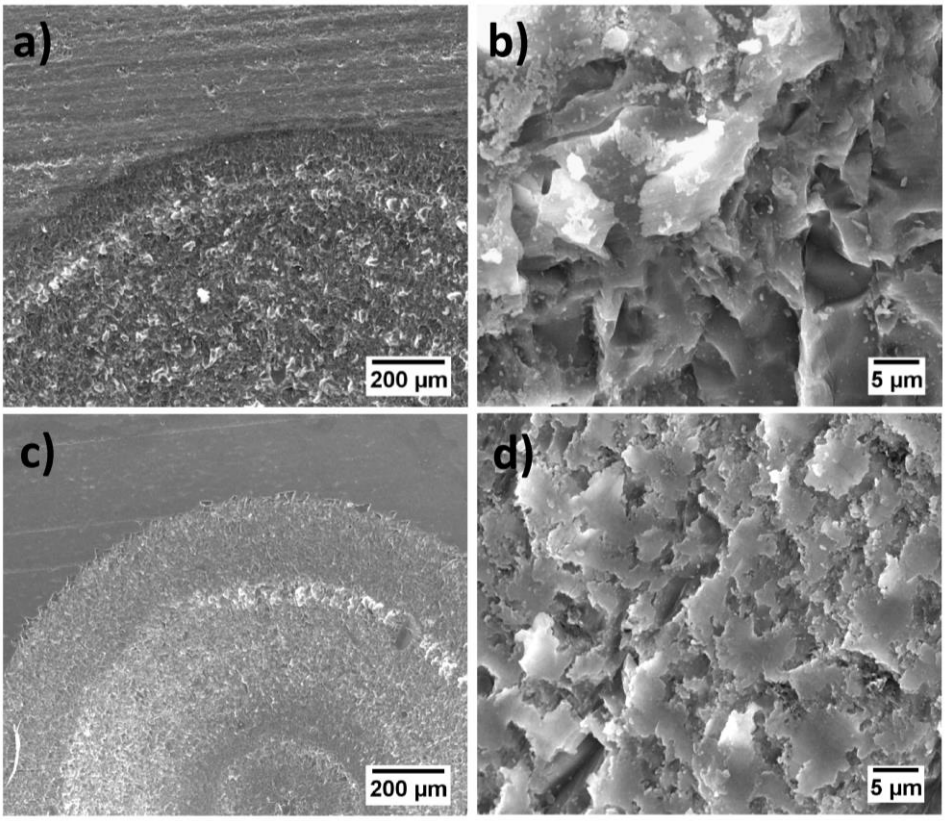

Figure 5.5 SEM images showing surfaces after drilling: **a)** low, and **b)** high magnification images for pure silica; and **c)** low, and **d)** high magnification images for silica-GONP (2.5 vol%) composite.

5.4 Conclusion

Using the optimized conditions, well dispersed and fully dense (relative density > 99%) silica-GONP composite powders were prepared using a colloidal processing route followed by SPS densification at 1200 ^{o}C with 50 MPa pressure. There was an improvement of ~35% in the fracture toughness of the composites with the addition of 2.5 vol% GONP as measured using the chevron notch fracture toughness method. Various toughening mechanism including GONP necking, GONP pull-out, crack bridging, crack deflection and crack branching were observed for silica-GONP composites. GONP induces local stresses in the silica matrix making cracks deviate from their normal straight path, increasing the fracture toughness of the composites. Hardness and brittleness index of the composites decreases by ~30% and ~50% respectively compared to pure silica. The addition of GONP to silica matrix enhanced the machinability of silica-GONP composites. Silica-GONP composites show easy processability and better mechanical properties when compared to silica-CNTs composites. This can be attributed to the higher specific surface area and 2D geometry of GONP compared to CNTs, which have tendency to agglomerate. The present study suggests that GONP is an effective reinforcing agent to prepare tougher and machinable glass matrix composites.

Chapter 6 Tribological properties of silica-graphene nano platelet composites

6.1 Introduction

The sliding and frictional behaviour of materials in reciprocal motion is extremely important for wide range of engineering application. Polymer matrix composites are of interest for engineering applications because of their light weight, low cost, high modulus of elasticity, good wear resistance and low friction [153]. Metal matrix composites have advantages like high strength, stiffness, relatively higher operating temperatures and wear resistance. The main limitations of using polymer or metal matrix composites are: polymer matrix composites have poor thermal stability, low hardness, and are reactive to moisture, chemicals and solvents, while metal matrix composites are sensitive to acids, bases, humidity and salts which limits their applications [154]. In order to avoid these problems glass matrix composites reinforced with carbon fibres were developed [155]. Carbon fibre reinforced glass composites has been a topic of research for the last three decades [156]. They have become an important class of advanced materials due to the limitations of polymer and metal matrix composites [157]. Glass matrix composites exhibit high hardness and are less sensitive to moisture, acids, chemicals or salts, along with the advantage that graphite fibre provides a self-lubricating effect to the composites [158].

Recently, with the discovery of graphene, research on composites has focussed on developing graphene reinforced ceramic , glass , polymer [129] and metal [159] matrix composites. Graphene consists of a two dimensional, one atomic layer thick sheet of carbon atoms. It has better mechanical [13], electrical [12] and thermal [160] properties compared to graphite. Also due to its high specific surface area compared to graphite, CNTs and carbon black, a small loading of graphene in a matrix can lead to significant improvements in properties. An improvement in the electrical properties of graphene nano-composites can be useful for electronic applications, while the high specific surface area and excellent mechanical properties of graphene can be useful for fabricating advanced composites with improved mechanical and tribological properties. Graphene composites are expected to have better tribological properties compared to graphite fibre reinforced glass composites along with improved electrical and thermal properties.

In the present study, silica composites with different vol% of GNP loading were fabricated using spark plasma sintering (SPS). SPS minimised any structural damage to GNP during high temperature sintering. The tribological properties of the fabricated composites were investigated for the first time using a ball on disc technique with both alumina and BS balls as the counterpart. The extent of damage to GNP after tribology testing was also quantified using Raman spectroscopy.

6.2 Experimental Section

Graphene was synthesised using liquid phase exfoliation as described in **chapter 3**. Silica-GNP composites with 2 and 5 vol% GNP loading were prepared using powder processing and DMF as the solvent. It should be noted that GNP and powder processing was used for the fabrication of composites instead of GONP and colloidal processing as described in **chapter 4 and 5**. There were two main reasons for this: 1) we wanted to try a processing route that can be used for commercial application and can be up scaled; 2) since, we were investigating the tribological properties of the composites we wanted to have a weaker interface in between GNP and silica matrix so that GNP can take part in the lubrication process during tribology test. In the case silica-GONP composites there was a good interfacial bonding between GNP and silica particles because of the presence of hydroxyl groups in both cases, which might have compensated the beneficial effect of graphene on the tribological properties of the composites.

Silica-GNP composites were sintered using SPS. The prepared composites were characterised for mechanical (fracture toughness, hardness, elastic modulus) and tribological (friction coefficient, wear resistance) properties. The normalised wear resistance of the composite was calculated by dividing the specific wear rate of pure silica (reference) with the specific wear rate of the composites. It provided a measure of the improvement in the wear resistance of the composite materials. Detailed analysis of the wear tracks as well as the wear debris, along with EDS analysis of the wear tracks, were performed using SEM in order to investigate the wear mechanisms. Raman spectroscopy was used to quantify the damage to GNP before and after tribology test.

6.3 Results and Discussion

Figure 6.1 is the chevron notch fractured surface SEM image of a silica-GNP (5 vol%) composite and shows the distribution of GNP in the silica matrix. GNP were found to be evenly distributed through the glass matrix and were aligned in a direction perpendicular to the applied force during SPS (arrow in **Figure 6.1** shows the pressing direction). Interestingly, the thickness of the GNP was larger than the as prepared GNP (~3 layers), synthesized using liquid phase exfoliation method, suggesting there was some overlapping of the GNP flakes during processing, which was also confirmed by Raman spectroscopy (discussed later).

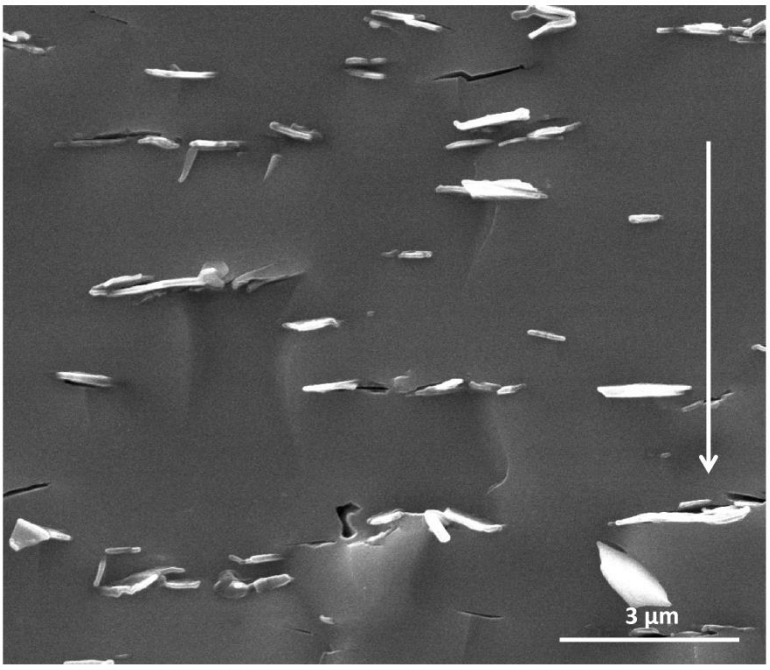

Figure 6.1 SEM image showing distribution of GNP in silica-GNP (5 vol%) composite.

Tribology testing was performed on silica, silica-GNP (2 vol%) and silica-GNP (5 vol%) composites. In order to understand in detail how the silica nano-composites will behave while in contact with hard materials like ceramics and softer materials like glasses, the wear properties of the silica-GNP composites were measured using both alumina and BS balls as the counterpart. **Figure 6.2** shows the change in the coefficient of friction with sliding distance for silica-GNP composites against alumina balls, where the top x axis represents the number of rotations for 500 m sliding distance. It is clear that as the concentration of GNP increases in the silica matrix the value of coefficient of friction decreases. In fact during sliding the friction between the alumina balls and silica composites is less due to the multilayer structure of GNP which provides a lubricating effect to the silica matrix, resulting in a reduced coefficient of friction. The coefficient of friction value for silica-GNP (5 vol%) composite was ~70% lower than that of the pure silica sample for the initial sliding distance of 1 m. As the sliding distance increased the coefficient of friction also increased due to both an increase in the roughness of the silica and the alumina ball surfaces and the progressively larger contact area between the contacting parts. It should be noted that the average coefficient of friction values for pure silica (0.69 ± 0.04) were similar to silica-GNP (2vol%) composite (0.71 ± 0.02). When GNP is added in small amounts it does not significantly affect the coefficient of friction, but when added above a critical concentration there is a significant change. An average overall decrease of ~20% was observed in the coefficient of friction for the silica-GNP (5 vol%) composite (0.56 ± 0.1) compared to that of pure silica at the 500 m sliding distance using alumina balls. Although by the end of the test coefficients of friction values are very similar for both the pure silica and silica-GNP composite samples.

The coefficient of friction of the silica-GNP (5 vol%) composite (0.65 ± 0.05) tested using BS ball as the counterpart was similar to that of pure silica (0.64 ± 0.02). The similarity of the results in this case is attributed to the increased contact area and material removal, which might have compensated the lubricating effect of GNP in the silica matrix.

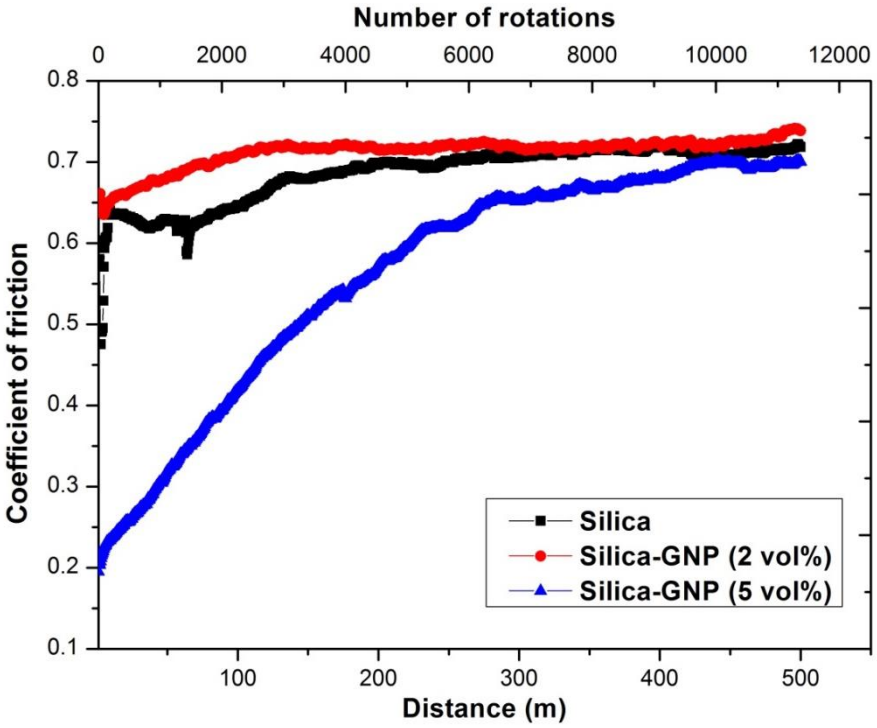

Figure 6.2 Coefficient of friction with respect to sliding distance and number of rotations for silica, silica-GNP (2 and 5 vol%) composites against alumina balls.

Figure 6.3 shows the specific wear rate and normalised wear resistance for the silica-GNP composites with increasing concentration of GNP: **a)** wear properties measured using alumina balls; and **b)** wear properties measured using BS balls. The wear rates were measured at the end of the wear test. The wear resistance of the silica-GNP (2 vol%) composite did not change much compared to pure silica against

the alumina and BS balls. Similar to the coefficient of friction, there was a significant improvement in the wear resistance of the silica-GNP (5 vol%) composite suggesting that the content of GNP plays a critical role in the tribological properties of silica-GNP composites. For both the alumina as well as the BS balls there was a significant drop in the wear rate. Moreover, the comparison between the two different types of balls was very consistent. Since alumina is much harder than the silica composites the wear of the actual balls was much lower (3.1 to 8.7 x 10^{-6} mm^3/N m), leading to a much smaller contact area during the test which results in very low specific wear rate (~10^{-5} to 10^{-6} mm^3/N m) of the silica composites. On the other hand, when borosilicate balls were used (with comparable hardness as silica), the wear of the balls was 2 orders of magnitude higher compared to the alumina balls (1.2 to 7.6 x 10^{-4} mm^3/N m), leading to a much larger contact area, which further results in a significant increase in the wear rate of the silica composites (~10^{-3} mm^3/N m).

The wear resistance of the silica-GNP (5 vol%) composite (7.7 x 10^{-6} mm^3/ N m) increased ~5.5 times compared to pure silica (4.15 x 10^{-5} mm^3/ N m) against alumina balls. The improvement was even more marked against BS balls, with an improvement of ~8.5 times (5.26 x 10^{-4} mm^3/ N m) compared to pure silica (4.29 x 10^{-3} mm^3/ N m). In fact the wear resistance value was comparable to silicon nitride-GNP composites as reported in Ref. [103] with similar test conditions. The dramatic increase in the wear resistance of the nano-composites for high vol% loading can be explained as due to the formation of an interconnected network of GNP inside the silica matrix. The interconnected network of GNP gives a lubricating effect limiting the removal of material from the silica matrix. Also because of the 2D geometry of the GNP and its alignment in the silica matrix, GNP formed a lubricating layer on

the surface of silica limiting the damage during the wear testing. The increased wear resistance of the material was also linked to the improved mechanical properties of silica-GNP composite.

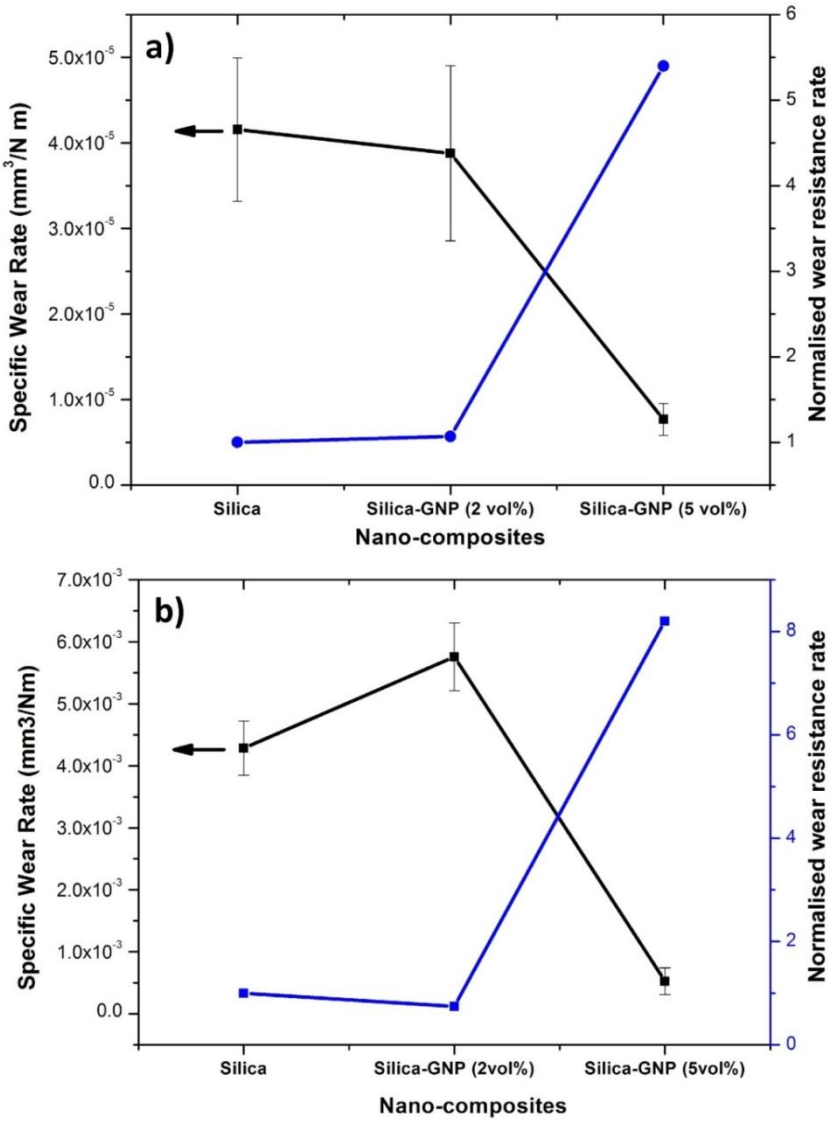

Figure 6.3 Specific and normalised wear rate for silica and silica-GNP (2 and 5 vol%) composites **a)** for alumina balls; and **b)** for BS balls as the counterpart.

Table 6.1 lists the bulk densities, % relative densities, chevron notch fracture toughness, Martens hardness, brittleness index and coefficient of friction values for silica and silica-GNP (2 and 5 vol%) composites tested using both alumina and BS balls as the counterpart. The hardness of the silica-GNP (5 vol%) composite decreased by ~25% while its fracture toughness increased by ~45% compared to the pure silica sample. The decrease in hardness can be attributed to the presence of large weak bonded interfaces of graphene planes in the silica matrix. The improvement in the fracture toughness can be attributed to various toughening mechanisms including crack bridging, crack branching, crack deflection and GNP pullout. The main toughening mechanisms observed were crack deflection and crack branching. Mismatch of the coefficient of thermal expansion between silica and GNP generated residual stresses in the silica matrix. These residual stresses result in crack deflection making the silica nano-composites tougher. Also the presence of GNP in a silica matrix made it difficult for the cracks to propagate and thus cracks had to move around the GNP resulting in crack branching. Detailed information about these toughening mechanisms is provided in **chapter 5**. The addition of GNP increases the toughness and decreases the hardness of silica-GNP nano-composites, which decreases the brittleness index of the material by ~50%. It has been shown [161] that the brittleness index, combining both material responses (ratio between hardness and fracture toughness of the material), is a better parameter for the quantification of wear resistance than hardness or fracture toughness taken separately. The decrease in the brittleness index makes the surface of silica-GNP composites less rough and less brittle compared to pure silica. Less brittle and tougher silica composites do not produce much wear of the hard alumina and BS balls resulting in a less rough surface of the counterpart balls compared to pure silica. This, results in less material

removal from silica-GNP composites compared to pure silica. This was experimentally observed by analysing the surface of the balls at the end of the tribology test using an optical microscope. Therefore, the wear resistance of the material increases with decreasing brittleness index.

Table 6.1 Bulk, % relative densities and mechanical, tribological properties of silica and silica-GNP (2 and 5 vol%) composites.

Sample	**Bulk Density (g/cm^3)**	**% Relative Density**	**Martens Hardness (HM) (GPa)**	**Chevron Notch K_{IC} ($MPa\ m^{1/2}$)**	**Brittleness Index ($\mu m^{-1/2}$)**	**Friction Coefficient Alumina Balls**	**Friction Coefficient BS Balls**
SiO_2	2.195	99.8	3.51 ± 0.14	0.67 ± 0.08	5.24	0.69 ± 0.04	0.64 ± 0.02
SiO_2 + GNP (2 vol%)	2.184	99.3	2.91 ± 0.5	0.79 ± 0.07	3.68	0.71 ± 0.02	0.67 ± 0.02
SiO_2 + GNP (5 vol%)	2.2	100	2.63 ± 0.2	0.96 ± 0.08	2.74	0.56 ± 0.1	0.65 ± 0.05

In order to understand in more detail the mechanism of wear resistance, wear tracks for both the silica and silica-GNP composites were investigated using SEM. **Figure 6.4** shows SEM images of wear tracks of silica and silica-GNP (5 vol%) composites for both alumina and BS balls as the counterpart. **Figure 6.4 a)** low and **b)** high magnification images of pure silica. It is clear from the images that the surface of the wear track for pure silica was very rough. Also the width of the wear track was measured to be 887 μm **(figure 6.4 (a))**. **Figure 6.4 c)** low and **d)** high magnification images for silica-GNP (5 vol%) composite. Micro-fracture along with wear debris was observed as the main wear mechanism for all of the materials studied. The addition of GNP into the silica based materials results in a higher amount of "islands" of the coherent tribofilm (created by removal and consequently adhesion of the wear debris). These "islands" of coherent film layer can provide some protection to the glass surfaces and decrease the wear coefficient of the materials. The highest amount of such a coherent film was observed in the case of silica composites with 5 vol% of GNP, which explains why this material had the lowest coefficient of friction. Similarly, the smallest amount of wear debris was observed for the silica-GNP (5 vol%) composite. Therefore, the surface for the wear track of the nano-composite was much smoother than that of pure silica confirming the lubricating effect of GNP. Also, the exfoliation of the nanoplatelets generates graphene flakes, which become part of an adhered lubricating tribofilm that effectively limits the wear volume. Therefore, it is believed that the wear behaviour of silica-GNP composites is controlled by the continuous supply of exfoliated graphene flakes that creates a lubricating tribofilm well adhered to the surface, leading to the improved wear resistance of the composite materials. This was also confirmed by Raman spectroscopy.

It should be noted that in **figure 6.4 (a-d)**, the central area of the wear track is deeper as it follows the shape of the sliding sphere. The SEM contrast in **figure 6.4 a)** evidences a deeper zone with more obvious damage (light grey area), the nearby dark grey area might have been generated as a result of the secondary damage (induced damage). Compared to pure silica, silica-GNP (5 vol%) composite had a reduced wear rate because of: 1) decreased friction and; 2) higher damage tolerant property of the nano-composites, also confirmed by the reduced secondary damaged area **(figure 6.4 (c))**. The width of the wear track for silica-GNP (5 vol%) composite (603 µm) was ~35% less compared to pure silica (887 µm). The width of the wear track is directly proportional to the amount of material removed during tribology testing. Since, silica-GNP composite had increased wear resistance; the width of the wear track was much smaller for nano-composite compared to pure silica. This kind of wear behaviour is new and has not been reported in literature for silica-GNP composites. So far, limited improvement of wear resistance (~60%) has been reported in literature for polycrystalline matrix-GNP composite [103]. While we report an improvement of ~5.5 times in wear resistance for amorphous matrix composites. This may suggest GNP can be more effective for improvement in wear properties of the amorphous matrix composites compared to polycrystalline ones.

According to SEM analysis of silica based composites tested using the BS balls, a coherent film providing the lubricating effect was not observed. As mentioned above, it is believed that the increased contact area (due to the higher specific wear rate of the BS balls acting as a counterpart) caused severe wear of the silica based composites producing a large amount of the wear debris, which might have compensated the lubricating effect of GNP in the silica matrix. **Figure 6.4 e)** and; **f)** are the high magnification images of the wear tracks, showing the surface

roughness for pure silica and silica-GNP (5 vol%) composite, respectively, tested using BS balls as the counterpart. Interestingly the surface of silica-GNP (5 vol%) composite was less rough compared to pure silica. Although, there was not much effect on the coefficient of friction, there was a significant reduction in the width of the wear track. Similar to alumina samples, the width of the wear track decreased ~30% for silica-GNP (5 vol%) composite (1260 μm) compared to pure silica (1800 μm) confirming the improvement in the wear resistance of the material.

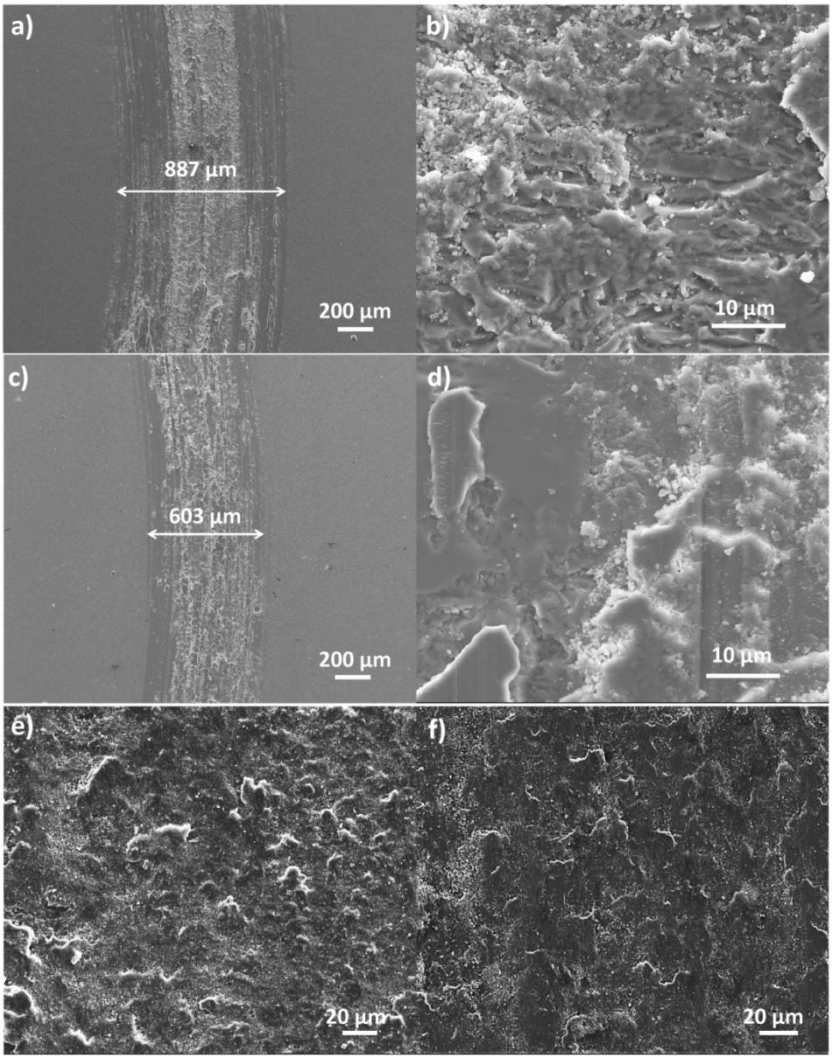

Figure 6.4 SEM images of wear tracks for silica-GNP composites: **a)** low and **b)** high magnification images showing width of the wear track, surface roughness for pure silica; **c)** low and **d)** high magnification images of silica-GNP (5 vol%) composite using alumina balls as the counterpart; **e)** and; **f)** high magnification images showing surface roughness of the wear track for pure silica and silica-GNP (5 vol%) composite respectively using BS balls as the counterpart.

Raman spectroscopy was performed on the as synthesised GNP and silica-GNP (5 vol%) composite (alumina balls) in order to understand the extent of damage to the GNP after tribology testing. **Figure 6.5** shows the comparison of the Raman spectra of GNP and silica-GNP (5 vol%) composite. In the case of silica-GNP (5 vol%) composite two scan areas were chosen: 1) surface without wear damage (outside wear track); and 2) surface with wear damage (inside wear track). At least 3 scans were performed for each sample. Typical peaks were observed at ~1350 cm^{-1} (D band), ~1585 cm^{-1} (G band) and ~2700 cm^{-1} (2D band). Interestingly, there was a negative shift of ~7 cm^{-1} (D band), ~14 cm^{-1} (G band) and ~20 cm^{-1} (2D band) in the peak positions of silica-GNP (5 vol%) composite on the wear damaged surface (inside wear track) compared to the surface without damage (outside wear track). A shift in D, G and 2D peak positions can be attributed to residual tensile strain [162]. This strain might have been induced by the shear stress at the contact point of balls and substrate, while the flexible GNP was anchored to the matrix. Sliding forces increased the shear and tensile stresses on the GNP resulting in its damage. The shift in peak confirms residual tensile strain of the GNP produced by deformation of the GNP. The defected and fragmented GNP becomes part of the wear debris and acts as lubricant during the tribology testing. A decrease in the I_D/I_G ratio was also observed for silica-GNP (5 vol%) composite (I_D/I_G = 0.24) compared to GNP (I_D/I_G = 0.32) suggesting that there was some agglomeration of GNP during processing of the composite resulting in reduced edge defects and hence decreased D peak intensity. The damage of the GNP during the wear testing was also confirmed by evaluating the I_D/I_G ratios of GNP and silica-GNP (5 vol%) composite in the areas with and without wear damage. In the case of Raman scans inside the wear track of silica-GNP (5 vol%) composite an increase in the D peak intensity was observed (I_D/I_G =

0.67). The increased D peak intensity is directly related to the number of edges, and therefore more GNP flakes [41]. Thus the increase in the I_D/I_G ratio inside the wear track of silica-GNP (5 vol%) composite confirmed the formation of exfoliated and fragmented GNP flakes during tribology testing which contributed to the formation of a tribofilm on silica-GNP composites resulting in improved wear properties. Similar behaviour has been observed by other authors for silicon nitride-GNP composites [105]. It should be noted that similar Raman results were observed for silica-GNP composites tested using BS balls as the counterpart.

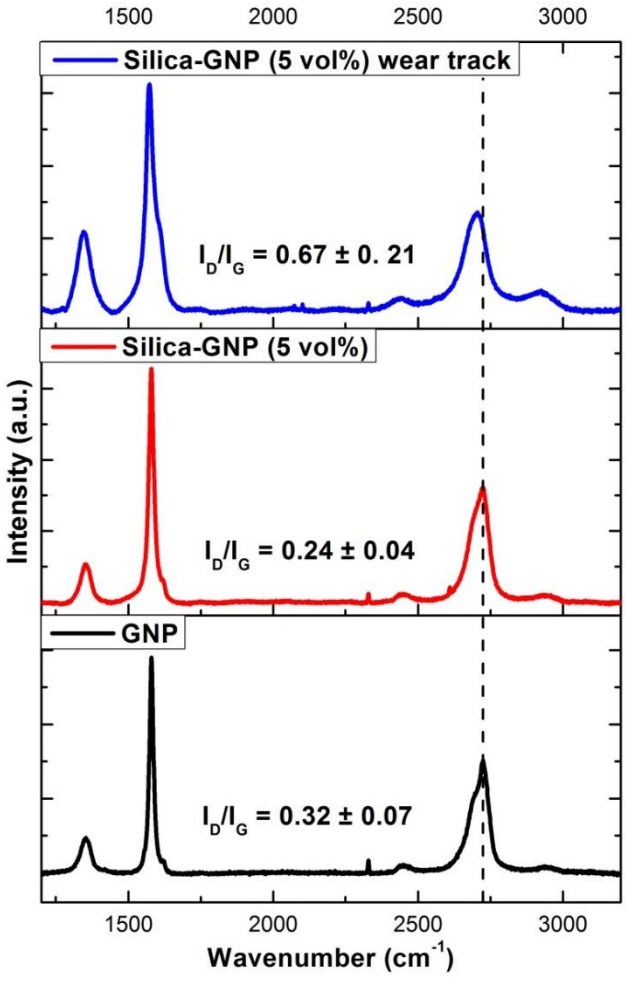

Figure 6.5 Shows the comparison of the Raman scans for GNP and silica-GNP (5 vol%) composite with and without damaged surface (wear track) using alumina balls as the counterpart.

6.4 Conclusion

The tribological properties of silica-GNP composites were investigated for the first time using a ball on disc technique with alumina and BS balls as the tribological counterpart at room temperature. GNP reduced the coefficient of friction of the material by ~20% for silica-GNP composites (alumina balls) while in the case of silica composites tested using BS balls no change was observed. There was an improvement of ~5.5 and ~8.5 times in the wear resistance of the silica-GNP composites tested against alumina and BS balls, respectively. GNP above a critical content formed an interconnecting network, which provided an effective lubricating effect to the silica matrix resulting in improved wear properties. GNP increased the toughness (~45%) and decreased the hardness (~25%), thus decreasing the brittleness index (~50%) of the prepared composites. Interestingly the width of the wear track was also decreased by ~35% and 30% for silica-GNP (5 vol%) composites compared to pure silica, for samples tested using alumina and BS balls respectively. Raman spectroscopy confirmed the GNP was damaged during the tribology tests. The present study suggests that GNP is a good reinforcement for improving the tribological properties of brittle matrices.

Chapter 7 Graphene Nanoplatelet Reinforced Alumina Nano-Composites

7.1 Introduction

Although the reported literature shows that colloidal processing gives better dispersion compared to powder processing, many authors have used powder processing because it is easier and can be scaled up. However, there is considerable scope for optimising the processing to achieve improved dispersion. In the present work, liquid phase exfoliation has been used to produce Al_2O_3-graphene nanoplatelet (GNP) composites. This method enables good dispersion and quality of GNP with control over size and thickness. This processing route solves the problem of producing good quality GNP without affecting its properties, as in the case of Hummer's method. Well dispersed Al_2O_3-GNP powder mixtures were produced using simple sonication and ball-milling. SPS was used for the consolidation process to preserve the integrity of GNP from structural defects by minimising the processing times at high temperature [70]. The aim of this work was to develop a processing route to produce directly well dispersed and dense ceramic-GNP composites, with minimal damage to the GNP. Then to evaluate the influence of GNP on the fracture behaviour of the composites.

7.2 Experimental Section

GNP were prepared using a liquid phase exfoliation method. Details about the preparation of GNP are provided in **chapter 3**. Alumina-GNP composites with GNP loading of 0.2, 0.5, 0.8, 2 and 5 vol% were prepared using a powder processing method and sintered using SPS. Details about the processing and sintering conditions of the alumina nanocomposites are provided in **chapter 3**. The microstructure of the prepared composites was investigated using XRD, Raman and SEM. The prepared composites were characterised for mechanical properties. The details about the mechanical testing are provided in **chapter 3**. The nanocomposites were characterised for chevron notch fracture toughness, indentation toughness and hardness, elastic modulus and grain size analysis.

7.3 Results and Discussion

The main advantages of using SPS over conventional sintering techniques is that the sintering time can be reduced from several hours to just a few minutes because of the high heating rates involved (up to ~600 ^{o}C/min) and simultaneous application of pressure/electric field. Fully dense composites were obtained with a dwell time of 5 minutes, thus limiting the GNP damage induced by prolonged exposure at high temperature as in the case of hot pressing/pressure-less sintering. **Figure 7.1** shows shrinkage rate, pressure and temperature profiles for the pure alumina. There appeared to be no change in the sintering behaviour of alumina with the addition of GNP. This is different to what has been reported in the case of Al_2O_3-

CNTs composites, where CNTs (>2% vol) promoted low temperature sintering [9, 78, 79].

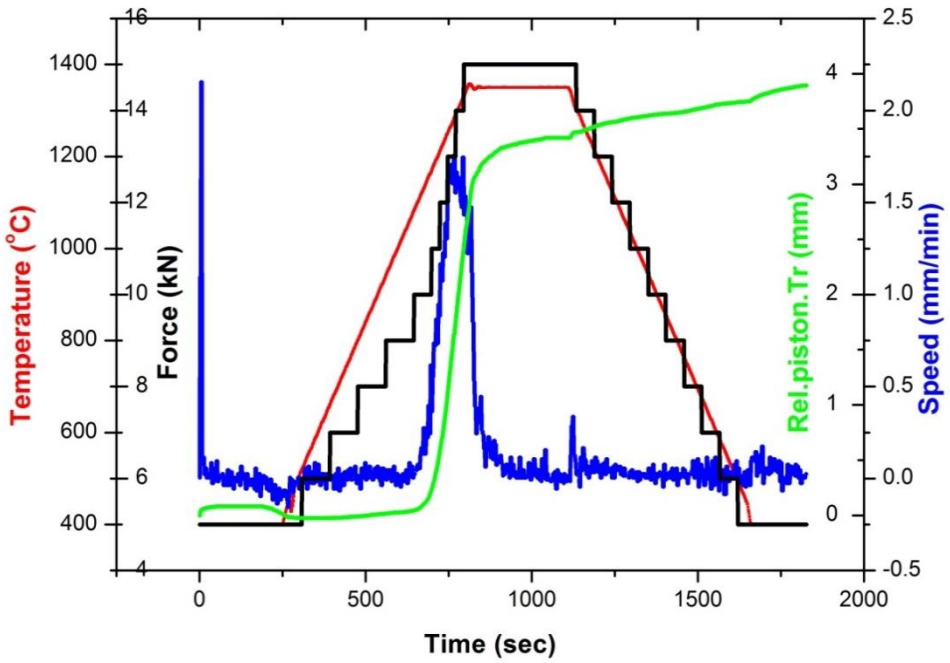

Figure 7.1 Sintering profile of pure alumina showing temperature (red curve) and pressure (black curve) profiles, shrinkage rate (blue curve) and relative piston travel (green curve).

It should be noted that no agglomerates of GNP were found in samples with concentration ≤2 vol%, thus, confirming the good quality of the GNP dispersion. Another advantage of using GNP prepared by liquid phase exfoliation is that there is no need to reduce graphene oxide nanoplatelet (GONP) to GNP, making these composites easier to process and avoiding un-wanted damage to GNP due to oxidation.

Table 7.1 shows the bulk and theoretical densities of the prepared composites along with their sintering conditions. The XRD data shows that with increasing volume fraction of GNP, a new peak is observed at 26.3^{o} which

corresponds to crystalline carbon **(Figure (7.2a))** [142]. There is no detectable second phase indicating that there was no significant reaction between GNP and alumina. Raman spectroscopy was used to confirm the structural integrity of the GNP in the alumina matrix after sintering **(Figure (7.2b)).** Three clear peak at ~1317 cm^{-1} (D band), ~1585 cm^{-1} (G band) and ~2600 cm^{-1} (2D band) were observed for all samples including graphite, graphene and Al_2O_3-GNP nano-composites [130]. The intensities of the D and G Raman peaks were compared for all samples. As expected graphite showed the lowest I_D/I_G ratio of 0.22. After exfoliation, the intensity of the D peak increased due to an increased number of edge defects produced during high energy processing of the graphene suspension (I_D/I_G of 0.68). I_D/I_G values of 0.78, 0.59 and 0.5 were observed for Al_2O_3-GNP 0.5, 2 and 5 vol% samples respectively. The slight increase in I_D/I_G ratio for the 0.5 vol% sample suggests that the GNP was further damaged during high temperature processing. Interestingly, the I_D/I_G ratio for Al_2O_3-GNP composites decreased with increasing concentration of GNP. In the case of liquid phase exfoliated graphene, the intensity of the D peak is dominated by the number of edge defects and can also be related to size of the graphene flakes [41]. As the number of graphene flakes increased the intensity of the D peak also increased. In case of Al_2O_3-GNP composites, as the concentration of graphene increased in the alumina matrix, overlapping of graphene flakes was observed (also confirmed by SEM). The overlapping of graphene flakes leads to less number of edges and thus decreasing I_D/I_G ratio for Al_2O_3-GNP composites with high concentration of GNP.

Table 7.1 Bulk and theoretical densities of prepared composites along with sintering conditions.

Sample	**Sintering Conditions**	**Bulk Density**	**% Theoretical Density**
Al_2O_3 Pure	1350 ^oC/50 MPa/5 min	3.98	99.8
Al_2O_3 + 0.2 vol% GNP	1350 ^oC /50 MPa/5 min	3.97	99.9
Al_2O_3 + 0.5 vol% GNP	1350 ^oC /50 MPa/5 min	3.97	99.0
Al_2O_3 + 0.8 vol% GNP	1350 ^oC /50 MPa/5 min	3.96	99.9
Al_2O_3 + 2 vol% GNP	1350 ^oC /50 MPa/5 min	3.94	98.9
Al_2O_3 + 5 vol% GNP	1350 ^oC /50 MPa/5 min	3.89	99.0

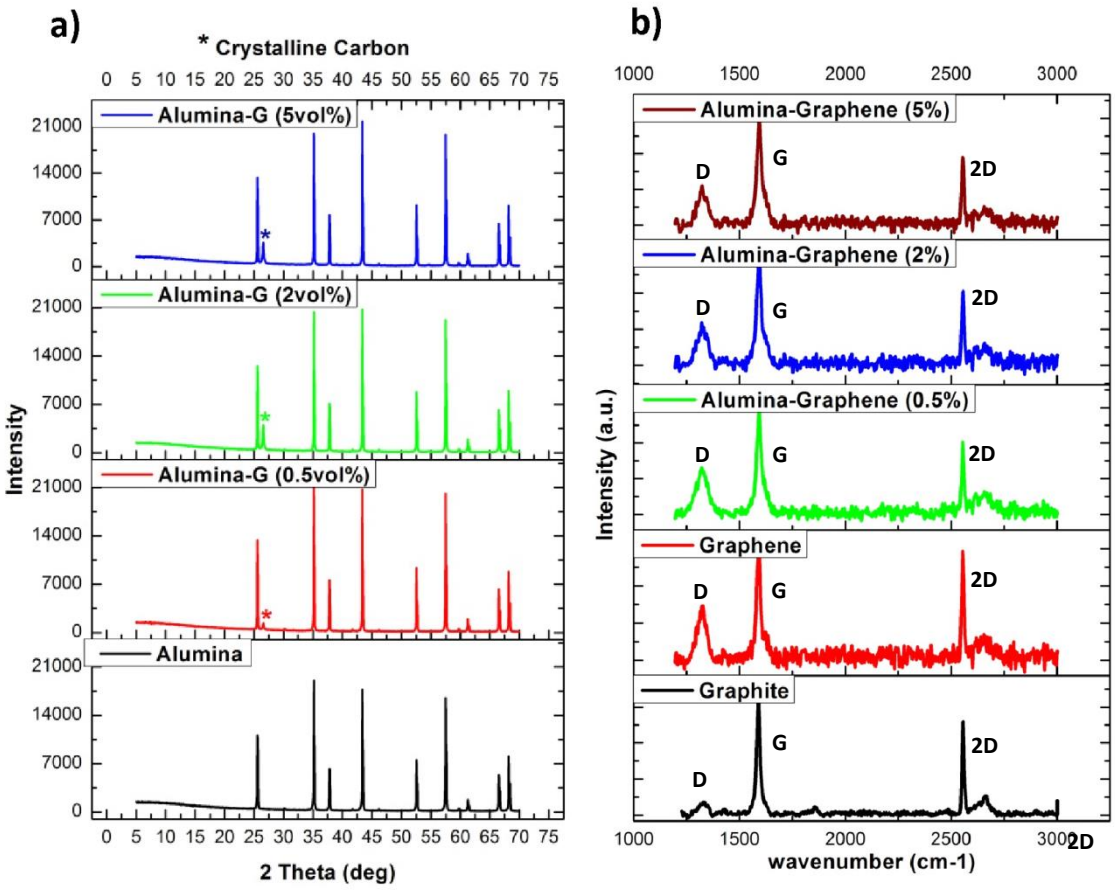

Figure 7.2 a) XRD patterns for pure alumina and alumina-GNP composites showing crystalline carbon peak at 26.3^{o} and; **b)** Raman spectra of graphite, graphene and alumina-GNP nano-composites showing typical D, G and 2D peaks.

In order to investigate the effect of GNP concentration on the fracture toughness of alumina ceramics, we used both chevron notch fracture toughness (standard method) and micro indentation fracture toughness method (common method) to measure the toughness of the prepared composites as shown in **Figure 7.3**. It should be noted that although micro indentation fracture toughness has advantages, like only small specimens are required for testing, it does not provide correct engineering values of fracture toughness. In the case of CNT composites

there can be a large discrepancy between the two methods [98]. A comparison of the results of the two methods has not previously been reported for ceramic graphene nano-composites. Therefore we used both methods to calculate the toughness of our materials to enable a comparative study of the toughness values obtained.

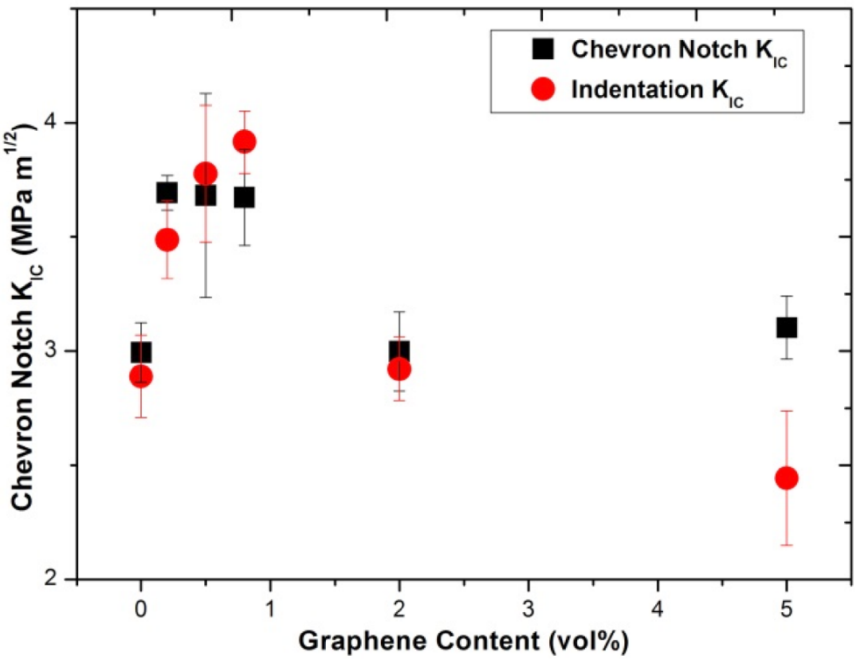

Figure 7.3 Fracture toughness of the alumina-GNP nano-composites with different vol% loading of GNP measured with both chevron notch and indentation fracture toughness method.

Similar toughness values of 2.9 and 2.8 MPa were obtained for pure alumina with chevron notch and indentation fracture toughness methods respectively. The micro indentation fracture toughness values increased with increasing vol% loading of GNP and reached a maximum value of 3.9 MPa for the 0.8 vol% composite, corresponding to an increase of ~40% compared to pure alumina. This value was slightly higher than, but within the error bars, the value obtained with the chevron

notch fracture toughness method. The toughness values decreased for GNP loading higher than 1 vol% and reached a value of 2.4 MPa for indentation and 3.1 MPa for chevron notch for the 5 vol% composite.

It should be noted that the fracture toughness values obtained by both chevron notch and indentation method differ only for the 5 vol% composite. As the concentration of GNP increases, it leads to the formation of an inter-connected graphene network that acts as a weak interface, and because the indentation method measures the toughness values locally it gives artificially lower values for the 5 vol% composite, suggesting that the indentation method is not a reliable tool for measuring the fracture toughness of high vol% samples.

7.3.1 Reinforcement Mechanism

To investigate the fracture behaviour of the composites, the fractured surfaces of the chevron notch fracture toughness samples were studied. **Figure 7.4** shows SEM images of chevron notch fractured surfaces for Al_2O_3-GNP nano-composites. **Figure 7.4 (a)** shows the grain microstructure of fully dense pure α-alumina. The main mechanism of crack propagation for pure alumina is inter-granular as the cracks only propagates through grain boundaries. **Figure 7.4 (b)** shows the trapping of GNP in between grain boundaries and protruding from the fracture surface for the 0.5 vol% Al_2O_3-GNP composite. **Figure 7.4 (c)** is a high magnification image showing a change in mechanism of crack propagation to trans-granular with the increasing concentration of GNP (2 vol%). Generally in ceramic matrix composites, cracks propagate through the grain boundaries if they are weaker than the grains. It should be noted that in the case of Pure Al_2O_3 the mechanism of crack propagation was dominated by an inter-granular mechanism but with

increasing concentration of GNP in Al_2O_3-GNP composites a trans-granular mechanism of crack propagation became more dominant. **Figure 7.4 (d)** SEM image of 5 vol% Al_2O_3-GNP composite showing graphene pull out from the fractured surface.

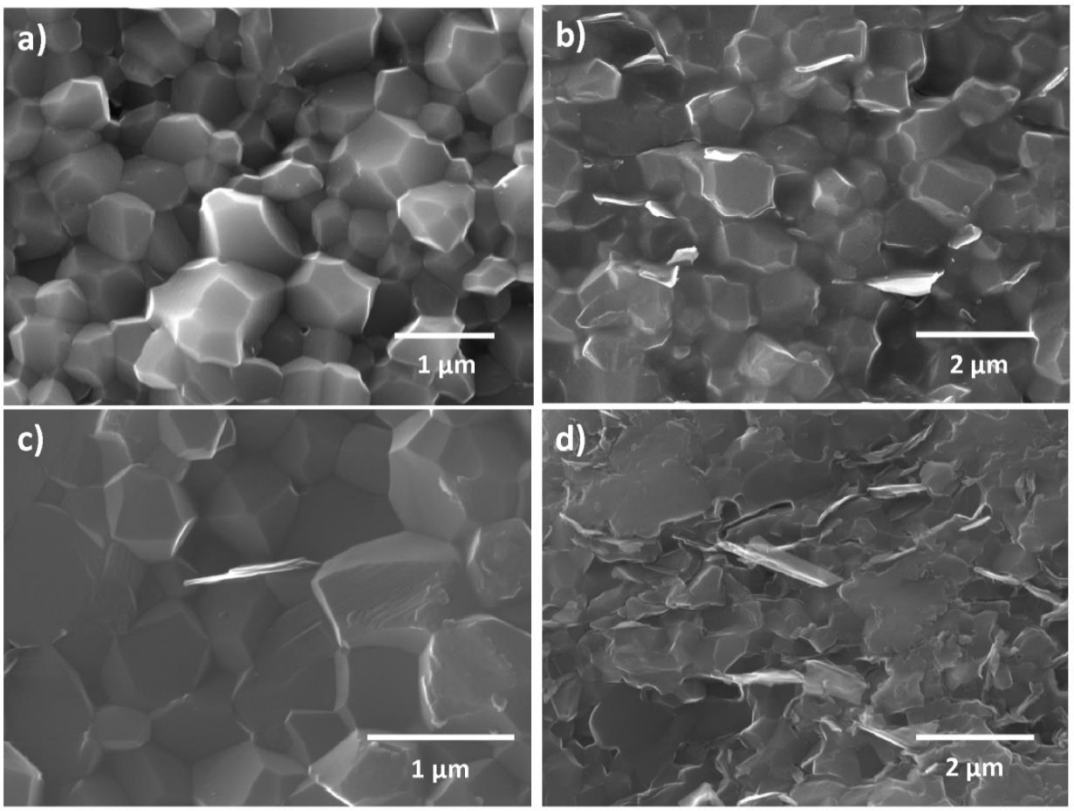

Figure 7.4 Shows SEM images of chevron notch fractured surfaces for Al_2O_3-GNP nano-composites: **a)** grain microstructure of fully dense pure α-alumina; **b)** low magnification image of 0.5vol% Al_2O_3-GNP sample showing graphene pull out; **c)** high magnification image of 2vol% Al_2O_3-GNP sample, showing change in mechanism of crack propagation from inter-granular to trans- inter-granular with the addition of GNP; **d)** 5vol% Al_2O_3-GNP sample showing graphene pull out from alumina matrix.

In order to study in more detail about the toughening mechanisms in graphene composites, the fracture patterns generated by Vickers indentation were analysed. **Figure 7.5** shows SEM images of Vickers indentation fractured surfaces for Al_2O_3 and Al_2O_3-GNP composites. **Figure 7.5 (a)** shows a straight crack path for pure Al_2O_3. **Figure 7.5 (b)** shows a deflected crack path for Al_2O_3-GNP (0.5 vol%) composite, with an arrow highlighting crack bridging. **Figure 7.5 (c)** shows crack bridging and grain pullout toughening mechanisms (highlighted with arrows) for Al_2O_3-GNP (2 vol%) composite. **Figure 7.5 (d)** shows crack branching in the Al_2O_3-GNP (0.5 vol%) composite. In reinforced ceramics which fracture by the growth of a single dominant flaw, the toughness of the material is mainly influenced by four effects [163]: 1) Debonding which generates new surfaces; 2) frictional dissipation upon pullout; 3) matrix cracking which relieves residual stresses; and 4) nano-fibre failure. All these factors contribute positively to the toughness of a composite and were observed for GNP reinforced Al_2O_3 nano-composite.

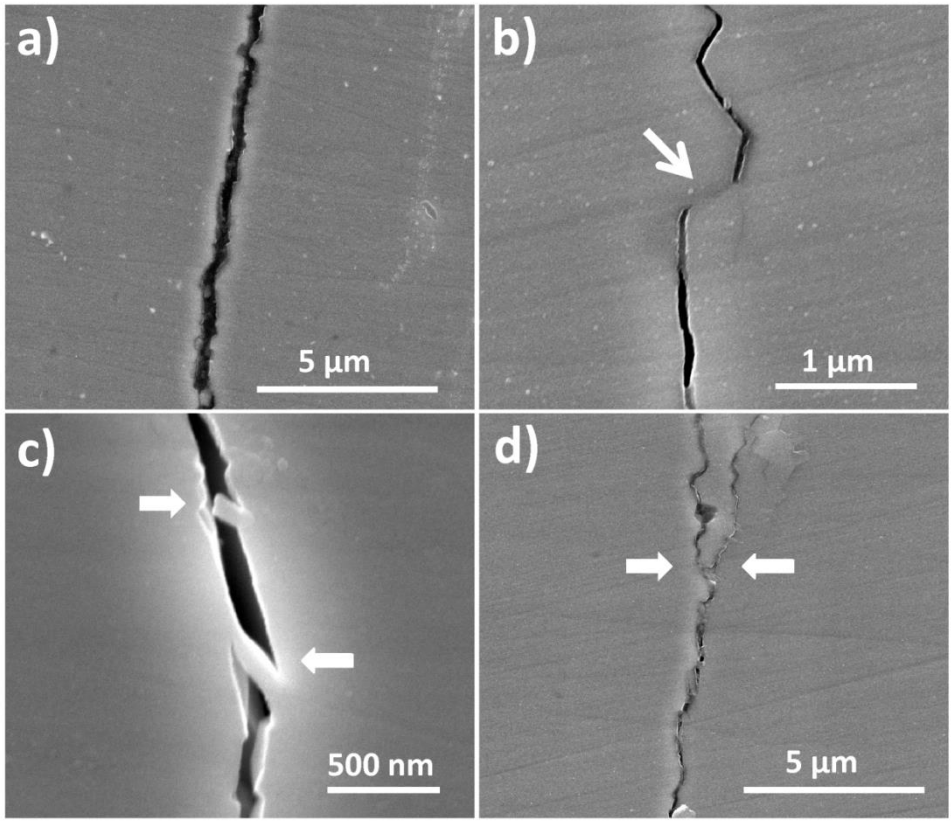

Figure 7.5 SEM images of Vickers indentation crack for Al_2O_3-GNP composites: a) shows straight crack path for pure Al_2O_3; b) crack deflection and crack bridging toughening mechanisms for Al_2O_3- GNP (0.5 vol%) composite; c) shows crack bridging and pullout for Al_2O_3- GNP (2 vol%) composite; and d) crack branching toughening mechanism for Al_2O_3-GNP (0.5 vol%) composite.

It should be noted that graphene seen in fractured surfaces looked thicker than the graphene produced using the liquid phase exfoliation method. There was overlapping of graphene flakes during the processing of the Al_2O_3-GNP powder mixtures which was verified by comparison of the I_D/I_G ratios in Raman spectroscopy. Similar phenomena have also been reported by other authors [107, 164]. There was preferential orientation of the GNP in the alumina matrix in the

plane perpendicular to the pressure direction during sintering **(Figure 7.6)**. This alignment of GNP can also enhance the toughness of the materials in the direction perpendicular to the alignment and produce anisotropic properties in the composites. Anisotropy has also been reported for Si_3N_4-graphene composites for various properties including elastic modulus [165], electrical [108] and thermal [113] conductivities. The anisotropy in the case of graphene nano-composites can be explained due to the 2D geometry of the graphene flakes which aligns during sintering with applied pressure in the ceramic matrix.

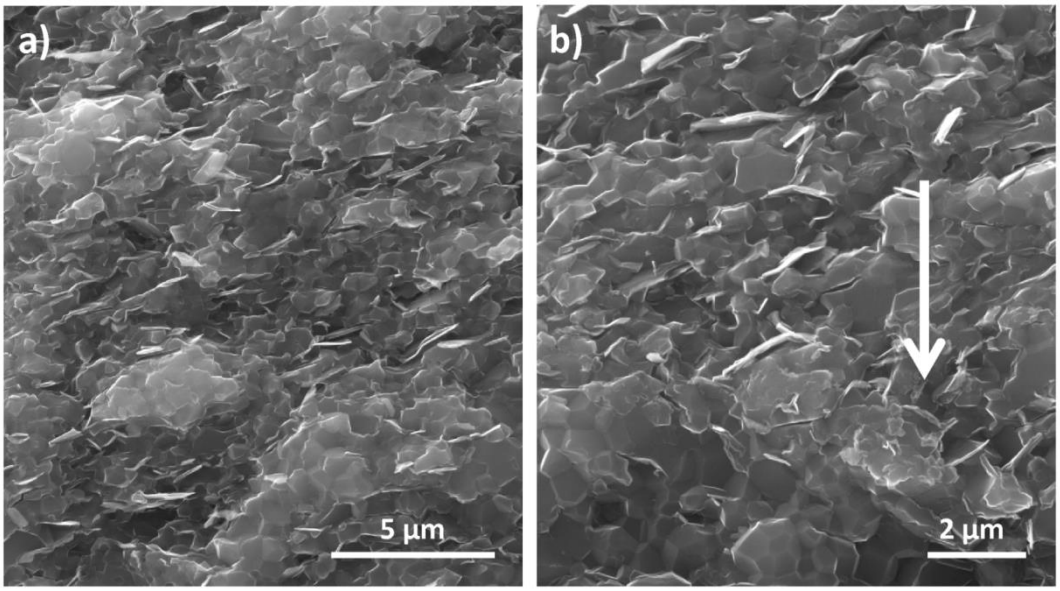

Figure 7.6 SEM fractured surface images of Al_2O_3-GNP (5 vol%) nano-composites: **a)** Increase in number of contacted GNP site with increasing concentration of GNP; **b)** alignment of graphene in alumina matrix after SPS processing with arrow showing the pressing direction.

Table 7.2 summarizes the chevron notch toughness, micro indentation toughness, grain size, micro indentation hardness and elastic modulus values for all the Al_2O_3-GNP nano composites. There is no significant difference in the grain size of the materials **(Figure 7.7)**. The hardness is similar for all of the composites. The elastic modulus of the composites does not change up to 2 vol% loading and decreases by ~15% for the 5 vol% composite. A similar trend is observed for the toughness values measured using micro-indentation and chevron notch method. The sudden decrease in mechanical properties (K_{IC} and elastic modulus) above 2 vol% GNP loading can be attributed to the increase in number of sites of inter-connected graphene flakes **(Figure 7.6)** with increasing GNP content. The formation of inter-linked graphene networks effectively produces large defects which are detrimental to the fracture toughness of the composites. The formation of an inter-linked graphene network was also confirmed by elastic modulus measurement where the value for pure alumina decreased from 380 to 328 GPa for the 5 vol% composite.

Table 7.2 Physical and mechanical properties of Al_2O_3-GNP nano-composites.

Sample	**Chevron Notch K_{IC} (MPa $m^{1/2}$)**	**Micro Indentation K_{IC} (MPa $m^{1/2}$)**	**Grain Size (nm)**	**Hardness HV (GPa)**	**E-Modulus (GPa)**
Al_2O_3 Pure	2.9 ± 0.13	2.8 ± 0.17	529 ± 114	22.9 ± 0.70	380
Al_2O_3 + 0.2 vol% GNP	3.7 ± .07	3.5 ± 0.17	-	21.3 ± 0.60	398
Al_2O_3 + 0.5 vol% GNP	3.6 ± 0.44	3.7 ± 0.3	589 ± 86	21.3 ± 1.32	380
Al_2O_3 + 0.8 vol% GNP	3.7 ± 0.21	3.9 ± 0.13	-	21.6 ± 0.55	373
Al_2O_3 + 2 vol% GNP	3.0 ± 0.17	2.9 ± 0.14	520 ± 96	22.1 ± 0.71	372
Al_2O_3 + 5 vol% GNP	3.1 ± 0.13	2.4 ± 0.18	572 ± 108	21.6 ± 0.295	328

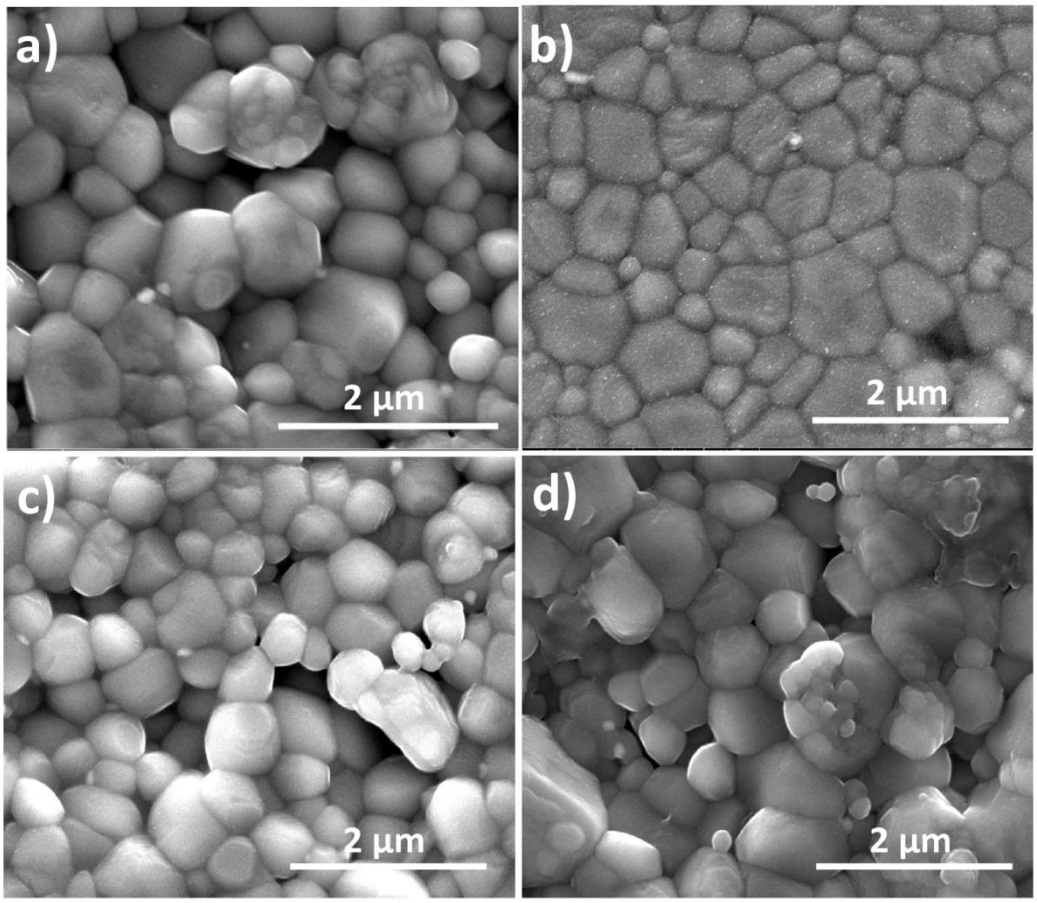

Figure 7.7 SEM images of polished then thermally etched surfaces showing grain size distribution of: **a)** Al_2O_3; **b)** Al_2O_3-GNP (0.5 vol%); **c)** Al_2O_3-GNP (2 vol%) and **d)** Al_2O_3- GNP (5 vol%) composites.

7.4 Conclusion

To summarize, well dispersed suspensions of graphene with average lateral size 1.5 µm and typically three layers thick were prepared using a liquid phase exfoliation method. Well dispersed, fully dense (> 99%) Al_2O_3-graphene composites were prepared by powder processing and densified using SPS at 1350 ^oC with 50 MPa pressure. There was an improvement of ~40% in the fracture toughness of the composites prepared with the addition of only 0.8 vol% GNP as measured by micro indentation and ~25% as measured by chevron notch fracture toughness methods. GNP was found to be anchored in between the grains of alumina and different toughening mechanism were observed including graphene pull out, crack bridging, crack deflection and crack branching. A trans-granular mechanism of crack propagation became more dominant with increasing GNP content. GNP toughens the composites by making the crack paths more tortuous. The change in mechanism of crack propagation is new compared to fibre reinforced ceramic composites and has not been reported in the literature previously for ceramic GNP composites. The fracture toughness and elastic modulus of the nano-composites decreased for composites with ≥ 2 vol% GNP. This is attributed to an increase in number of sites with inter connecting graphene flakes. The present study suggests that a low (< 2 vol%) concentration of GNP is an effective reinforcing agent for alumina ceramics.

Chapter 8 Scratch Behaviour of Graphene Alumina Nanocomposites

8.1 Introduction

In the case of ceramic matrix composites, little attention has been paid to investigating their tribological properties. Lim et al. [166] prepared alumina-CNT (up to 12 wt%) composites and compared the effect of fabrication technique on their tribological behaviour. They suggested that composites made using tape casting followed by hot pressing showed better tribological properties compared to materials produced using hot pressing of powders. This was attributed to the better dispersion of CNTs in the alumina matrix. Ahmad et al. [167] reported a reduction in the coefficient of friction by 80% for alumina-multi walled carbon nanotubes (MWCNTs) composites containing 10 wt% MWCNTs. They suggested MWCNTs affect the tribological properties of alumina composites indirectly by influencing the mechanical properties and directly by acting as a lubricating medium. Hvizdos et al. [168] reported an improvement in the tribological properties of silicon nitride, zirconia and alumina composites with the addition of MWCNTs. In the works reported on GNP composites, Hvizdos et al. [103] and Belmonte et al. [169] reported an improvement of ~60% and 56% respectively in the wear resistance of silicon nitride with the addition of GNP. The research so far has shown promising improvements in tribological properties with the addition of carbon nano-fillers. It

should be noted that there is little reported literature on the scratch resistance of ceramic nano-composites, despite their promising tribological properties. Scratch resistance is an important property in many applications [170-172]. In the present work, the effect of GNP concentration on the scratch resistance of alumina was investigated by fabricating alumina-GNP (0.5, 2 and 5 vol%) composites using SPS. The fabricated composites were tested using single pass scratch testing. The mechanisms for micro damage were investigated with increasing load. Different scratch resistance mechanisms were observed for different composites depending on the loading of GNP.

8.2 Experimental Section

The details about the synthesis, characterisation and scratch testing of GNP and alumina-GNP composites are provided in **chapter 3**.

8.3 Results and Discussion

All of the prepared composites were nearly fully dense (>98%). The microstructural characterisation of the prepared composites using XRD and Raman spectroscopy is reported in **Chapter 7**. **Figure 8.1** are SEM images showing the distribution of GNP in the alumina-GNP (2 and 5 vol%) composites. The GNP (marked with white arrows) were found to be located at the alumina grain boundaries and was uniformly distributed throughout the alumina matrix **(Figure 8.1 (a))**. As the concentration of GNP increased in the alumina matrix there was some overlapping of the GNP around alumina grains, which weakened the grain

boundaries (marked with red arrows **Figure 8.1 (b)**). It should be noted that the GNP prepared using liquid phase exfoliation were thinner compared to the GNP observed in the fractured surfaces, which suggests that there was some overlapping of the GNP during processing. This was also confirmed by Raman spectroscopy **(Chapter 7)**.

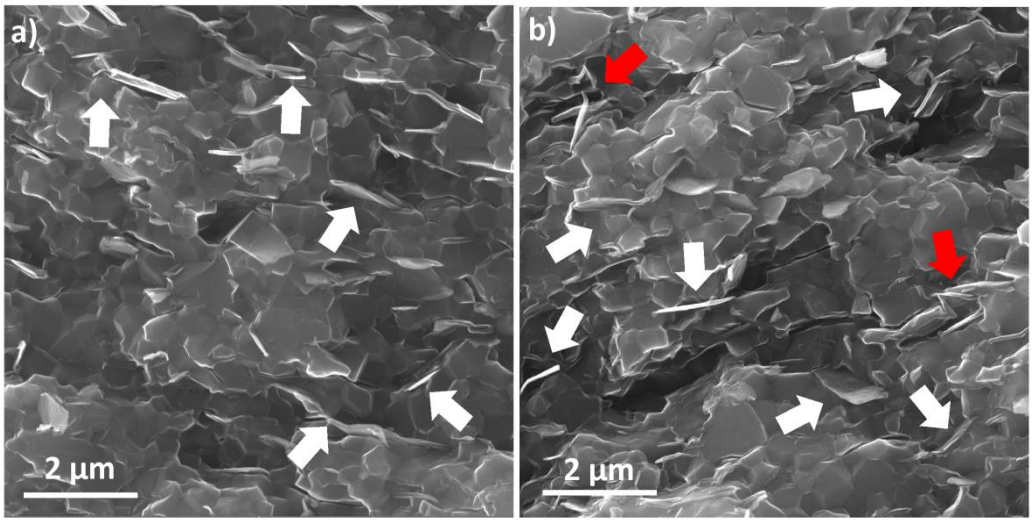

Figure 8.1 SEM images of the fracture surfaces of: **a)** alumina-GNP (2 vol%); and **b)** alumina-GNP (5 vol%) composites showing the distribution of GNP in the alumina matrix.

Figure 8.2 shows the scratch test data recorded for alumina-GNP (5 vol%) composite over a distance of 10 mm with an increasing applied load of 1 to 200 N. The coefficient of friction (COF) and acoustic emission (AE) signals were recorded during the scratch test for all of the samples. The COF increases (red curve) with increasing scratch distance and increasing applied load. The peaks in the AE (black lines) corresponded to cracking and chipping events. The AE signal helped us to identify when (distance and/or load) the first cracks occurred (marked with arrow in

Figure 8.2), it was also directly related to the chipping of the material at higher loads.

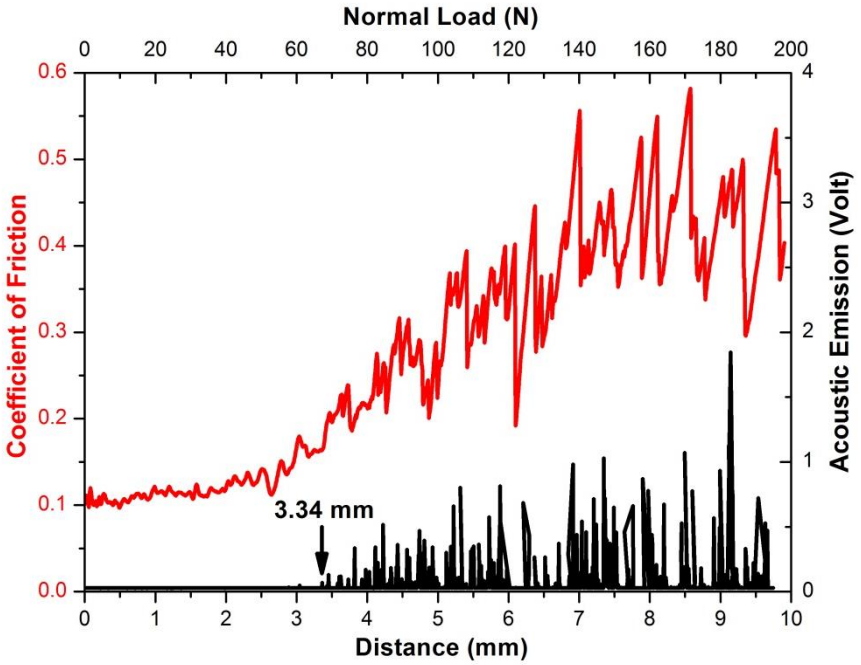

Figure 8.2 Scratch test data recorded for alumina-GNP (5 vol%) composite showing coefficient of friction (red curve) and acoustic emission (black lines) with respect to increasing distance (1-10 mm) and normal applied load (1-200 N).

Figure 8.3 shows the change of the COF values of the alumina-GNP composites with applied normal load and distance. There was no significant change in the COF of the composites compared to pure alumina at low loads (~65 N). As the applied load increased the COF of the composites increased with increasing concentration of GNP. The starting surface roughness of the alumina and alumina-GNP (5 vol%) composite was ~55 and ~92 nm respectively which increased to ~1.93 µm for pure alumina and ~8.9 µm for alumina-GNP (5 vol%) composite after the scratch test. The increased COF at high loads can be attributed to more chipping and increased surface roughness **(Table 1)** of alumina-GNP composites. The average

COF of the alumina-GNP (5 vol%) composite was ~60% higher compared to the pure alumina sample. Interestingly, the COF values for pure alumina and alumina-GNP (0.5 vol%) composite were very similar up to a load of 150 N because, suggesting that the roughness of the scratch grooves of alumina-GNP (0.5 vol%) composite was less compared to alumina-GNP composites with high GNP loading **(Table 1)**.

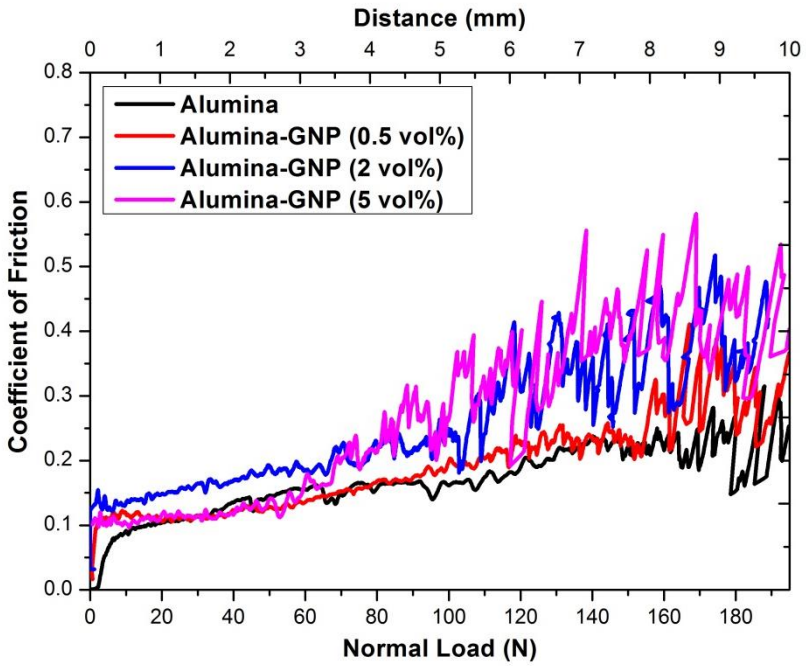

Figure 8.3 COF values with respect to normal load and distance for pure alumina and alumina-GNP composites with different GNP contents.

Figure 8.4 shows confocal microscopy images of scratch grooves obtained after scratch testing the alumina and alumina-GNP (0.5, 2 and 5 vol%) composites. The scratch grooves obtained for various materials are mainly divided into three regions. Region 1 corresponds to so-called *micro-ductile* behaviour at low loading, where the scratch test did not generate any cracks and the material deformed only in a plastic manner **(marked by black lines in figure 8.4)**. The *micro-ductile* region

can be considered as the region before cracking is initiated. As the load increases with scratching distance radial micro cracks start to form around the scratch grooves, corresponding to *micro-cracking* region (Region 2) **(marked by red line in figure 8.4)**. When the load is increased further, sub surface lateral cracking leads to chipping, corresponding to *chipping* region (Region 3) **(dark region in figure 8.4)**. The critical load corresponding to the start of the formation of the radial cracks and chipping are defined as Lc1 and Lc2, respectively.

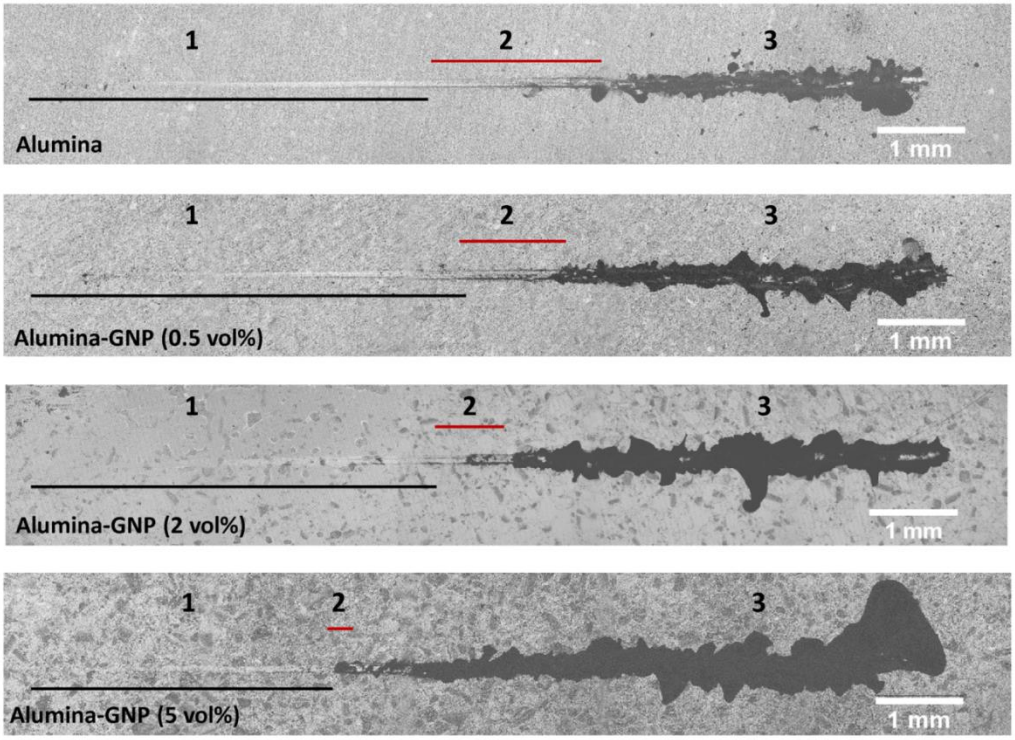

Figure 8.4 Confocal microscopy images showing the scratch damage generated on the polished surfaces of composites containing different vol% loading of GNP.

The mechanical properties and toughening mechanism of alumina-GNP composites are discussed in detail in **Chapter 7**. It has been shown that brittleness index is a better parameter for quantifying the wear properties of the materials

compared to hardness and fracture toughness taken separately [161]. **Table 8.1** summarizes the brittleness index and scratch resistance response for pure alumina and alumina-GNP composites. The brittleness index of alumina-GNP (0.5 vol%) composite was ~30% lower compared to pure alumina sample which was mainly due to the improved fracture toughness of the material. The hardness and chevron notch fracture toughness of alumina-GNP (2 vol%) composites did not change much, therefore no significant change in the brittleness index was observed for the composite. As the concentration of GNP (5 vol%) increased in alumina matrix indentation fracture toughness of the composite decreased by ~15% resulting in ~10% increase in the brittleness index of the material. It should be noted that indentation fracture toughness values are considered in the present work compared to chevron notch fracture toughness because scratch resistance is a surface property and the indentation method measures the toughness values on the surface of the material which is more appropriate in this case. The lengths of the Regions 1, 2 and 3 during the scratch tests were analysed using AE signal, and SEM and confocal microscopy. The data obtained using all of these techniques were in good accordance with each other. The average COF of the composites increased with increasing concentration of GNP in the alumina matrix.

As seen in **figure 8.4,** the length of Region 1 for pure alumina was 4.5 mm. The first radial cracks were observed, which is in good correlation with AE signal (4.25 mm). The Region 1 length increased to 4.9 mm for alumina-GNP (0.5 vol%) composite. This was mainly because of the improved fracture toughness (~35%) and decreased brittleness index of the alumina-GNP (0.5 vol%) composite. The increase in toughness can be attributed to various toughening mechanism including crack bridging, crack branching, crack deflection and GNP pull out **(Chapter 7)**. No

significant change in the length of the Region 1 was observed for the alumina-GNP (2 vol%) composite compared to pure alumina, corresponding to similar brittleness index and elastic modulus values of alumina and alumina-GNP (2 vol%) composite. When the concentration of GNP was further increased there was a significant change in the length of the Region 1. First small chipping in the case of alumina-GNP (5 vol%) composite was observed at 3.4 mm of the scratch test length. It should be noted that no radial cracks were observed in the case of alumina-GNP (5 vol%) composite. The reason for the decrease in the length of the Region 1 was because of the increased brittleness index of the composite. Also, GNP overlapping at the grain boundaries lead to the formation of weak bonded grain boundaries (WBG) which resulted in decreased elastic modulus (~15%) of the alumina-GNP (5 vol%) composite. Interestingly the Region 2 for all the composites decreased in length with increasing concentration of GNP in the alumina matrix. Chipping in GNP composites started earlier compared to pure alumina sample. Since the decrease in the length of the Region 2 was directly related to GNP concentration it is believed that addition of high concentration of GNP resulted in the formation WBG in the alumina matrix. Also since GNP has high aspect ratio and the GNP are bonded by the weak Van der Waals forces there are weak bonded interfaces inside multi-layered platelet which might also contribute to the formation of WBG in the composites. High loads during the scratch test, because of the presence of WBG in alumina-GNP composites, produced more extensive chipping compared to pure alumina which does not contain any weak bonded alumina grains. The observation suggests that at low concentrations GNP (0.5% vol) is beneficial for improving the scratch resistance of alumina-GNP composites for low loads. While high loads resulted in poor scratch resistance for all the composites. Pure alumina was more resistant to chipping

compared to alumina-GNP composites. There was a significant increase in the length of the Region 3 with increasing concentration of GNP for all the composites as can be seen in **figure 8.4**.

Table 8.1 Scratch resistance data for alumina-GNP composites.

Sample	**Brittleness Index ($\mu m^{-1/2}$)**	**Surface Roughness (Before Scratch Test) (nm)**	**Surface Roughness (After Scratch Test) (µm)**	**Average COF**	**Micro ductile Region (mm) Region 1**	**Lc 1 (N)**	**Micro-cracking Region (mm) Region 2**	**Lc 2 (N)**
Al_2O_3	8.20	54.9 ± 6.2	1.93 ± 0.04	0.17 ± 0.05	4.5 ± 0.25	89 ± 5	1.91 ± 0.11	126 ± 7
Al_2O_3-GNP (0.5 vol%)	5.76	66.4 ± 7.3	2.23 ± 0.03	0.19 ± 0.07	4.9 ± 0.37	97 ± 7	1.19 ± 0.09	120 ± 9
Al_2O_3-GNP (2 vol%)	7.62	79.2 ± 16.2	2.97 ± 0.04	0.25 ± 0.09	4.6 ± 0.26	92 ± 5	0.78 ± 0.04	107 ± 6
Al_2O_3-GNP (5 vol%)	9.00	92.2 ± 20.4	8.9 ± 0.06	0.27 ± 0.13	3.4 ± 0.56	68 ± 11	0.28 ± 0.04	73 ± 12

Figure 8.5 shows SEM images showing the initiation of cracks at the start of the Region 2 for: **a)** alumina; **b)** alumina-GNP (0.5 vol%); **c)** alumina-GNP (2 vol%) and; **d)** alumina-GNP (5 vol%) composites. As discussed earlier, the Region 1 for alumina-GNP (0.5 vol%) composite was longer in length than for the other materials due to the improved mechanical properties of the composite. Cracks in the case of pure alumina initiated at a load of 89 ± 5 N (Lc1) while in the case of alumina-GNP (0.5 vol%) composites the crack initiation load was 97 ± 7 N (Lc1). Similar to Region 1, no significant difference was observed for the crack initiation loads for alumina and alumina-GNP (2 vol%) composite (Lc1 = 92 ± 5 N). The composite with 5 vol% loading of GNP changed from Region 1 (Lc1 = 68 ± 11 N) to Region 3 (Lc2 = 73 ± 12 N) with a very narrow Region 2. This Region 2 was a bit different compared to the other materials. Instead of radial cracking, only small chipping was observed. A high concentration of GNP led to the formation of WBG in alumina-GNP (5 vol%) composites. The length of Region 3 in the case of alumina-GNP composites increased with increasing concentration of GNP. In fact the value of Lc2 changed from 126 ± 7 to 73 ± 12 N for alumina and alumina-GNP (5 vol%) composite respectively **(Table 8.1)**.

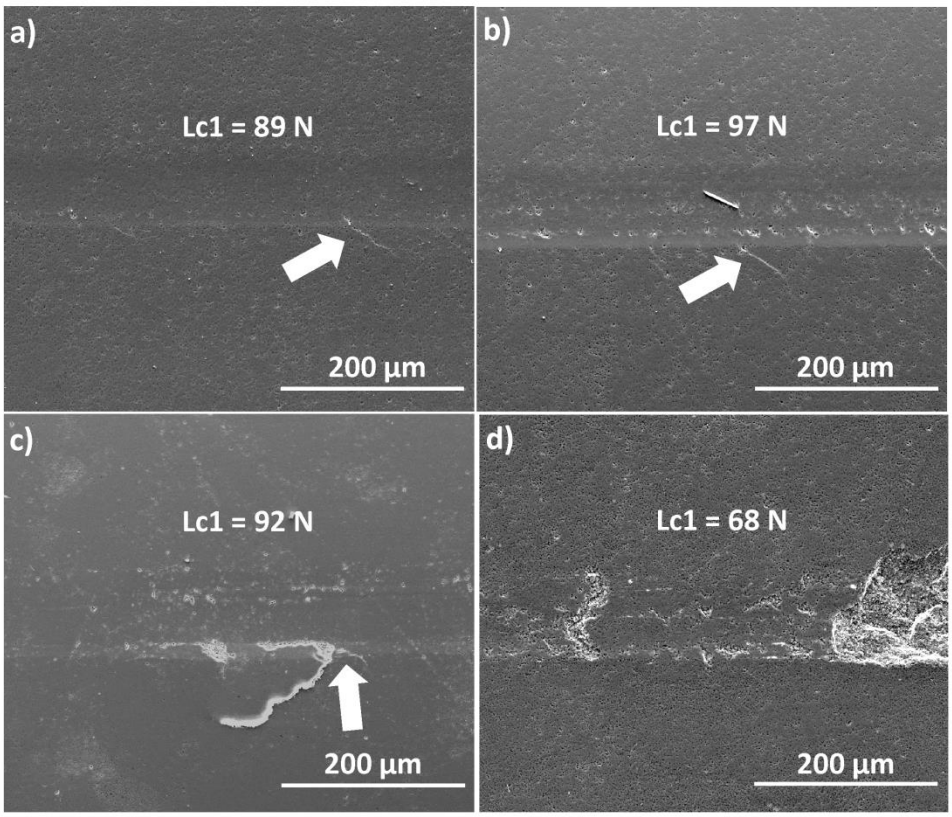

Figure 8.5 SEM images showing the initiation of cracks at the start of region 2 for: **a)** alumina; **b)** alumina-GNP (0.5 vol%); **c)** alumina-GNP (2 vol%) and; **d)** alumina-GNP (5 vol%) composites.

Figures 8.6 shows SEM images of the fractured surfaces in Region 3 of the scratch grooves for: **a)** alumina; **b)** alumina-GNP (0.5 vol%); **c)** alumina-GNP (2 vol%) and; **d)** alumina-GNP (5 vol%) composites. GNP can be seen in the fractured surface after chipping (marked with white arrows). As the concentration of GNP increased in the alumina composites, more GNP and interconnected alumina grains were pulled out at high normal loads, which resulted in an increased surface roughness of the alumina-GNP composites during the scratch testing **(Table 1)**. This can also be related to the increased COF in Region 3.

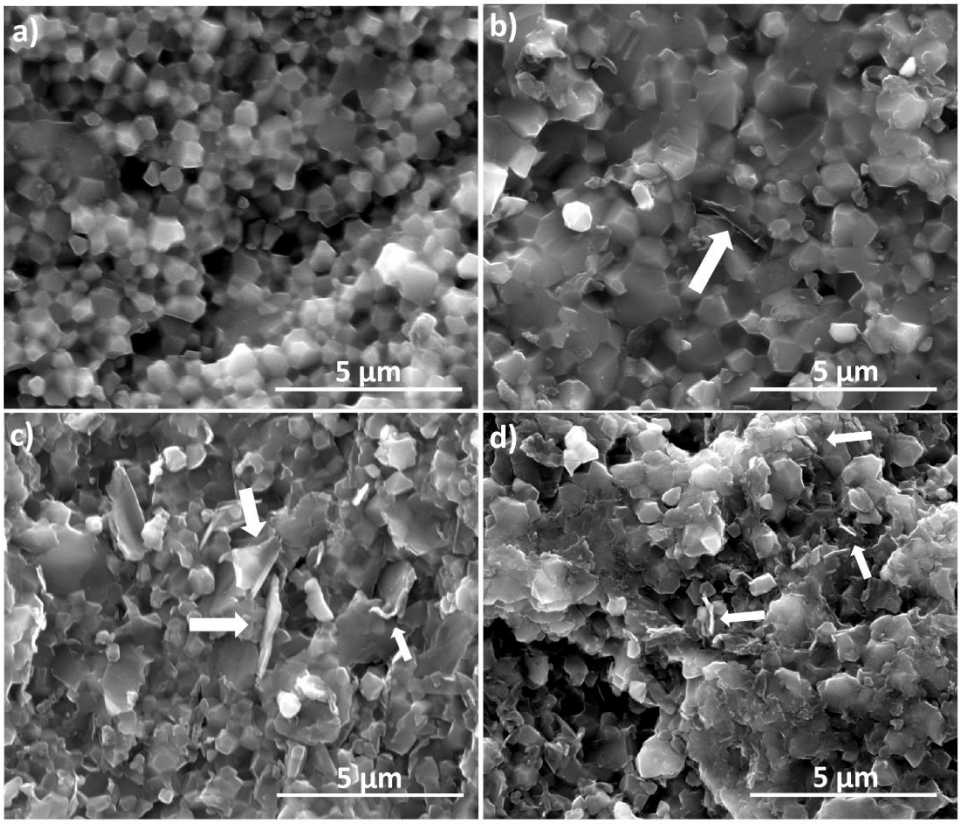

Figure 8.6 SEM images showing the fractured surface after the scratch test for: **a)** alumina; **b)** alumina-GNP (0.5 vol%); **c)** alumina-GNP (2 vol%) and; **d)** alumina-GNP (5 vol%) composites.

Figure 8.7 illustrates the behaviour of alumina and alumina-GNP composites during the scratch testing. In the case of alumina-GNP composites, GNP were located at the grain boundaries of the alumina grains. An improved scratch resistance in the case of alumina-GNP composites was only observed at low loads because of the improved mechanical properties of the composites **(Chapter 7)**. With increasing load the cracks interact directly with the GNP at the grain boundaries. The GNP acts as reinforcement resisting the propagation of cracks, and there is some improvement

in the scratch resistance of alumina composites. However, with increasing applied load increasing micro-cracking leads to chipping and grain pull out. When the concentration of GNP is high there is overlapping of GNP at the grain boundaries. This overlapping and high concentration of GNP leads to the formation of an interconnected network of GNP around the alumina grains (shown with white arrows in **Figure 8.7 (b)**) which results in WBG in the alumina matrix. Thus during the scratch testing when a grain is pulled out in the alumina-GNP composites other interconnected grains in the GNP network are also removed, resulting in more extensive chipping in the alumina-GNP composites. This results in decreased scratch resistance of the alumina-GNP composites at high loads.

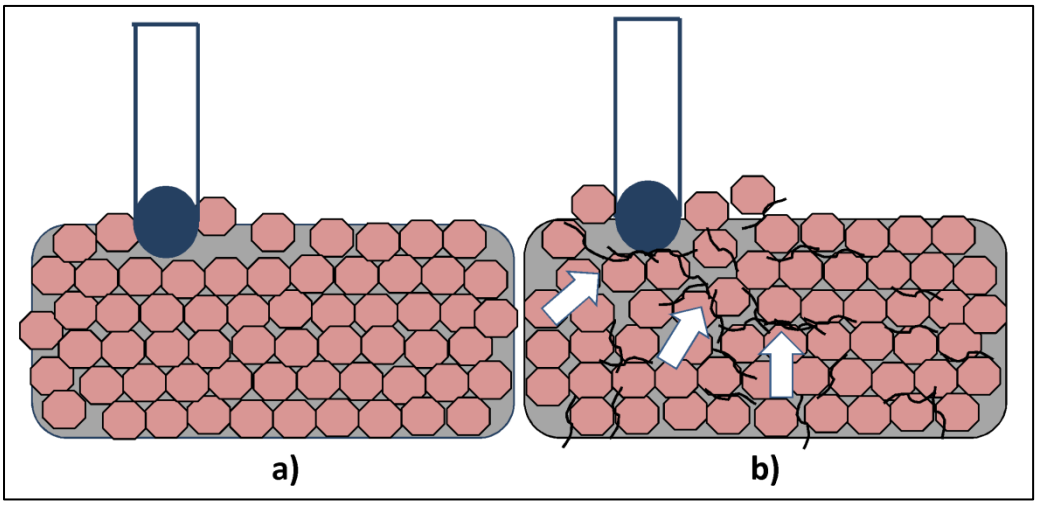

Figure 8.7 Illustration of the mechanisms involved during the scratch test (region 3) for: **a)** alumina and; **b)** alumina-GNP composites.

It should be noted that authors have reported an improvement in the wear resistance of glass/ceramic nano-composites with the addition of GNP [173]. Most of the works reported have used a ball on disc method to measure the wear resistance

of these material for long sliding distances (>300 m) and various loads (1-200 N). In the case of tribological properties measured using ball on disc methods, authors reported the formation of a tribofilm on composite surfaces. GNP removed during tribology testing acts as a lubricant and forms a tribofilm because of the repeated movement of the counterpart material on the nano-composite surfaces. This avoids further removal of material, resulting in improved wear resistance. In fact Belmonte et al. [169] saw more of an improvement in the wear resistance of silicon nitride-GNP composites at high loads compared to low loads because more GNP was removed during the tribology testing which resulted in the formation of a tribofilm on the material surface. In the case of scratch testing, the normal applied load increases linearly with distance and there is no repeated movement of the counterpart on the nano-composite surfaces thus avoiding any tribofilm formation. Even though a significant amount of GNP is removed from the material that contains a higher loading of GNP, it cannot have a beneficial effect on the scratch resistance of the composites due to the fact that no tribofilm forms. Instead, it results in more grain removal from alumina-GNP composites because of the inter-connected network formation of GNP around alumina grains which contributes to extensive chipping.

8.4 Conclusion

The scratch resistance of the alumina-GNP (0.5, 2 and 5 vol%) composites was investigated using single pass scratch testing. The COF of the composites did not change much for low loads but increased at high loads with increasing concentration of GNP in the alumina matrix. The COF of alumina-GNP (5 vol%) composite was ~60% higher compared to pure alumina sample. Similarly the scratch resistance of the alumina-GNP (0.5 vol%) composites increased for low normal applied loads compared to pure alumina. The first radial cracks in the case of alumina-GNP composites were observed at a normal applied load of 97 N compared to 89 N in the case of pure alumina. The improved scratch resistance of alumina-GNP (0.5 vol%) composite was attributed to increased fracture toughness and decreased brittleness index. As the applied load was increased, the scratch resistance of the alumina-GNP composite decreased mainly due to the formation of WBG in the alumina matrix. The formation of WBG was also confirmed by the decrease in elastic modulus (~15%) of alumina-GNP composites (5 vol%). The scratch resistance properties obtained were in good agreement with the mechanical properties of the composites. The results and observation of this work suggests that low concentrations of GNP produce good reinforcement and improved scratch resistance of the alumina nano-composites up to a critical load.

Chapter 9 Processing and bioactivity of 45S5 Bioglass®-Graphene Nanoplatelets composites

9.1 Introduction

Bioglass® (45wt.% SiO_2, 24.5wt% CaO, 24.5wt% Na_2O and 6wt% P_2O_5) was originally developed by Prof. Larry Hench in 1969 [174], and since then it has received increasing attention due its unique properties in the field of biomaterials and regenerative medicine, with clinical applications since 1985 [175]. BG is a biocompatible and bioactive material with the potential for osteinduction which encourages the repair and regeneration of bone tissue [176-178]. BG increases the bone-implant contact and bone growth rate by the formation of a bioactive layer of hydroxyapatite (HA) over the surface of the biomaterial. The HA layer allows osteogenic stem cells to attach over it and differentiate with the subsequent formation of bone [179-181]. Beyond its bioactivity, BG also shows angiogenesis, antibacterial and anti-inflammatory effects in-vivo and in-vitro [182-184]. The surface of the BG plays an important role in its bioactivity applications, therefore surface modification approaches are being continuously investigated for improving the biocompatibility and bioactivity of biomaterials [185]. Carbon nanomaterials have attracted significant research efforts to modify the surface of biomaterials [186]

due to their unique ability to simulate protein adhesion along with their high reactivity which improves cellular functions.

Advanced biomaterials with multi functionalities might accelerate new tissue formation. When bone is subjected to mechanical stresses its deformation leads to electric signals (piezoelectric effect), this can contribute to bone regeneration and fracture healing [187, 188]. Therefore using electrically conductive nano filler (e.g. GNP, CNTs) might enable further functionalisation of biomaterials. These electrically conductive biomaterials can be used in bone tissue engineering to facilitate cell growth and tissue regeneration with physioelectrical signal transfer [189]. It has been reported that CNTs can significantly increase the electrical conductivity of biomaterials, and CNT coatings can also enhance the attachment and growth functions of different cell line, including osteoblasts [190-192]. CNTs have also been applied with BG scaffolds for bone tissue engineering [193]. Although CNTs have shown very promising results, the main issues associated with their use for biomedical applications are: 1) their cost [194]; 2) presence of residual metallic impurities; and most importantly; 3) difficulty in processing them. On the other hand GNP with excellent mechanical [13], electrical [12] and thermal [14] properties are relatively inexpensive and easy to process. The 2D nanostructure and high specific surface area of GNP [15] makes them easy to disperse in a matrix compared to CNTs which usually requires surface modification [2]. In a recent work by Fabbri et al. [195], it was demonstrated that BG scaffolds coated with graphene were biocompatible and supported cellular activity for MG-63 cells. Graphene enhanced the electrical conductivity of the BG scaffolds without impairing the bioactivity. Other than improving functional properties, graphene can also be used to enhance mechanical properties of BG composites [27, 82].

In this study the effect of addition of GNP on the bioactivity and electrical conductivity of BG was investigated. GNP was synthesized using a liquid phase exfoliation method. Synthesized GNP was used to prepare BG-GNP composites. The first step included the optimization of the processing methods (powder, colloidal) for preparing BG-GNP powder mixtures using various solvents. In the second step, composites with increasing vol% of GNP were prepared using a powder processing method. In our previous work we showed that SPS produced near full densification of amorphous BG which was more bioactive compared to crystalline pressureless sintered BG [127]. Therefore, SPS was used to sinter BG-GNP composites; the low processing temperature (600 ^{o}C) avoided any structural damage to the GNP. Finally, the bioactivity and electrical conductivity of the nano composites were characterized.

9.2 Experimental Section

Details about GNP synthesis are provided in **chapter 3**. In order to optimise the processing conditions for preparing well dispersed BG-GNP (1 vol%) composites, two different processing methods namely: powder and colloidal processing were investigated **(chapter 3)**. Three different solvents were considered: di-methyl formamide (DMF), acetone (Sigma Aldrich) and de-ionised water (DI water). The choice of the solvents was guided by the literature, which suggested that the suitable dispersion of GNP can be readily achieved in these solvents [41, 128]. It should be noted that GNP powders were prepared after removing the solvent from already prepared GNP-NMP suspension. The dried GNP powders were used to prepare GNP suspensions in various solvents. The details about sintering and

characterisation of the BG-GNP composites using SEM, XRD, Raman spectroscopy and electrical conductivity measurement are provided in **chapter 3**.

For bioactivity studies, the samples were immersed in simulated body fluid (SBF), which was prepared using Kokubo's procedure [196]. BG-GNP composites were immersed in SBF for 1 and 3 days at 37 °C in an incubator with a composites surface to SBF volume ratio of 0.02 cm^{-1}. The composites were subsequently cleaned with distilled water and preserved to avoid contamination. The composites surfaces were evaluated using XRD and SEM for hydroxyapatite (HA) formation.

9.3 Results and Discussion

9.3.1 Microstructural Characterisation

Figure 9.1 shows SEM images of BG and BG-GNP composite powders processed using various solvents and processing methods. **Figure 9.1 a)** shows the as received pure BG. The average particle size was ~60 µm. **Figure 9.1 b) and c)** powders of BG-GNP (1 vol%) composite processed using colloidal processing method, with acetone + DI water and only DI water as solvents, respectively. As expected, there was no significant change in the average particle size for BG-GNP composites processed using colloidal processing compared to as received pure BG powder. **Figure 9.1 d)** shows powders of BG-GNP (1 vol%) composite processed using powder processing method and DMF as solvent. Powder processing reduced the average particle size for BG down to ~8-10 µm.

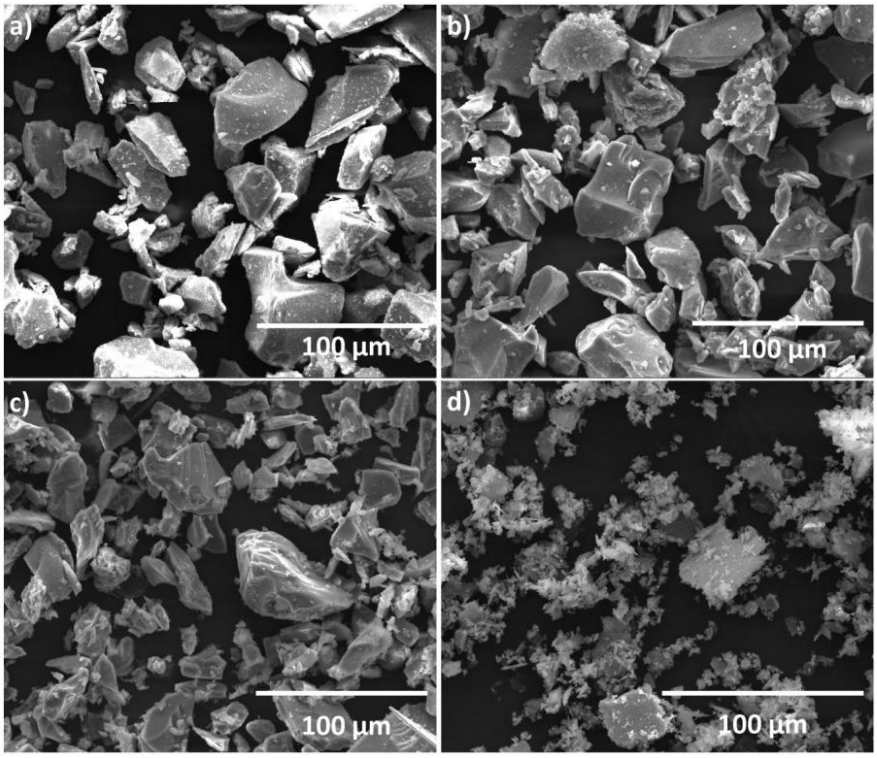

Figure 9.1 SEM images of BG and BG-GNP (1 vol%) composite powders after processing; **a)** Pure BG; **b)** BG-GNP (colloidal processing-Acetone + DI water); **c)** BG-GNP (colloidal processing-DI water and; **d)** BG-GNP (powder processing-DMF).

The BG-GNP powders were densified using the SPS furnace. **Figure 9.2** shows temperature profile, relative piston travel and speed (piston travel rate) with respect to sintering time as recorded by SPS furnace for pure BG sample. BG and BG-GNP composites were sintered at 600 ^{o}C with 2 minutes dwell time. The short dwell time during high temperature processing avoided structural damage of the GNP as confirmed by Raman spectroscopy. As shown in **Figure 9.2**, powders started to densify at ~400 ^{o}C, and with increasing temperature a sharp densification peak was observed at ~500 ^{o}C. The sharp sintering peak corresponds to the viscous flow of amorphous BG while the pressure was kept constant throughout the sintering

process. Relative piston travel confirmed full densification of the material at ~550 ^{o}C.

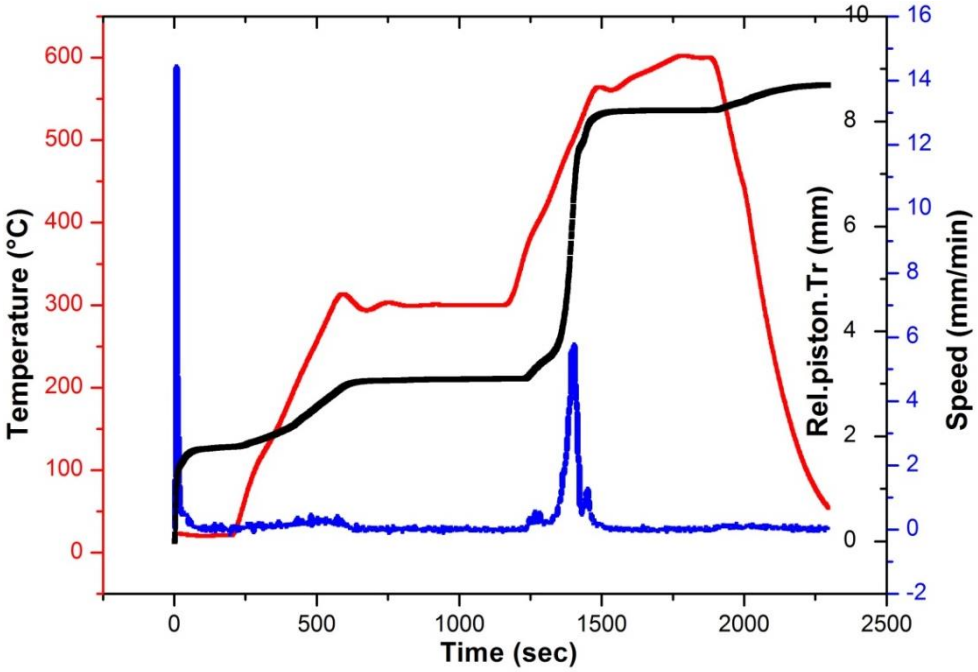

Figure 9.2 Sintering profile of pure 45S5 Bioglass® sample during SPS processing (600 ^{o}C/70 MPa/2 min) showing temperature profile (red curve), relative piston travel (black curve) and shrinkage rate/speed (blue curve). The shark sintering peak confirm viscous flow sintering mechanism for 45S5 Bioglass® sample.

In order to evaluate the quality of the dispersion of GNP in the BG matrix, fractured surfaces of BG-GNP composites were analysed using SEM. **Figure 9.3** shows SEM images of the fractured surface of BG-GNP (1 vol%) composites prepared using various processing methods and solvents. **Figure 9.3 a)** shows the dispersion of GNP in the BG matrix processed using colloidal processing using a mixture of acetone and DI water as the solvent. The particle size of BG was ~60 µm and most of the GNP was on the original surface of these large particles resulting in

poor dispersion. The inset in **Figure 9.3 a)** is a high magnification image of GNP trapped in between two BG particles. **Figure 9.3 b)** shows a fracture surface of BG-GNP (1 vol%) composite made using colloidal processing route and DI water as solvent. As in the previous case, GNP was found to be trapped in between the BG particles. The inset in **Figure 9.3 b)** shows agglomerated GNP in between BG particles. **Figure 9.3 c)** is a low magnification image of BG-GNP (1 vol%) composite processed using powder processing and DMF as the solvent. The best results in terms of microstructural homogeneity were obtained using this method, and GNP was found to be evenly distributed throughout the BG matrix. Powder processing dramatically reduced the particle size of the BG powders, resulting in finer particles **(Figure 9.1 (d))**. Also due to the two dimensional (2D) geometry and good solubility of GNP in DMF, it was easier to obtain good dispersion of GNP in the BG matrix for the samples processed using powder processing compared to colloidal route. **Figure 9.3 d)** is a high magnification image of BG-GNP (1 vol%) composites made using powder processing showing the pullout of GNP from the BG matrix. Some preferential alignment of GNP in the BG matrix in a direction perpendicular to the applied force can be observed in **Figure 9.3 (d)**. Alignment was also observed for silica-GNP composites. This behaviour can be attributed to viscous flow during sintering of BG and the high specific surface area and two dimensional (2D) geometry of GNP.

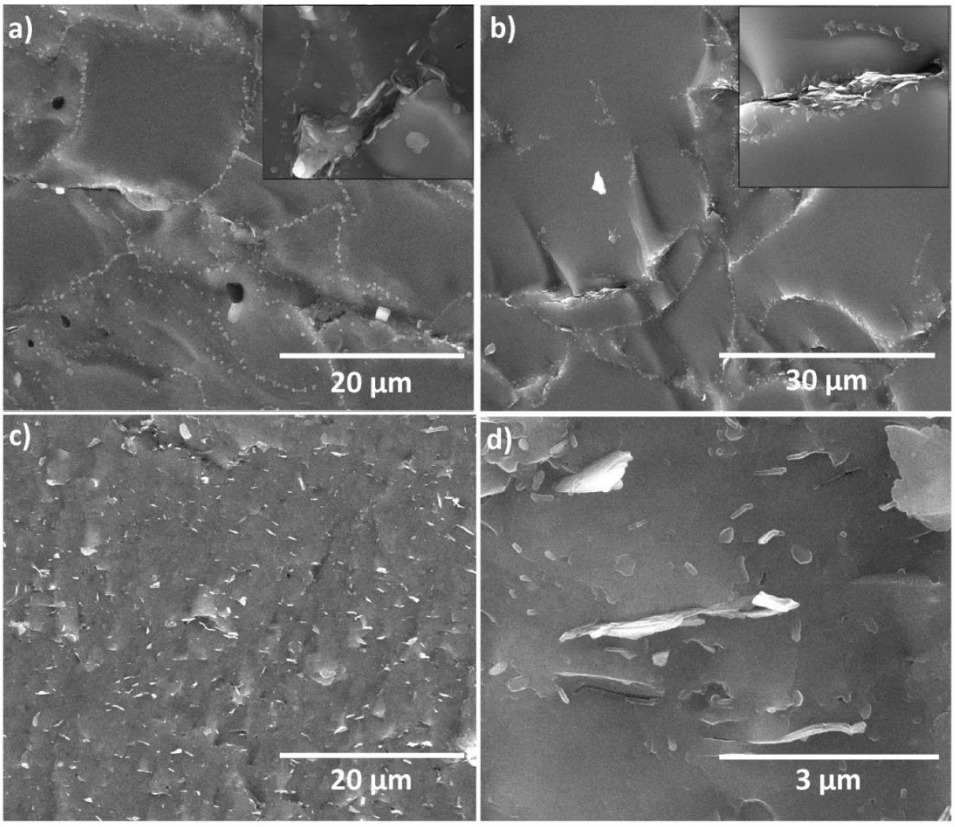

Figure 9.3 SEM images showing fractured surfaces of BG-GNP (1 vol%) composites processed using different solvents and processing methods; **a)** colloidal processing using Acetone and DI water; **b)** colloidal processing using DI water; **c)** low and; **d)** high magnification images processed using powder processing and DMF as solvent.

BG-GNP composites prepared using the powder processing method gave the best results in terms of dispersion. Therefore this processing route was considered most suitable for preparing BG-GNP composites with various GNP loadings. BG-GNP composites with 1, 3 and 5 vol% loading were prepared and the amount of GNP loading were selected corresponding to GNP contents below and above percolation threshold as demonstrated in **Section 9.3.2**. The prepared powders were

consolidated using SPS (600 ^{o}C/70 MPa/ 2min) and their sintering profile was recorded. Interestingly, addition of GNP to the BG matrix affected the sintering behaviour of BG. **Figure 9.4 a)** shows the shrinkage peaks of BG-GNP (1, 3 and 5 vol%) composites with respect to temperature. A sharp sintering peak was observed at ~500 ^{o}C in the case of pure BG. This was shifted by ~50 ^{o}C to a higher temperature for BG-GNP (1 and 3 vol%) composites. Addition of GNP to BG matrix increases the viscosity of BG-GNP composites. This increase in viscosity hindered the viscous flow sintering mechanism resulting in higher sintering temperatures. In the case of BG-GNP (5 vol%) composite, the sintering peak was broader compared to the other composites, and the shift in peak was relatively less (~30 ^{o}C). It is well known that GNP have very good thermal conductivity [160], therefore this change in behaviour compared to BG and BG-GNP (1 and 3 vol%) might be attributed to the increased thermal conductivity of the BG-GNP (5 vol%) composite. The heat would have diffused more evenly during sintering producing more rapid densification of BG-GNP (5 vol%) powders resulting in a broadened sintering peak.

The sintered composites were analysed using Raman spectroscopy in order to quantify the effect of high temperature processing on GNP in SPS. **Figure 9.4 b)** shows the Raman spectra for GNP, BG-GNP (1 vol%) powder and BG-GNP (1, 3 and 5 vol%) composites. The typical three peaks at ~1350 cm^{-1} (D band), ~1585 cm^{-1} (G band) and ~2700 cm^{-1} (2D band) are observed for GNP as well as for BG-GNP powder and composites. The D peak intensity in the case of liquid phase exfoliated GNP can be related to edge defects. The ratio of the intensity of the D peak to the G peak gives some indication of the amount of defects introduced into GNP during processing and sintering. The I_D/I_G ratios were calculated from the Raman spectra and compared for all the samples. The I_D/I_G ratio in the case of pure

GNP was ~0.24 which is typical for liquid phase exfoliated GNP. The I_D/I_G ratio values were compared after each processing step in order to quantify the defects introduced into GNP after processing and sintering. The I_D/I_G ratio of BG-GNP (1 vol%) powder was ~0.29, which is slightly higher, but within the error bars, compared to pure GNP suggesting that the GNP was not damaged during the powder processing step. In the case of BG-GNP (1, 3 and 5 vol%) composites, the I_D/I_G ratios were ~0.51, 0.48 and 0.41 respectively. The increase in I_D/I_G ratio in the case of sintered nano-composites compared to pure GNP suggests that some defects were introduced into the GNP during SPS processing, but the damage was not significant. In fact the typical value of I_D/I_G ratio for heavily damaged graphene is of the order of ~1 to 3. Interestingly, with increasing concentration of GNP, the I_D/I_G ratio values decreased for BG-GNP (1, 3 and 5 vol%) composites. This can be attributed to the more frequent overlapping of GNP which resulted in decreased D peak intensity due to decreased edge defects and hence lower I_D/I_G values. It should be noted that there was also some small shift in D and G peaks for BG-GNP composites compared to GNP and BG-GNP powder. The D and G peaks in case of GNP and BG-GNP powder were observed at ~1345 and ~1573 cm^{-1}. These peak positions were shifted by ~6 cm^{-1} to a higher value in the case of BG-GNP sintered composites. This small shift in the D and G peaks is produced because of the residual compressive stresses introduced into the sintered GNP due to both the mismatch in thermal expansion coefficient of the BG and GNP [148, 162] and the uniaxial mechanical stress applied during SPS.

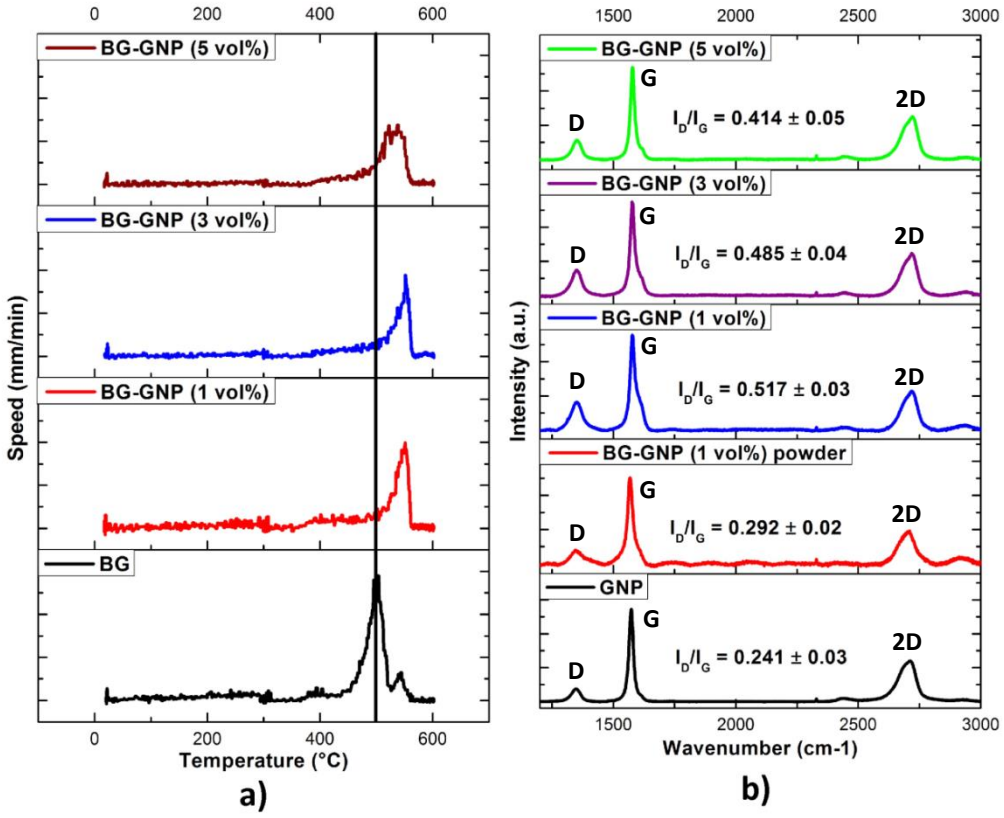

Figure 9.4 a) shows shift in the sintering peak with respect to temperature for BG nano-composites with the addition of GNP; **b)** Raman spectra of GNP, BG-GNP (1 vol%) powder and BG-GNP (1, 3 and 5 vol%) composites showing the extent of damage to GNP before and after processing and sintering in SPS.

9.3.2 Electrical Conductivity

Table 9.1 lists the bulk, theoretical densities and electrical conductivities of BG-GNP (1, 3 and 5 vol%) composites. Density measurements confirmed that all of the samples were highly dense (>99%). As expected the electrical conductivity of the composites increased with increasing concentration of GNP in the BG matrix. There was an increase of ~9 order of magnitude in the electrical conductivity of BG-GNP (5 vol%) composite compared to pure BG. The formation of a percolating network of

GNP inside the BG matrix resulted in a sudden increase in electrical conductivity of the BG-GNP (3 and 5 vol%) composites. The BG-GNP (3 and 5 vol%) composites had electrical conductivity values of ~3 and 13 S/m, respectively. The improved electrical conductivity in case of BG-GNP composites is sufficient to stimulate cell growth and tissue regeneration by facilitating physioelectrical signal transfer [189].

Table 9.1 Bulk, relative theoretical densities and electrical conductivity of BG-GNP (1, 3 and 5 vol%) composites prepared by powder processing. All the samples were sintered at 600 ^{o}C under 70 MPa pressure with 2 minute dwell time.

Sample	**Bulk Density (g/cc)**	**Theoretical Density (g/cc)**	**% Theoretical Density**	**Electrical Conductivity (S/m)**
BG	2.70	2.72	99.3	6.13×10^{-8}
BG + GNP (1 vol%)	2.708	2.715	99.7	9.96×10^{-8}
BG + GNP (3 vol%)	2.682	2.704	99.2	3.22
BG + GNP (5 vol%)	2.688	2.694	99.8	13

9.3.3 Bioactivity

After preparing well dispersed BG-GNP composites with improved electrical conductivities, the bioactive response of the nano-composites was compared to pure BG samples. In order to perform the bioactivity testing, BG-GNP (1, 3 and 5 vol%) composites were immersed in SBF solution [196] for 1 and 3 days. HA formation on the surface of BG and BG-GNP composites after immersion in SBF was characterized using XRD and SEM.

Figure 9.5 shows the XRD diffraction patterns for BG, BG-GNP (1, 3 and 5 vol%) composites before and after immersion in SBF. Comparison of the XRD patterns was important to understand the effect of GNP on the bioactive response of BG. **Figure 9.5 (a)** shows the XRD diffraction pattern for BG and BG-GNP composites before SBF treatment. XRD confirmed the crystallization of BG and BG-GNP composites after sintering at 600 ^{o}C. The amorphous to crystalline ratio for BG-GNP composites was determined after a detailed analysis of the XRD data. Pure BG, BG-GNP (1, 3 and 5 vol%) composites had 89.3, 54.6, 62 and 54.8 weight% crystallinity respectively. BG-GNP composites were less crystalline compared to pure BG. In summary GNP retarded densification (**Figure 9.4 (a)**) and inhibited crystallization of the composites. Similar behaviour have also been reported by Cho et al. [5] for silica-carbon nanotube (CNTs) composites where they reported decrease in crystallinity with increasing concentration of CNTs in silica matrix. It has been reported that amorphous BG exhibits higher bioactivity than crystalline BG [197]. In our study, the higher weight fraction of amorphous phase in the case of BG-GNP composites might result in improved bioactivity of the BG-GNP composites compared to pure BG.

The main crystallization phase observed for both BG and BG-GNP composites was sodium calcium silicate ($Na_2CaSi_3O_8$, PDF 00-012-0671). There was an overlapping of peaks at 26.3^o, which corresponds to the crystalline phase of GNP and $Na_2CaSi_3O_8$ [198], resulting in no observable difference in the XRD peaks of sintered BG with and without GNP. **Figure 9.5 (b)** shows the XRD pattern for sintered BG and BG-GNP composites (1, 3 and 5 vol%) after 1 day immersion in SBF. A decrease in the relative intensity of the crystalline peaks suggests the formation of a new crystalline layer on the surface of BG and BG-GNP composites. A new crystalline peak at ~32^o corresponding to HA (PDF 00-001-1008) was observed for all the samples suggesting that all of the samples were bioactive even after only 1 day of immersion in SBF. **Figure 9.5 (c)** shows the XRD patterns for BG and BG-GNP (1, 3 and 5 vol%) composites after 3 days of immersion in SBF. The intensity of the HA peak increased with increased time in SBF for all of the samples. Also it was interesting to see that the intensity of the crystalline peak due to $Na_2CaSi_3O_8$ decreased further suggesting the formation of a thicker HA layer on BG and BG-GNP composites. When comparing the intensities of the crystalline peaks of $Na_2CaSi_3O_8$ phase, it is apparent that more crystalline peaks are present for BG compared to BG-GNP composites.

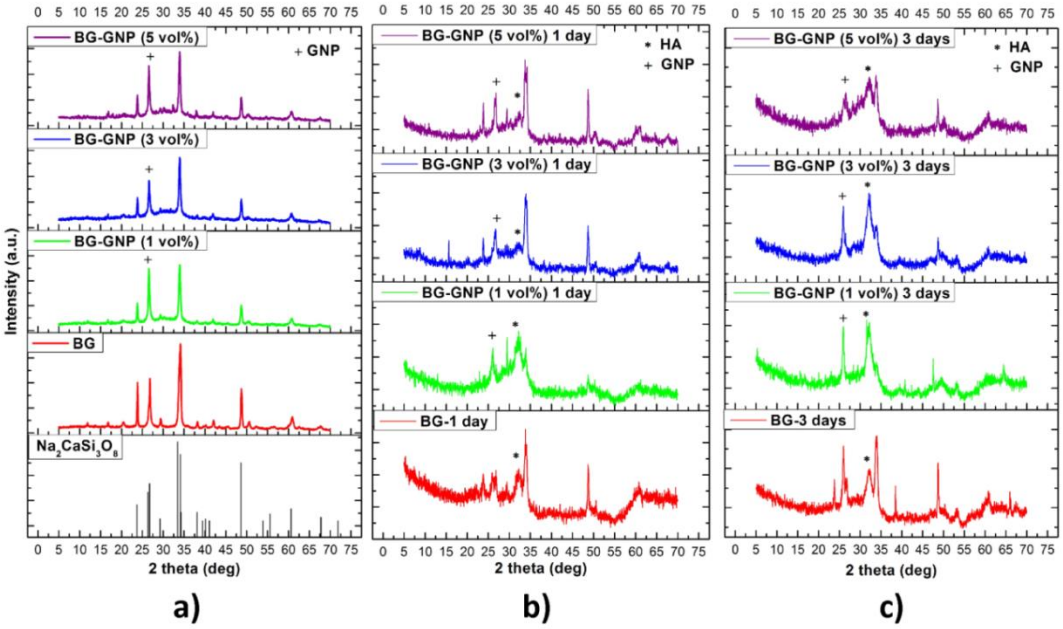

Figure 9.5 XRD spectra of BG and BG-GNP (1, 3 and 5 vol%) composites; **a)** as sintered; **b)** after 1 day immersion and; **c)** after 3 days immersion in SBF.

The morphology of the HA layer formation was also confirmed using SEM. **Figure 9.6** shows low magnification SEM images of BG and BG-GNP (1, 3 and 5 vol%) composites after 1 day immersion in SBF. The formation of a HA layer is clear for all the samples (thick layers on the surfaces of BG and BG-GNP composites which is not observed for samples without SBF test). There was no observable difference in the morphology of the HA layer formed for composites with different vol% loading of GNP, suggesting that GNP did not hinder the bioactivity of BG. In fact the size of the cracks in the HA layer suggests that the layers formed were quite thick.

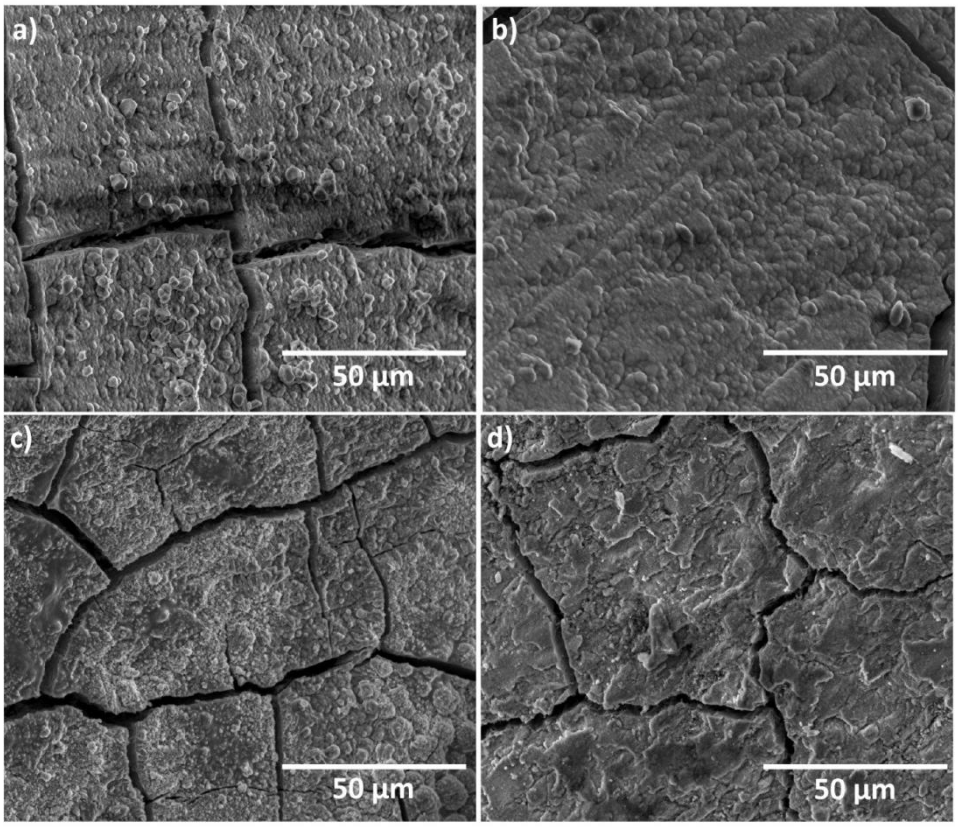

Figure 9.6 Low magnification SEM images of BG and BG-GNP composites showing the formation of HA after 1 day immersion time in SBF; **a)** Pure BG; **b)** BG-GNP (1 vol%); **c)** BG-GNP (3 vol%); and **d)** BG-GNP (5 vol%) composites.

Figure 9.7 shows the high magnification SEM images of BG and BG-GNP composites after 3 days immersion in SBF. **Figure 9.7 (a)** is the SEM image for pure BG sample showing the cauliflower-like structure typical of the formation of HA on top of the BG surface. **Figures 9.7 (b), (c) and (d)** are the SEM images of BG-GNP (1, 3 and 5 vol%) composites, respectively, showing the same cauliflower-like structures formation in case of the nano-composites. Interestingly the HA structures formed on BG-GNP composites were larger in size compared to pure BG samples, suggesting that the BG-GNP might be more reactive than pure BG when immersed

in SBF. The addition of GNP to BG may have introduced some nano-roughness to the BG-GNP composite surfaces resulting in enhanced bioactivity [189, 193]. It is clear that the addition of GNP to BG matrix increased the electrical conductivity of BG-GNP composites without affecting the intrinsic bioactivity of BG. Besides improving electrical conductivity, the addition of GNP to BG may also improve the mechanical properties of the prepared composites which can be considered a further advantage of the use of GNP as filler in BG based composites with potential application in bone tissue engineering.

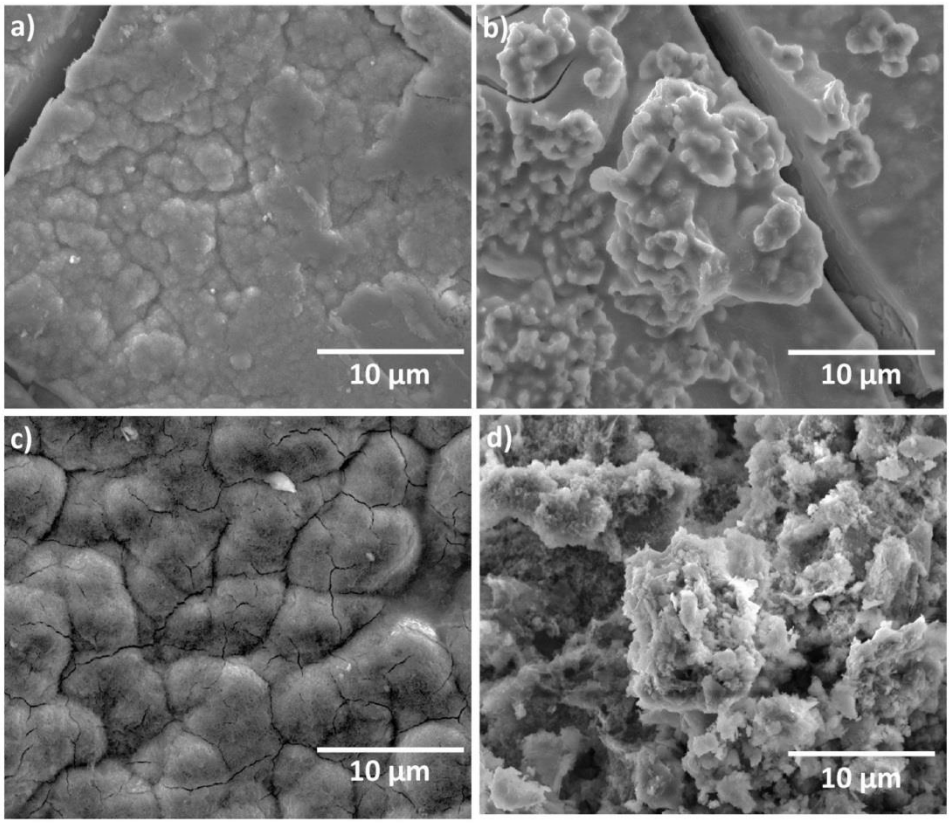

Figure 9.7 High magnification SEM images of BG and BG-GNP composites showing the formation of HA after 3 day immersion time in SBF; **a)** Pure BG; **b)** BG-GNP (1 vol%); **c)** BG-GNP (3 vol%); and **d)** BG-GNP (5 vol%) composites.

9.4 Conclusion

Well dispersed BG-GNP composites were obtained by optimizing the processing conditions. Different processing methods, namely colloidal and powder processing, were investigated using various solvents (acetone + DI water, DI water and DMF). The best results were obtained using powder processing; ball milling resulted in finer BG particles contributing to a good dispersion of GNP in the BG matrix. BG-GNP (1, 3 and 5 vol%) composites were prepared for the first time using SPS (600 ^{o}C/70 MPa/ 2 min). GNP increased the viscosity of BG composites, resulting in a detectable increase in the sintering temperature of BG-GNP composites by 50 ^{o}C compared to pure BG. SPS avoided structural damage of GNP during high temperature processing, as confirmed by Raman spectroscopy. In vitro bioactivity tests were performed on BG-GNP composites using immersion tests in SBF for up to 3 days. XRD confirmed the formation of HA on all samples. Cauliflower-like HA structures were observed using SEM confirming the bioactivity of nano-composites. Furthermore, the HA cauliflower-like structures formed on the surface of the samples were more pronounced for the BG-GNP samples than those of the pure BG samples. This effect could be due to the nano-roughness imparted by the GNP. GNP increased the electrical conductivity of BG-GNP composites by ~9 orders of magnitude compared to pure BG without affecting its bioactivity. Future work will focus on stimulating cell growth on conductive BG-GNP composites by applying electric field and understanding the effect of GNP on cells growth/survivability, the aim being the development of functional scaffolds for bone regeneration applications.

Chapter 10 Conclusion and Future Work

10.1 Conclusion

In the present research, various problems associated with fabrication of GNP-glass/ceramic composites were investigated and conditions for preparing well dispersed GNP-glass/ceramic composites were optimised. The prepared composites were characterised for mechanical, tribological, electrical and biological properties. Both amorphous (silica, BG) and polycrystalline matrices (alumina) with different microstructures were investigated in order to understand the effect of GNP on the prepared composites. Interestingly, GNP behaved differently in different matrices. High loading GNP (≥5 vol%) are good for producing reinforced glass nano-composites compared to ceramic composites where low loading of GNP (≤ 1 vol%) gave better results. Biological properties are also enhanced with increasing concentration of GNP in the BG matrix.

10.1.1 GNP

Good quality GNP was prepared using liquid phase exfoliation method. The prepared GNP was characterised using UV, Raman and TEM. The length, width and thickness of prepared GNP flakes was measured for at least 100 flakes. The average length was found to be ~1.5 μm with a thickness of 3-4 layers.

10.1.2 Silica-GONP/GNP composites

The conditions for preparing well dispersed silica-GNP and silica-GONP nano-composites were optimised using powder and colloidal processing routes. Raman spectroscopy and XRD results confirmed that the GONP was reduced to GNP during high temperature processing in SPS. Alignment of GNP in the silica matrix was observed perpendicular to the pressing direction in SPS. Fracture toughness of the silica-GNP composites increased with increasing concentration of GNP. There was an improvement of ~45% in the fracture toughness of the composites with the addition of 5 vol% GNP. Various toughening mechanism including GNP necking, GNP pull-out, crack bridging, crack deflection and crack branching were observed. The addition of GNP to silica matrix enhanced the machinability of silica-GNP composites. GNP reduced the coefficient of friction of the silica-GNP composites by 20% compared to pure silica. There was an improvement of ~5.5 times in the wear resistance of the silica-GNP composites. GNP above a critical content formed an interconnecting network, which provided an effective lubricating effect to the silica matrix resulting in improved wear properties. The present study suggests that high concentration of GNP is a good reinforcement for improving both mechanical and tribological properties of brittle matrices.

10.1.3 Alumina-GNP composites

Well dispersed Alumina-GNP composites were prepared using powder processing route. There was an improvement of ~40% in the fracture toughness of the composites prepared with the addition of only 0.8 vol% GNP. GNP was found to be anchored in between the grains of alumina and different toughening mechanism

were observed including GNP pull out, crack bridging, crack deflection and crack branching. A trans-granular mechanism of crack propagation became more dominant with increasing GNP content. The fracture toughness and elastic modulus of the nano-composites decreased for composites with ≥2 vol% GNP. This was attributed to an increase in number of sites with inter connecting GNP. The scratch resistance of the alumina-GNP (0.5, 2 and 5 vol%) composites was investigated. The COF of the composites did not change much for low loads but increased at high loads with increasing concentration of GNP in the alumina matrix. The COF of alumina-GNP (5 vol%) composite was ~60% higher compared to pure alumina sample. Similarly the scratch resistance of the alumina-GNP (0.5 vol%) composites increased for low normal applied loads compared to pure alumina. The improved scratch resistance of alumina-GNP (0.5 vol%) composite was attributed to increased fracture toughness and decreased brittleness index. As the applied load was increased, the scratch resistance of the alumina-GNP composite decreased mainly due to the formation of weak bonded grain boundaries in the alumina matrix. The results and observation of this work suggests that low concentrations of GNP produce good reinforcement and improved scratch resistance of the alumina nano-composites up to a critical load.

10.1.4 BG-GNP Composites

Well dispersed BG-GNP composites were obtained by optimizing the processing conditions. Different processing methods, namely colloidal and powder processing, were investigated. BG-GNP (1, 3 and 5 vol%) composites were prepared using powder processing route and sintered using SPS. In vitro bioactivity tests were performed on BG-GNP composites using immersion tests in SBF for up to 3 days. XRD confirmed the formation of hydroxyapatite (HA) on all samples. Cauliflower-

like HA structures were observed using SEM confirming the bioactivity of nano-composites. GNP increased the electrical conductivity of BG-GNP composites by ~9 orders of magnitude compared to pure BG without affecting its bioactivity.

10.2 Future Work

1. The addition of GNP in the glass/ceramic matrix leads to improvement in fracture toughness of the composites. One of the toughening mechanisms that lead to such improvements was reported to be crack deflection. The addition of GNP generated stresses in the glass/ceramic matrix due to mismatch in the thermal coefficient of expansions of GNP and glass/ceramics. The stresses on GNP in the glass/ceramic matrix leads to shifts in D, G and 2D peak positions of GNP and can be observed using Raman spectroscopy. These stresses contribute to toughening of the composites and could be studied and quantified using Raman spectroscopy.

2. Various toughening mechanisms including crack deflection, crack bridging, crack branching, GNP pull-out are reported in the present work. It is still not clear how much does each toughening mechanism contributes to the fracture toughness of the material? In literature authors have reported toughening models for fibre reinforced glass/ceramic composites. Optimisation of these classical toughening models is needed in order to quantify various toughening mechanisms involved in GNP-glass/ceramic composites.

3. The primary focus of the present work was optimisation of processing and fabrication conditions for preparing glass/ceramic composites and characterising them for mechanical properties. Since, GNP has very good functional properties, thermal and electrical properties of the glass/ceramic composites could be studied. Also we report alignment of GNP in a direction perpendicular to the applied pressure in SPS. Both mechanical and functional properties of the prepared glass/ceramic composites could be investigated in different directions with respect to alignment of GNP. The properties are expected to be different depending on the alignment of GNP. Such anisotropic properties in composites can have many potential applications.

4. The results reported so far in literature used different kinds of GNP to understand the effect of GNP on the mechanical and functional properties of glass/ceramic composites. Since it has been shown that quality of GNP used for fabricating glass/ceramic composites plays a crucial role in the final properties of the composites. It will be interesting to investigate the effect of different size GNP flakes on the mechanical and functional properties of glass/ceramic composites. It is expected that composites prepared using different size GNP flakes will have different mechanical and functional properties.

   Also in the present work we report how GNP behaves differently in amorphous and polycrystalline matrices. Another important question that can be answered is how different size GNP flakes will influence the properties of amorphous and polycrystalline materials.

5. The main idea for fabricating BG-GNP composites was to use a conductive nano-filler to improve the electrical conductivity of the composite and use these electrically conductive composites for bone tissue engineering to facilitate cell growth and tissue regeneration with physioelectrical signal transfer. In the present work we observed that addition of GNP leads to the improvement of bioactivity of the composites. Future work could focus on stimulating cell growth on conductive BG-GNP composites by applying electric field and understanding the effect of GNP on cells growth/survivability, the aim being the development of functional scaffolds for bone regeneration applications.

   Also since GNP has shown remarkable improvement in the mechanical properties of glass/ceramic composites, mechanical properties of BG-GNP composites are expected to improve and could be investigated.

6. Other than graphene there are various 2D materials (Maxenes, BN, MoS_2, WS_2, Bi_2Te_3 etc.) with exotic electrical properties and high specific surface areas which are important for various applications including sensing, catalysis and energy storage. Although graphene is the most well studied 2D material there is potential for exploiting other 2D materials and fabricating novel composites with them.

List of Publications

1. H. Porwal, S. Grasso, and M. Reece: 'Review of graphene-ceramic matrix composites', *Adv Appl Ceram*, 2013, **112**(8), 443.
2. H. Porwal, S. Grasso, M. K. Mani, and M. J. Reece: 'In situ reduction of graphene oxide nanoplatelet during spark plasma sintering of a silica matrix composite', *J Eur Ceram Soc*, 2014(0).
3. H. Porwal, P. Tatarko, S. Grasso, C. Hu, A. R. Boccaccini, I. Dlouhý, and M. Reece: 'Toughened and machinable glass matrix composites reinforced with graphene and graphene-oxide nano platelets', *Sci Technol Adv Mat*, 2013, **14**.
4. H. Porwal, P. Tatarko, R. Saggar, S. Grasso, M. Kumar Mani, I. Dlouhý, J. Dusza, and M. J. Reece: 'Tribological properties of silica–graphene nano-platelet composites', *Ceram Int*, 2014(0).
5. H. Porwal, P. Tatarko, S. Grasso, J. Khaliq, I. Dlouhý, and M. Reece: 'Graphene Reinforced Alumina Nano-Composites ', *Carbon*, 2013, **64**, 359-369.
6. H. Porwal, M. Kasiarova, P. Tatarko, S. Grasso, J. Dusza, and M. J. Reece: 'Scratch Behaviour of Graphene Alumina Nanocomposites', *Adv Appl Ceram*, 2015.
7. H. Porwal, S. Grasso, L. Cordero-Arias, C. Li, A. Boccaccini, and M. Reece: 'Processing and bioactivity of 45S5 Bioglass®-graphene nanoplatelets composites', *J Mater Sci: Mater Med*, 2014, 1-11.
8. H. Porwal, M. Estili, A. Grünewald, S. Grasso, R. Detsch, C. Hu, Y. Sakka, A. Boccaccini, and M. Reece: '45S5 Bioglass®-MWCNT Composite: Processing and Bioactivity', *J Mater Sci: Mater Med*, 2015, 26:199.
9. H. Porwal, R. Saggar, P. Tatarko, S. Grasso, I. Dlouhý and M. J. Reece: ‘Effect of lateral size of graphene nano- sheets on the mechanical properties of alumina nano-composites’, submitted 2015.

Publications from Collaborations

1. S. Grasso, R. K. Chinnam, H. Porwal, A. R. Boccaccini, and M. J. Reece: 'Low temperature spark plasma sintering of 45S5 Bioglass®', *J Non-Cryst Solids*, 2013, **362**, 25-29.
2. S. Grasso, H. Yoshida, H. Porwal, Y. Sakka, and M. Reece: 'Highly transparent α-alumina obtained by low cost high pressure SPS', *Ceram Int*, 2013, **39**, 3243-3248.
3. S. Grasso, T. Saunders, H. Porwal, O. Cedillos-Barraza, D. D. Jayaseelan, W. E. Lee, and M. J. Reece: 'Flash Spark Plasma Sintering (FSPS) of Pure ZrB2', *J Am Ceram Soc*, 2014, **97**(8), 2405-2408.
4. E. Bernardo, I. Ponsot, P. Colombo, S. Grasso, H. Porwal, and M. J. Reece: 'Polymer-derived SiC ceramics from polycarbosilane/boron mixtures densified by SPS', *Ceram Int*, 2014(0).
5. P. Tatarko, S. Grasso, H. Porwal, Z. Chlup, R. Saggar, I. Dlouhý, and M. J. Reece: 'Boron nitride nanotubes as a reinforcement for brittle matrices', *J Eur Ceram Soc*, 2014(0).
6. P. Tatarko, S. Grasso, Z. Chlup, H. Porwal, M. Kašiarová, I. Dlouhý, and M. J. Reece: 'Toughening effect of multi-walled boron nitride nanotubes and their influence on the sintering behaviour of 3Y-TZP zirconia ceramics', *J Eur Ceram Soc*, 2014, **34**(7), 1829-1843.
7. S. Grasso, P. Tatarko, S. Rizzo, H. Porwal, C. Hu, Y. Katoh, M. Salvo, M. J. Reece, and M. Ferraris: 'Joining of β-SiC by spark plasma sintering', *J Eur Ceram Soc*, 2014, **34**(7), 1681-1686.
8. S. Grasso, T. Saunders, H. Porwal, and M. Reece: 'Ultra-high temperature spark plasma sintering of α-SiC', *Ceram Int*, 2015, **41**(1, Part A), 225-230.
9. B. Yazdani, H. Porwal, Y. Xia, H. Yan, M. J. Reece, Y. Zhu: 'Role of synthesis method on microstructure and mechanical properties of graphene/carbon nanotube toughened Al_2O_3 nanocomposites', *Ceram Int*, 2015; 41(8).

References

[1] A. R. Bunsell JR. Fundamentals of Fibre Reinforced Composite Materials. London: CRC Press; 2005.

[2] Cho J, Boccaccini AR, Shaffer MSP. Ceramic matrix composites containing carbon nanotubes. J Mater Sci. 2009;44(8):1934-51.

[3] Hwang GL, Hwang KC. Carbon nanotube reinforced ceramics. J Mater Chem. 2001;11(6):1722-5.

[4] Zhan GD, Mukherjee AK. Carbon nanotube reinforced alumina-based ceramics with novel mechanical, electrical, and thermal properties. Int J Appl Ceram Tec. 2004;1(2):161-71.

[5] Cho J, Inam F, Reece MJ, Chlup Z, Dlouhy I, Shaffer MSP, et al. Carbon nanotubes: do they toughen brittle matrices? J Mater Sci. 2011;46(14):4770-9.

[6] Ning JW, Zhang JJ, Pan YB, Guo JK. Fabrication and mechanical properties of SiO2 matrix composites reinforced by carbon nanotube. Mat Sci Eng a-Struct. 2003;357(1-2):392-6.

[7] Sivakumar R, Guo SQ, Nishimura T, Kagawa Y. Thermal conductivity in multi-wall carbon nanotube/silica-based nanocomposites. Scripta Mater. 2007;56(4):265-8.

[8] Guo SQ, Sivakumar R, Kitazawa H, Kagawa Y. Electrical properties of silica-based nanocomposites with multiwall carbon nanotubes. J Am Ceram Soc. 2007;90(5):1667-70.

[9] Inam F, Yan HX, Jayaseelan DD, Peijs T, Reece MJ. Electrically conductive alumina-carbon nanocomposites prepared by Spark Plasma Sintering. J Eur Ceram Soc. 2010;30(2):153-7.

[10] Fan JP, Zhuang DM, Zhao DQ, Zhang G, Wu MS, Wei F, et al. Toughening and reinforcing alumina matrix composite with single-wall carbon nanotubes. Appl Phys Lett. 2006;89(12).

[11] Zhan GD, Kuntz JD, Garay JE, Mukherjee AK. Electrical properties of nanoceramics reinforced with ropes of single-walled carbon nanotubes. Appl Phys Lett. 2003;83(6):1228-30.

[12] Geim AK, Novoselov KS. The rise of graphene. Nat Mater. 2007;6(3):183-91.

[13] Lee C, Wei XD, Kysar JW, Hone J. Measurement of the elastic properties and intrinsic strength of monolayer graphene. Science. 2008;321(5887):385-8.

[14] Balandin AA, Ghosh S, Bao WZ, Calizo I, Teweldebrhan D, Miao F, et al. Superior thermal conductivity of single-layer graphene. Nano Lett. 2008;8(3):902-7.

[15] Fan YC, Wang LJ, Li JL, Li JQ, Sun SK, Chen F, et al. Preparation and electrical properties of graphene nanosheet/Al2O3 composites. Carbon. 2010;48(6):1743-9.

[16] He T, Li JL, Wang LJ, Zhu JJ, Jiang W. Preparation and Consolidation of Alumina/Graphene Composite Powders. Mater Trans. 2009;50(4):749-51.

[17] Lam CW, James JT, McCluskey R, Arepalli S, Hunter RL. A review of carbon nanotube toxicity and assessment of potential occupational and environmental health risks. Crit Rev Toxicol. 2006;36(3):189-217.

[18] Choi W, Lahiri I, Seelaboyina R, Kang YS. Synthesis of Graphene and Its Applications: A Review. Crit Rev Solid State. 2010;35(1):52-71.

[19] Stoller MD, Park SJ, Zhu YW, An JH, Ruoff RS. Graphene-Based Ultracapacitors. Nano Lett. 2008;8(10):3498-502.

[20] Blake P, Brimicombe PD, Nair RR, Booth TJ, Jiang D, Schedin F, et al. Graphene-based liquid crystal device. Nano Lett. 2008;8(6):1704-8.

[21] Wu JB, Agrawal M, Becerril HA, Bao ZN, Liu ZF, Chen YS, et al. Organic Light-Emitting Diodes on Solution-Processed Graphene Transparent Electrodes. Acs Nano. 2010;4(1):43-8.

[22] Wang X, Zhi LJ, Mullen K. Transparent, conductive graphene electrodes for dye-sensitized solar cells. Nano Lett. 2008;8(1):323-7.

[23] Stankovich S, Dikin DA, Dommett GHB, Kohlhaas KM, Zimney EJ, Stach EA, et al. Graphene-based composite materials. Nature. 2006;442(7100):282-6.

[24] Liang JJ, Wang Y, Huang Y, Ma YF, Liu ZF, Cai FM, et al. Electromagnetic interference shielding of graphene/epoxy composites. Carbon. 2009;47(3):922-5.

[25] Kalaitzidou K, Fukushima H, Drzal LT. Mechanical properties and morphological characterization of exfoliated graphite-polypropylene nanocomposites. Compos Part a-Appl S. 2007;38(7):1675-82.

[26] Yasmin A, Luo JJ, Daniel IM. Processing of expanded graphite reinforced polymer nanocomposites. Compos Sci Technol. 2006;66(9):1182-9.

[27] Walker LS, Marotto VR, Rafiee MA, Koratkar N, Corral EL. Toughening in Graphene Ceramic Composites. Acs Nano. 2011;5(4):3182-90.

[28] Du JH, Cheng HM. The Fabrication, Properties, and Uses of Graphene/Polymer Composites. Macromol Chem Phys. 2012;213(10-11):1060-77.

[29] Watcharotone S, Dikin DA, Stankovich S, Piner R, Jung I, Dommett GHB, et al. Graphene-silica composite thin films as transparent conductors. Nano Lett. 2007;7(7):1888-92.

[30] Tapaszto O, Tapaszto L, Marko M, Kern F, Gadow R, Balazsi C. Dispersion patterns of graphene and carbon nanotubes in ceramic matrix composites. Chem Phys Lett. 2011;511(4-6):340-3.

[31] Kun P, Tapaszto O, Weber F, Balazsi C. Determination of structural and mechanical properties of multilayer graphene added silicon nitride-based composites. Ceram Int. 2012;38(1):211-6.

[32] Zhou TN, Chen F, Liu K, Deng H, Zhang Q, Feng JW, et al. A simple and efficient method to prepare graphene by reduction of graphite oxide with sodium hydrosulfite. Nanotechnology. 2011;22(4).

[33] Zhu YW, Murali S, Cai WW, Li XS, Suk JW, Potts JR, et al. Graphene and Graphene Oxide: Synthesis, Properties, and Applications. Adv Mater. 2010;22(35):3906-24.

[34] Park S, Ruoff RS. Chemical methods for the production of graphenes. Nat Nanotechnol. 2009;4(4):217-24.

[35] Stankovich S, Dikin DA, Piner RD, Kohlhaas KA, Kleinhammes A, Jia Y, et al. Synthesis of graphene-based nanosheets via chemical reduction of exfoliated graphite oxide. Carbon. 2007;45(7):1558-65.

[36] Singh V, Joung D, Zhai L, Das S, Khondaker SI, Seal S. Graphene based materials: Past, present and future. Prog Mater Sci. 2011;56(8):1178-271.

[37] Ferrari AC. Raman spectroscopy of graphene and graphite: Disorder, electron-phonon coupling, doping and nonadiabatic effects. Solid State Commun. 2007;143(1-2):47-57.

[38] Wang K, Wang YF, Fan ZJ, Yan J, Wei T. Preparation of graphene nanosheet/alumina composites by spark plasma sintering. Mater Res Bull. 2011;46(2):315-8.

[39] Coleman JN. Liquid Exfoliation of Defect-Free Graphene. Accounts Chem Res. 2013;46(1):14-22.

[40] Khan U, Porwal H, O'Neill A, Nawaz K, May P, Coleman JN. Solvent-Exfoliated Graphene at Extremely High Concentration. Langmuir. 2011;27(15):9077-82.

[41] Khan U, O'Neill A, Porwal H, May P, Nawaz K, Coleman JN. Size selection of dispersed, exfoliated graphene flakes by controlled centrifugation. Carbon. 2012;50(2):470-5.

[42] Echeberria J, Rodriguez N, Vleugels J, Vanmeensel K, Reyes-Rojas A, Garcia-Reyes A, et al. Hard and tough carbon nanotube-reinforced zirconia-toughened alumina composites prepared by spark plasma sintering. Carbon. 2012;50(2):706-17.

[43] Estili M, Kawasaki A. Engineering Strong Intergraphene Shear Resistance in Multi-walled Carbon Nanotubes and Dramatic Tensile Improvements. Adv Mater. 2010;22(5):607-+.

[44] Inam F, Yan H, Reece MJ, Peijs T. Dimethylformamide: an effective dispersant for making ceramic-carbon nanotube composites. Nanotechnology. 2008;19(19).

[45] Yang Y, Wang Y, Tian W, Wang ZQ, Zhao Y, Wang L, et al. Reinforcing and toughening alumina/titania ceramic composites with nano-dopants from nanostructured composite powders. Mat Sci Eng a-Struct. 2009;508(1-2):161-6.

[46] Dusza J, Blugan G, Morgiel J, Kuebler J, Inam F, Peijs T, et al. Hot pressed and spark plasma sintered zirconia/carbon nanofiber composites. J Eur Ceram Soc. 2009;29(15):3177-84.

[47] Balazsi C, Shen Z, Konya Z, Kasztovszky Z, Weber F, Vertesy Z, et al. Processing of carbon nanotube reinforced silicon nitride composites by spark plasma sintering. Compos Sci Technol. 2005;65(5):727-33.

[48] Boccaccini AR, Thomas BJC, Brusatin G, Colombo P. Mechanical and electrical properties of hot-pressed borosilicate glass matrix composites containing multi-wall carbon nanotubes. J Mater Sci. 2007;42(6):2030-6.

[49] Tapaszto O, Marko M, Balazsi C. Distribution Patterns of Different Carbon Nanostructures in Silicon Nitride Composites. J Nanosci Nanotechno. 2012;12(11):8775-8.

[50] Michalkova M, Kasiarova M, Tatarko P, Dusza J, Sajgalik P. Effect of homogenization treatment on the fracture behaviour of silicon nitride/graphene nanoplatelets composites. J Eur Ceram Soc. 2014;34(14):3291-9.

[51] Lewis JA. Colloidal processing of ceramics. J Am Ceram Soc. 2000;83(10):2341-59.

[52] Rincon A, Chinelatto ASA, Moreno R. Tape casting of alumina/zirconia suspensions containing graphene oxide. J Eur Ceram Soc. 2014;34(7):1819-27.

[53] Rincon A, Moreno R, Chinelatto ASA, Gutierrez CF, Rayon E, Salvador MD, et al. Al2O3-3YTZP-Graphene multilayers produced by tape casting and spark plasma sintering. J Eur Ceram Soc. 2014;34(10):2427-34.

[54] Zheng C, Feng M, Zhen X, Huang J, Zhan HB. Materials investigation of multi-walled carbon nanotubes doped silica gel glass composites. J Non-Cryst Solids. 2008;354(12-13):1327-30.

[55] Zhan HB, Chen WZ, Wang MQ, Zhengchan, Zou CL. Optical limiting effects of multi-walled carbon nanotubes suspension and silica xerogel composite. Chem Phys Lett. 2003;382(3-4):313-7.

[56] Zeng Y, Zhou Y, Kong L, Zhou T, Shi G. A novel composite of SiO2-coated graphene oxide and molecularly imprinted polymers for electrochemical sensing dopamine. Biosensors and Bioelectronics. 2013;45:25-33.

[57] Cheng WY, Wang CC, Lu SY. Graphene aerogels as a highly efficient counter electrode material for dye-sensitized solar cells. Carbon. 2013;54:291-9.

[58] Yang JL, Wang JJ, Wang DN, Li XF, Geng DS, Liang GX, et al. 3D porous LiFePO4/graphene hybrid cathodes with enhanced performance for Li-ion batteries. J Power Sources. 2012;208:340-4.

[59] Cunci L, Rao CV, Velez C, Ishikawa Y, Cabrera CR. Graphene-Supported Pt, Ir, and Pt-Ir Nanoparticles as Electrocatalysts for the Oxidation of Ammonia. Electrocatalysis-Us. 2013;4(1):61-9.

[60] Ghosh T, Lee JH, Meng ZD, Ullah K, Park CY, Nikam V, et al. Graphene oxide based CdSe photocatalysts: Synthesis, characterization and comparative photocatalytic efficiency of rhodamine B and industrial dye. Mater Res Bull. 2013;48(3):1268-74.

[61] Cha SI, Kim KT, Arshad SN, Mo CB, Hong SH. Extraordinary strengthening effect of carbon nanotubes in metal-matrix nanocomposites processed by molecular-level mixing. Adv Mater. 2005;17(11):1377-+.

[62] Lee B, Koo MY, Jin SH, Kim KT, Hong SH. Simultaneous strengthening and toughening of reduced graphene oxide/alumina composites fabricated by molecular-level mixing process. Carbon. 2014;78:212-9.

[63] Colombo P, Mera G, Riedel R, Soraru GD. Polymer-Derived Ceramics: 40 Years of Research and Innovation in Advanced Ceramics. J Am Ceram Soc. 2010;93(7):1805-37.

[64] Sarkar S, Zou J, Liu J, Xu C, An L, Zhai L. Polymer-Derived Ceramic Composite Fibers with Aligned Pristine Multiwalled Carbon Nanotubes. 2010;2(4):1150-6.

[65] Duan RG, Mukherjee AK. Synthesis of SiCNO nanowires through heat-treatment of polymer-functionalized single-walled carbon nanotubes. Adv Mater. 2004;16(13):1106-+.

[66] An LN, Xu WX, Rajagopalan S, Wang CM, Wang H, Fan Y, et al. Carbon-nanotube-reinforeed polymer-derived ceramic composites. Adv Mater. 2004;16(22):2036-+.

[67] Lehman JH, Hurst KE, Singh G, Mansfield E, Perkins JD, Cromer CL. Core-shell composite of SiCN and multiwalled carbon nanotubes from toluene dispersion. J Mater Sci. 2010;45(15):4251-4.

[68] Bhandavat R, Singh G. Improved Electrochemical Capacity of Precursor-Derived Si(B)CN-Carbon Nanotube Composite as Li-Ion Battery Anode. Acs Appl Mater Inter. 2012;4(10):5092-7.

[69] Ji F, Li YL, Feng JM, Su D, Wen YY, Feng Y, et al. Electrochemical performance of graphene nanosheets and ceramic composites as anodes for lithium batteries. J Mater Chem. 2009;19(47):9063-7.

[70] Inam F, Yan H, Reece MJ, Peijs T. Structural and chemical stability of multiwall carbon nanotubes in sintered ceramic nanocomposite. Adv Appl Ceram. 2010;109(4):240-5.

[71] Peigney A, Flahaut E, Laurent C, Chastel F, Rousset A. Aligned carbon nanotubes in ceramic-matrix nanocomposites prepared by high-temperature extrusion. Chem Phys Lett. 2002;352(1-2):20-5.

[72] Boccaccini AR, Acevedo DR, Brusatin G, Colombo P. Borosilicate glass matrix composites containing multi-wall carbon nanotubes. J Eur Ceram Soc. 2005;25(9):1515-23.

[73] Flahaut E, Peigney A, Laurent C, Marliere C, Chastel F, Rousset A. Carbon nanotube-metal-oxide nanocomposites: Microstructure, electrical conductivity and mechanical properties. Acta Mater. 2000;48(14):3803-12.

[74] Sun J, Gao L. Development of a dispersion process for carbon nanotubes in ceramic matrix by heterocoagulation. Carbon. 2003;41(5):1063-8.

[75] Rul S, Lefevre-schlick F, Capria E, Laurent C, Peigney A. Percolation of single-walled carbon nanotubes in ceramic matrix nanocomposites. Acta Mater. 2004;52(4):1061-7.

[76] Grasso S, Sakka Y, Maizza G. Electric current activated/assisted sintering (ECAS): a review of patents 1906-2008. Sci Technol Adv Mat. 2009;10(5).

[77] Grasso S, Yoshida H, Porwal H, Sakka Y, Reece M. Highly transparent α-alumina obtained by low cost high pressure SPS. Ceram Int. 2013;39:3243-8.

[78] Milsom B, Viola G, Gao ZP, Inam F, Peijs T, Reece MJ. The effect of carbon nanotubes on the sintering behaviour of zirconia. J Eur Ceram Soc. 2012;32(16):4149-56.

[79] Inam F, Yan HX, Peijs T, Reece MJ. The sintering and grain growth behaviour of ceramic-carbon nanotube nanocomposites. Compos Sci Technol. 2010;70(6):947-52.

[80] Centeno A, Rocha VG, Alonso B, Fernandez A, Gutierrez-Gonzalez CF, Torrecillas R, et al. Graphene for tough and electroconductive alumina ceramics. J Eur Ceram Soc. 2013;33(15-16):3201-10.

[81] Tapaszto O, Kun P, Weber F, Gergely G, Balazsi K, Pfeifer J, et al. Silicon nitride based nanocomposites produced by two different sintering methods. Ceram Int. 2011;37(8):3457-61.

[82] Kvetkova L, Duszova A, Hvizdos P, Dusza J, Kun P, Balazsi C. Fracture toughness and toughening mechanisms in graphene platelet reinforced Si3N4 composites. Scripta Mater. 2012;66(10):793-6.

[83] Liu J, Yan HX, Reece MJ, Jiang K. Toughening of zirconia/alumina composites by the addition of graphene platelets. J Eur Ceram Soc. 2012;32(16):4185-93.

[84] Liu J, Yan H, Jiang K. Mechanical properties of graphene platelet-reinforced alumina ceramic composites. Ceram Int. 2013.

[85] Nieto A, Lahiri D, Agarwal A. Graphene NanoPlatelets reinforced tantalum carbide consolidated by spark plasma sintering. Mat Sci Eng a-Struct. 2013;582:338-46.

[86] Kvetková L, Duszová A, Kašiarová M, Dorčáková F, Dusza J, Balázsi C. Influence of processing on fracture toughness of Si3N4+graphene platelet composites. J Eur Ceram Soc. 2013;33(12):2299-304.

[87] Shuai CJ, Gao CD, Feng P, Peng SP. Graphene-reinforced mechanical properties of calcium silicate scaffolds by laser sintering. Rsc Adv. 2014;4(25):12782-8.

[88] Chen Y-F, Bi J-Q, Yin C-L, You G-L. Microstructure and fracture toughness of graphene nanosheets/alumina composites. Ceram Int. 2014;40(9, Part A):13883-9.

[89] Kim HJ, Lee SM, Oh YS, Yang YH, Lim YS, Yoon DH, et al. Unoxidized Graphene/Alumina Nanocomposite: Fracture- and Wear-Resistance Effects of Graphene on Alumina Matrix. Sci Rep-Uk. 2014;4.

[90] Singh VK, Cura ME, Liu X, Johansson L-S, Ge Y, Hannula S-P. Tuning the Mechanical and Adsorption Properties of Silica with Graphene Oxide. ChemPlusChem. 2014;79(10):1512-22.

[91] Mehrali M, Moghaddam E, Shirazi SFS, Baradaran S, Mehrali M, Latibari ST, et al. Synthesis, Mechanical Properties, and in Vitro Biocompatibility with Osteoblasts of Calcium Silicate–Reduced Graphene Oxide Composites. Acs Appl Mater Inter. 2014;6(6):3947-62.

[92] Liu Y, Huang J, Li H. Synthesis of hydroxyapatite-reduced graphite oxide nanocomposites for biomedical applications: oriented nucleation and epitaxial growth of hydroxyapatite. J Mater Chem B. 2013;1(13):1826-34.

[93] Liu Y, Huang J, Li H. Nanostructural Characteristics of Vacuum Cold-Sprayed Hydroxyapatite/Graphene-Nanosheet Coatings for Biomedical Applications. J Therm Spray Techn. 2014;23(7):1149-56.

[94] Zhu JT, Wong HM, Yeung KWK, Tjong SC. Spark Plasma Sintered Hydroxyapatite/Graphite Nanosheet and Hydroxyapatite/Multiwalled Carbon Nanotube Composites: Mechanical and in Vitro Cellular Properties. Adv Eng Mater. 2011;13(4):336-41.

[95] Lawn B. Indentation Fracture in Fracture of Brittile Solids-Second Edition. Cambridge: Press Syndicate of the University of Cambridge 1993, p. 249-304.

[96] Wang XT, Padture NP, Tanaka H. Contact-damage-resistant ceramic/single-wall carbon nanotubes and ceramic/graphite composites. Nat Mater. 2004;3(8):539-44.

[97] Quinn GD, Bradt RC. On the Vickers indentation fracture toughness test. J Am Ceram Soc. 2007;90(3):673-80.

[98] Sheldon BW, Curtin WA. Nanoceramic composites: Tough to test. Nat Mater. 2004;3(8):505-6.

[99] Anstis GR, Chantikul P, Lawn BR, Marshall DB. A Critical-Evaluation of Indentation Techniques for Measuring Fracture-Toughness .1. Direct Crack Measurements. J Am Ceram Soc. 1981;64(9):533-8.

[100] Dusza J, Morgiel J, Duszova A, Kvetkova L, Nosko M, Kun P, et al. Microstructure and fracture toughness of Si3N4 + graphene platelet composites. J Eur Ceram Soc. 2012;32(12):3389-97.

[101] Inam F, Peijs T, Reece MJ. The production of advanced fine-grained alumina by carbon nanotube addition. J Eur Ceram Soc. 2011;31(15):2853-9.

[102] Ramirez C, Osendi MI. Toughening in ceramics containing graphene fillers. Ceram Int. 2014;40(7, Part B):11187-92.

[103] Hvizdos P, Dusza J, Balázsi C. Tribological properties of Si3N4–graphene nanocomposites. J Eur Ceram Soc. 2013;33:2359-64.

[104] Balko J, Hvizdos P, Dusza J, Balazsi C, Gamcova J. Wear damage of Si3N4-graphene nanocomposites at room and elevated temperatures. J Eur Ceram Soc. 2014;34(14):3309-17.

[105] Belmonte M, Ramírez C, González-Julián J, Schneider J, Miranzo P, Osendi MI. The beneficial effect of graphene nanofillers on the tribological performance of ceramics. Carbon. 2013;61(0):431-5.

[106] Li HQ, Xie YT, Li K, Huang LP, Huang SS, Zhao BZ, et al. Microstructure and wear behavior of graphene nanosheets-reinforced zirconia coating. Ceram Int. 2014;40(8):12821-9.

[107] Fan YC, Jiang W, Kawasaki A. Highly Conductive Few-Layer Graphene/Al2O3 Nanocomposites with Tunable Charge Carrier Type. Adv Funct Mater. 2012;22(18):3882-9.

[108] Ramirez C, Garzon L, Miranzo P, Osendi MI, Ocal C. Electrical conductivity maps in graphene nanoplatelet/silicon nitride composites using conducting scanning force microscopy. Carbon. 2011;49(12):3873-80.

[109] Ramirez C, Figueiredo FM, Miranzo P, Poza P, Osendi MI. Graphene nanoplatelet/silicon nitride composites with high electrical conductivity. Carbon. 2012;50(10):3607-15.

[110] Miranzo P, Ramirez C, Roman-Manso B, Garzon L, Gutierrez HR, Terrones M, et al. In situ processing of electrically conducting graphene/SiC nanocomposites. J Eur Ceram Soc. 2013;33(10):1665-74.

[111] Ramirez C, Vega-Diaz SM, Morelos-Gomez A, Figueiredo FM, Terrones M, Osendi MI, et al. Synthesis of conducting graphene/Si3N4 composites by spark plasma sintering. Carbon. 2013;57:425-32.

[112] Shin JH, Hong SH. Fabrication and properties of reduced graphene oxide reinforced yttria-stabilized zirconia composite ceramics. J Eur Ceram Soc. 2014;34(5):1297-302.

[113] Miranzo P, Garcia E, Ramirez C, Gonzalez-Julian J, Belmonte M, Osendi MI. Anisotropic thermal conductivity of silicon nitride ceramics containing carbon nanostructures. J Eur Ceram Soc. 2012;32(8):1847-54.

[114] Rutkowski P, Stobierski L, Górny G. Thermal stability and conductivity of hot-pressed Si3N4–graphene composites. J Therm Anal Calorim. 2014;116(1):321-8.

[115] Inam F, Bhat BR, Vo T, Daoush WM. Structural health monitoring capabilities in ceramic-carbon nanocomposites. Ceram Int. 2014;40(2):3793-8.

[116] Inam F, Vo T, Bhat BR. Structural stability studies of graphene in sintered ceramic nanocomposites. Ceram Int. 2014;40(10, Part B):16227-33.

[117] Guo ZX, Zhang D, Gong XG. Thermal conductivity of graphene nanoribbons. Appl Phys Lett. 2009;95(16).

[118] Lin KL, Zhai WY, Ni SY, Chang J, Zeng Y, Qian WJ. Study of the mechanical property and in vitro biocompatibility of CaSiO3 ceramics. Ceram Int. 2005;31(2):323-6.

[119] Zhao SJ, Wang LJ, Jiang W, Zhang JF, Chen LD. Mechanical Properties of CaSiO3/Ti3SiC2 Composites and Hydroxyapatite Forming Ability in Simulated Body Fluid. Mater Trans. 2008;49(10):2310-4.

[120] Wu CT, Ramaswamy Y, Soeparto A, Zreiqat H. Incorporation of titanium into calcium silicate improved their chemical stability and biological properties. J Biomed Mater Res A. 2008;86A(2):402-10.

[121] Shirazi FS, Mehrali M, Ataollahi Oshkour A, Cornelis Metselaar HS, Kadri NA, Abu Osman NA. Characterization and Mechanical Properties of Calcium Silicate/Citric Acid–Based Polymer Composite Materials. Int J Appl Ceram Tec. 2013:n/a-n/a.

[122] Conroy JV, Navin K.; Smith, Ronan J.; Rezvani, Ehsan; Duesberg, Georg S.; Coleman, Jonathan N.; Volkov, Yuri. Biocompatibility of Pristine Graphene Monolayers, Nanosheets and Thin Films. arXiv:14062497 [q-bioCB]. 2014.

[123] Fan HL, Wang LL, Zhao KK, Li N, Shi ZJ, Ge ZG, et al. Fabrication, Mechanical Properties, and Biocompatibility of Graphene-Reinforced Chitosan Composites. Biomacromolecules. 2010;11(9):2345-51.

[124] Kalbacova M, Broz A, Kong J, Kalbac M. Graphene substrates promote adherence of human osteoblasts and mesenchymal stromal cells. Carbon. 2010;48(15):4323-9.

[125] Berrueco C, Alvarez P, Venditti S, Morgan TJ, Herod AA, Millan M, et al. Sample Contamination with NMP-oxidation Products and Byproduct-free NMP Removal from Sample Solutions. Energ Fuel. 2009;23:3008-15.

[126] Hench LL. Bioceramics. J Am Ceram Soc. 1998;81(7):1705-28.

[127] Grasso S, Chinnam RK, Porwal H, Boccaccini AR, Reece MJ. Low temperature spark plasma sintering of 45S5 Bioglass®. J Non-Cryst Solids. 2013;362:25-9.

[128] Yi M, Shen ZG, Zhang XJ, Ma SL. Achieving concentrated graphene dispersions in water/acetone mixtures by the strategy of tailoring Hansen solubility parameters. J Phys D Appl Phys. 2013;46(2).

[129] Khan U, May P, Porwal H, Nawaz K, Coleman JN. Improved Adhesive Strength and Toughness of Polyvinyl Acetate Glue on Addition of Small Quantities of Graphene. Acs Appl Mater Inter. 2013;5(4):1423-8.

[130] Dresselhaus MS, Jorio A, Hofmann M, Dresselhaus G, Saito R. Perspectives on Carbon Nanotubes and Graphene Raman Spectroscopy. Nano Lett. 2010;10(3):751-8.

[131] Khan U, O'Neill A, Lotya M, De S, Coleman JN. High-Concentration Solvent Exfoliation of Graphene. Small. 2010;6(7):864-71.

[132] Boccaccini AR, Rawlings RD, Dlouhy I. Reliability of the chevron-notch technique for fracture toughness determination in glass. Mat Sci Eng a-Struct. 2003;347(1-2):102-8.

[133] Dlouhy I, Chlup Z, Chawla KK, Kulkarni R, Koopman M, Boccaccini AR. Effect of static pre-loading on fracture toughness of Nicalon (R) fibre glass matrix composite. Mat Sci Eng a-Struct. 2004;367(1-2):17-23.

[134] Venkatesh R. Mechanical properties of alumina fiber glass matrix composites with and without a tin dioxide interface. Mat Sci Eng a-Struct. 1999;268(1-2):47-54.

[135] Chlup Z, Dlouhy I. Size Effect in Fracture Toughness Determination of Brittle Materials. Advances in Science and Technology. 2006;45:101-6.

[136] Bluhm JI. Slice synthesis of a three dimensional "work of fracture" specimen. Engineering Fracture Mechanics. 1975;7(3):593-604.

[137] Wu S-X. Fracture toughness determination of bearing steel using chevron-notch three point bend specimen. Engineering Fracture Mechanics. 1984;19(2):221-32.

[138] Dlouhy I, Holzmann M, Man J, Valka L. The Use of Chevron-Notched Specimens for Fracture-Toughness Determination of Bearing Steels. Kovove Mater. 1994;32(1):3-13.

[139] Huh SH. Thermal Reduction of Graphene Oxide. In: Mikhailov S, ed. Physics and Applications of Graphene-Experiments: InTech 2011, p. 73-90.

[140] Zhan D, Ni ZH, Chen W, Sun L, Luo ZQ, Lai LF, et al. Electronic structure of graphite oxide and thermally reduced graphite oxide. Carbon. 2011;49(4):1362-6.

[141] Ferrari AC, Robertson J. Interpretation of Raman spectra of disordered and amorphous carbon. Phys Rev B. 2000;61(20):14095-107.

[142] Wu YP, Wang B, Ma YF, Huang Y, Li N, Zhang F, et al. Efficient and large-scale synthesis of few-layered graphene using an arc-discharge method and conductivity studies of the resulting films. Nano Res. 2010;3(9):661-9.

[143] Thomas BJC, Shaffer MSP, Boccaccini AR. Sol-gel route to carbon nanotube borosilicate glass composites. Compos Part a-Appl S. 2009;40(6-7):837-45.

[144] Treacy MMJ, Ebbesen TW, Gibson JM. Exceptionally high Young's modulus observed for individual carbon nanotubes. Nature. 1996;381(6584):678-80.

[145] Ruoff RS, Lorents DC. Mechanical and Thermal-Properties of Carbon Nanotubes. Carbon. 1995;33(7):925-30.

[146] Thess A, Lee R, Nikolaev P, Dai HJ, Petit P, Robert J, et al. Crystalline ropes of metallic carbon nanotubes. Science. 1996;273(5274):483-7.

[147] Mounet N, Marzari N. First-principles determination of the structural, vibrational and thermodynamic properties of diamond, graphite, and derivatives. Phys Rev B. 2005;71(20).

[148] Yoon D, Son YW, Cheong H. Negative Thermal Expansion Coefficient of Graphene Measured by Raman Spectroscopy. Nano Lett. 2011;11(8):3227-31.

[149] Boccaccini AR. Machinability and brittleness of glass-ceramics. J Mater Process Tech. 1997;65(1-3):302-4.

[150] Kim HJ, Kim DE. MD simulation of the frictional behavior of CNTs with respect to orientation. Tribol Int. 2012;50:51-6.

[151] Liu YH, Wang XK, Pan GS, Luo JB. A comparative study between graphene oxide and diamond nanoparticles as water-based lubricating additives. Sci China Technol Sc. 2013;56(1):152-7.

[152] Yu ZT, Fang X, Fan LW, Wang X, Xiao YQ, Zeng Y, et al. Increased thermal conductivity of liquid paraffin-based suspensions in the presence of carbon nano-additives of various sizes and shapes. Carbon. 2013;53:277-85.

[153] Suvorov YV, Alekseeva SI, Fronya MA, Viktorova IV. Investigations of physical and mechanical properties of polymeric nanocomposites (review). Inorg Mater+. 2013;49(15):1357-68.

[154] Eliezer Z, Ramage CH, Rylander HG, Flowers RH, Amateau MF. High-Speed Tribological Properties of Graphite Fiber-Cu-Sn Matrix Composites. Wear. 1978;49(1):119-33.

[155] Minford E, Prewo K. Friction and Wear of Graphite-Fiber-Reinforced Glass Matrix Composites. Wear. 1985;102(3):253-64.

[156] D. C. Phillips RAJS, D. H. Bowen. The mechanical properties of carbon fibre reinforced Pyrex glass. J Mater Sci. 1972;7(12):1454.

[157] Sambell RAJ, Phillips DC, Bowen DH. Carbon Fiber Composites with Ceramic and Glass Matrices .1. Discontinuous Fibers. J Mater Sci. 1972;7(6):663-&.

[158] C.A. Berg SB, J. Tirosh. Wear and friction of two different types of graphite fibre reinforced composite materials. Fibre Science and Technology. 1973;6(3):159.

[159] Liu MC, Chen CL, Hu J, Wu XL, Wang XK. Synthesis of Magnetite/Graphene Oxide Composite and Application for Cobalt(II) Removal. J Phys Chem C. 2011;115(51):25234-40.

[160] Balandin AA. Thermal properties of graphene and nanostructured carbon materials. Nat Mater. 2011;10(8):569-81.

[161] Boccaccini AR. The Relationship between Wear Behaviour and Brittleness Index in Engineering Ceramics and Dispersion-Reinforced Ceramic Composites. Interceram. 1999;48:176-87.

[162] Tsoukleri G, Parthenios J, Papagelis K, Jalil R, Ferrari AC, Geim AK, et al. Subjecting a Graphene Monolayer to Tension and Compression. Small. 2009;5(21):2397-402.

[163] Evans AG. Perspective on the Development of High-Toughness Ceramics. J Am Ceram Soc. 1990;73(2):187-206.

[164] Liu J, Yan H, Jiang K. Mechanical properties of graphene platelet-reinforced alumina ceramic composites. Ceram Int. 2013(0).

[165] Seiner H, Sedlak P, Koller M, Landa M, Ramirez C, Osendi MI, et al. Anisotropic elastic moduli and internal friction of graphene nanoplatelets/silicon nitride composites. Compos Sci Technol. 2013;75:93-7.

[166] Lim DS, You DH, Choi HJ, Lim SH, Jang H. Effect of CNT distribution on tribological behavior of alumina–CNT composites. Wear. 2005;259(1–6):539-44.

[167] Ahmad I, Kennedy A, Zhu YQ. Wear resistant properties of multi-walled carbon nanotubes reinforced Al2O3 nanocomposites. Wear. 2010;269(1-2):71-8.

[168] Hvizdos P, Puchy V, Duszova A, Dusza J, Balazsi C. Tribological and electrical properties of ceramic matrix composites with carbon nanotubes. Ceram Int. 2012;38(7):5669-76.

[169] Manuel Belmonte CR, Jesus Gonzalez-Julian, Johannes Schneider, Pilar Miranzo, Marıa Isabel Osendi, A. R. Bunsell, Jacques Renard. The beneficial effect of graphene nanofillers on the tribological performance of ceramics. Carbon. 2013;61:431-5.

[170] Le Houerou V, Sangleboeuf JC, Deriano S, Rouxel T, Duisit G. Surface damage of soda-lime-silica glasses: indentation scratch behavior. J Non-Cryst Solids. 2003;316(1):54-63.

[171] Tatarko P, Grasso S, Porwal H, Chlup Z, Saggar R, Dlouhý I, et al. Boron nitride nanotubes as a reinforcement for brittle matrices. J Eur Ceram Soc. 2014(0).

[172] Sarkar S, Das PK. Dry sliding wear characteristics of carbon nanotube/alumina nanocomposites under a sharp pyramidal indenter. Ceram Int. 2014;40(9):13971-8.

[173] Hvizdoš P, Dusza J, Balázsi C. Tribological properties of Si3N4–graphene nanocomposites. J Eur Ceram Soc. 2013;33(12):2359-64.

[174] Hench LL, Splinter RJ, Allen WC, Greenlee TK. Bonding mechanisms at the interface of ceramic prosthetic materials. J Biomed Mater Res A. 1971;5(6):117.

[175] Hench LL. The story of Bioglass (R). J Mater Sci-Mater M. 2006;17(11):967-78.

[176] Hench LL. Biomaterials: a forecast for the future. Biomaterials. 1998;19(16):1419-23.

[177] Ducheyne P, Qiu Q. Bioactive ceramics: the effect of surface reactivity on bone formation and bone cell function. Biomaterials. 1999;20(23-24):2287-303.

[178] Lopez-Esteban S, Saiz E, Fujino S, Oku T, Suganuma K, Tomsia AP. Bioactive glass coatings for orthopedic metallic implants. J Eur Ceram Soc. 2003;23(15):2921-30.

[179] Bahniuk MS, Pirayesh H, Singh HD, Nychka JA, Unsworth LD. Bioactive Glass 45S5 Powders: Effect of Synthesis Route and Resultant Surface Chemistry and Crystallinity on Protein Adsorption from Human Plasma. Biointerphases. 2012;7(1-4).

[180] Xynos ID, Edgar AJ, Buttery LDK, Hench LL, Polak JM. Ionic products of bioactive glass dissolution increase proliferation of human osteoblasts and induce insulin-like growth factor II mRNA expression and protein synthesis. Biochem Bioph Res Co. 2000;276(2):461-5.

[181] Cao WP, Hench LL. Bioactive materials. Ceram Int. 1996;22(6):493-507.

[182] Drnovsek N, Novak S, Dragin U, Ceh M, Gorensek M, Gradisar M. Bioactive glass enhances bone ingrowth into the porous titanium coating on orthopaedic implants. Int Orthop. 2012;36(8):1739-45.

[183] Gorustovich AA, Roether JA, Boccaccini AR. Effect of Bioactive Glasses on Angiogenesis: A Review of In Vitro and In Vivo Evidences. Tissue Eng Part B-Re. 2010;16(2):199-207.

[184] Zhang D, Lepparanta O, Munukka E, Ylanen H, Viljanen MK, Eerola E, et al. Antibacterial effects and dissolution behavior of six bioactive glasses. J Biomed Mater Res A. 2010;93A(2):475-83.

[185] Aron B. Anderson AWD, Stephen J. Chudzik, Lise W. Duran, Patrick E. Guire, Robert W. Hergenrother, Muhammad A. Lodhi, Amy E. Novak, Ronald F. Ofstead, Klaus Wormuth. Technologies for the surface modification of biomaterials In: Michael J. Yaszemski DJT, Kai-Uwe Lewandrowski, Vasif Hasirci, David E. Altobelli, Donald L. Wise, ed. Biomaterials in Orthopedics 2004, p. 123.

[186] Sanchez VC, Jachak A, Hurt RH, Kane AB. Biological Interactions of Graphene-Family Nanomaterials: An Interdisciplinary Review. Chem Res Toxicol. 2012;25(1):15-34.

[187] Supronowicz PR, Ajayan PM, Ullmann KR, Arulanandam BP, Metzger DW, Bizios R. Novel current-conducting composite substrates for exposing osteoblasts to alternating current stimulation. J Biomed Mater Res. 2002;59(3):499-506.

[188] Hrapovic S, Liu YL, Male KB, Luong JHT. Electrochemical biosensing platforms using platinum nanoparticles and carbon nanotubes. Anal Chem. 2004;76(4):1083-8.

[189] Khang D, Park GE, Webster TJ. Enhanced chondrocyte densities on carbon nanotube composites: The combined role of nanosurface roughness and electrical stimulation. J Biomed Mater Res A. 2008;86A(1):253-60.

[190] Yang WR, Thordarson P, Gooding JJ, Ringer SP, Braet F. Carbon nanotubes for biological and biomedical applications. Nanotechnology. 2007;18(41).

[191] Li XM, Gao H, Uo M, Sato Y, Akasaka T, Feng QL, et al. Effect of carbon nanotubes on cellular functions in vitro. J Biomed Mater Res A. 2009;91A(1):132-9.

[192] Zanello LP, Zhao B, Hu H, Haddon RC. Bone cell proliferation on carbon nanotubes. Nano Lett. 2006;6(3):562-7.

[193] Meng D RS, Mordan N, Salih V, Kneser U, Boccaccini AR In vitro evaluation of 45S5 Bioglass®-derived glass-ceramic scaffolds coated with carbon nanotubes. J Biomed Mater Res A. 2011;99A:435-44.

[194] Afrin R, Khaliq J, Islam M, Gul IH, Bhatti AS, Manzoord U. Synthesis of multiwalled carbon nanotube-based infrared radiation detector. Sensor Actuat a-Phys. 2012;187:73-8.

[195] Paola Fabbri LV, Jasmin Hum, Rainer Detsch, Aldo R. Boccaccini. 45S5 Bioglass®-derived scaffolds coated with organic–inorganic hybrids containing graphene. Materials Science and Engineering C. 2013;33:3592-600.

[196] Tadashi Kokubo HT. How useful is SBF in predicting in vivo bone bioactivity? Biomaterials. 2006;27(15):2907-15.

[197] Peitl O, LaTorre GP, Hench LL. Effect of crystallization on apatite-layer formation of bioactive glass 45S5. J Biomed Mater Res. 1996;30(4):509-14.

[198] Chen QZ, Thompson ID, Boccaccini AR. 45S5 Bioglass®-derived glass–ceramic scaffolds for bone tissue engineering. Biomaterials. 2006;27(11):2414-25.